Pontifícia Universidade Católica
do Rio de Janeiro

Felippe Moraes Silva Costa

Cycle Counting Methods for Load-Time-Histories Typical for Power Plant Applications

Dissertação de Mestrado

Thesis presented to the Programa de Pós-Graduação em Engenharia Mecânica of the Departamento de Engenharia Mecânica do Centro Técnico Científico da PUC-Rio, as partial fulfillment of the requirements for the degree of Mestre.

Advisor: Prof. José Luiz de França Freire

Co-Advisor: Dr. Jürgen Rudolph

Rio de Janeiro
April 2015

Felippe Moraes Silva Costa

Cycle Counting Methods for Load-Time-Histories Typical for Power Plant Applications

Thesis presented to the Programa de Pós-Graduação em Engenharia Mecânica of the Departamento de Engenharia Mecânica do Centro Técnico Científico da PUC-Rio, as partial fulfillment of the requirements for the degree of Mestre.

Prof. José Luiz de França Freire
Advisor
Departamento de Engenharia Mecânica – PUC-Rio

Dr. Jürgen Rudolph
Co-Advisor
AREVA

Prof. Marco Antonio Meggiolaro
Departamento de Engenharia Mecânica – PUC-Rio

Prof. Arthur Martins Barbosa Braga
Departamento de Engenharia Mecânica – PUC-Rio

Dr. José Eduardo de Almeida Maneschy
ELETROBRAS - ELETRONUCLEAR

Prof. José Eugenio Leal
Coordenador Setorial do Centro Técnico Científico – PUC-Rio

Rio de Janeiro, April 8th, 2015

Felippe Moraes Silva Costa

Graduated in mechanical engineering in 2012 at the Pontifical Catholic University of Rio de Janeiro. Worked since then in the area of assessment of structural integrity and software development for structural integrity analysis.

Ficha Catalográfica

Costa, Felippe Moraes Silva

Cycle counting methods for load-time-histories typical for power plant applications / Felippe Moraes Silva Costa ; advisor: José Luiz de França Freire ; co-advisor: Jürgen Rudolph. – 2015.
126 f. : Il. (color) ; 30 cm

Dissertação (mestrado)–Pontifícia Universidade Católica do Rio de Janeiro, Departamento de Engenharia Mecânica, 2015.
Inclui bibliografia

1. Engenharia mecânica – Teses. 2. Componentes de usina térmica. 3. Projeto contra a fadiga. 4. Fadiga de baixo ciclo. 5. História de carga no tempo. 6. Método de contagem de ciclos. 7. Algoritmos multiaxiais. 8. Carregamento não-proporcional. 9. Carregamento multiaxial. I. Freire, José Luiz de França Freire. II. Rudolph, Jürgen. III. Pontifícia Universidade Católica do Rio de Janeiro. Departamento de Engenharia Mecânica. III. Título.

CDD:621

Acknowledgments

I would like to thank my advisor Dr. José Luiz de França Freire and my co-advisor Dr. Jürgen Rudolph for their confidence on me by given me a great opportunity which I will always be in debt.

In addition, I would like to thank my advisor Dr. José Luiz de França Freire for his support, patience and encouragement during this journey and for the entire professional and life knowledge that he passed to me.

I want to thank all the colleagues at AREVA's PEEA-G department in especial my co-advisor Dr. Jürgen Rudolph for his help and guidance during my stay at the company.

Furthermore, I like to thank my laboratory colleagues who have made lighter the process of getting my master degree.

I also like to thank CAPES, CNPq, FAPERJ and AREVA for the financial support.

Finally, I like to give a special thanks to my friends, in particular to Igor, Leandro and Lucas for their loyal friendship and to my family, in particular my mother for her devoted love and support.

Abstract

Costa, Felippe Moraes Silva; Freire, José Luiz de França (Advisor); Rudolph, Jürgen (Co-Advisor). **Cycle Counting Methods for Load-Time-Histories Typical for Power Plant Applications.** Rio de Janeiro, 2015. 126p. MSc. Dissertation - Departamento de Engenharia Mecânica, Pontifícia Universidade Católica do Rio de Janeiro.

Structural components of power plants are subjected to thermal transients during their operational life. These thermal transients generate unequal temperature distributions across the components' wall thickness, causing severe thermal stresses. The repetition of the thermal transients and, consequently, repetition of stress and strain variations are responsible for fatigue damage of the structural components. In such cases, fatigue damage is assessed by calculating the cumulative usage factor or CUF. CUF calculations are based on the stresses and strains histories, on experimental fatigue curves and fatigue damage models, and on algorithms used to determine the number of cycles a given stress or strain range occurs during the life period considered. This thesis presents and discusses fatigue damage models and their association with existing cycle counting models that are applicable to power plant components. A selection of combinations of damage and cycle-counting models was used in two case study examples.

Keywords

Power plant components; design against fatigue; Low Cycle Fatigue (LCF); load time histories; analytical solution; cycle counting methods; multiaxial algorithms; proportional loading; non-proportional loading; multiaxial loading.

Resumo

Costa, Felippe Moraes Silva; Freire, José Luiz de França (Orientador); Rudolph, Jürgen (Coorientador). **Métodos de Contagem de Ciclos Usados em Histórias de Carregamentos Típicas de Usinas Nucleares.** Rio de Janeiro, 2015. 126p. Dissertação de Mestrado - Departamento de Engenharia Mecânica, Pontifícia Universidade Católica do Rio de Janeiro.

Componentes estruturais de usinas térmicas para geração de energia sofrem transientes térmicos durante a operação da planta devido a partidas e paradas, variações de potência requerida e ocorrências causadas por anomalias. Estes transientes térmicos geram distribuições de temperaturas não uniformes ao longo da espessura dos componentes e, consequentemente, geram tensões térmicas. As variações destas tensões ao longo do tempo podem causar fadiga nos pontos mais solicitados destes componentes. A análise de fadiga para um ponto crítico do componente fornece o dano acumulado por meio do fator acumulado de dano ou CUF. O cálculo do CUF é feito baseado no conhecimento das histórias de tensões e deformações que ocorrem nos pontos críticos, no uso de modelos de geração de dano ciclo a ciclo e no uso de algoritmos para contagem de ciclos. Esta dissertação apresenta e discute modelos de dano a fadiga e suas associações aos modelos de contagem de ciclos existentes que são possíveis de serem aplicadas a componentes de usinas térmicas. Uma seleção de combinações entre modelos de dano e métodos de contagem foram utilizadas em dois exemplos nomeados estudos de caso.

Palavras chaves

Componentes de usina térmica; projeto contra a fadiga; fadiga de baixo ciclo; história de carga no tempo; método de contagem de ciclos; algoritmos multiaxiais; carregamento proporcional; carregamento não-proporcional; carregamento multiaxial.

Contents

List of Figures

List of Tables

1

Introduction

The methods used to design and assess considering fatigue as the principal damage mechanism are well treated in references [1-4] and can be separated into four categories: stress-life methods, strain-life methods, energy-life methods and fracture mechanics methods. The first three methods focus on studying the initiation of a micro crack, while the last one focuses on the growth of a macro crack.

Stress-life methods are called SN methods and strain-life methods are commonly referred to as εN methods. Generally speaking, SN (stress-life or high cycle fatigue) methods are related to varying stresses that are elastic and, consequently, lower than the material yield strength. They are also connected to lives that are higher than a few thousand cycles. εN (strain-life or low cycle fatigue) methods are related to large varying stress that induce critical points of the components to large elastic and plastic varying strains. Consequently, these stresses are higher than the material yield strength and are connected to lives that are shorter than a few thousand cycles. Pressure vessels and power plant design codes (such as ASME section III and ASME section VIII), in addition to fitness-in-service codes (such as API 579-1/ASME FFS-1), deal with fatigue assessment using εN methods. In such cases, εN methods are applied to critical points of components that are expected to operate safely for a few hundred cycles or for millions of cycles.

In this master's thesis, several aspects of a fatigue analysis using εN methods applicable to power plant components subjected to mechanical and thermal loads are developed and discussed.

The first aspect to be studied is the stress analysis of a simple case, where a thick walled pipe is subjected to thermal and mechanical loads that are typical for power plant facilities.

The principal goal of this study is to develop a procedure that can be implemented in a software program in such a way that the time required to evaluate the full stress solutions can be optimized, since the usual finite element procedures implemented so far are still too time consuming.

This analytical procedure (proposed in Chapter 2) used for a thick walled pipe is not only faster to evaluate but also makes known the stress distribution across the thickness of the pipe. This distribution is needed to linearize the stresses so that the ASME and API Codes addressing elastic stress fatigue assessment procedures for pressure vessels and power plant components may be used. The procedure for stress linearization is presented in Chapter 2.

The second aspect is the presentation of fatigue damage models and cycle counting method algorithms applicable to proportional and non-proportional histories. These subjects are presented and explained in Chapters 3 and 4, respectively. The principal characteristics and relevant differences are developed in these chapters, as well as the adaptations required for implementing calculation procedures when particular combinations of cycle counting methods and damage models are used.

The third aspect is presented in Chapter 5. This chapter discusses the stress-strain relationship when a non-proportional history is analyzed in such a way that non-proportional hardening and strain plasticity sequence effects can be calculated and considered in the fatigue assessment procedure.

Lastly, the methods discussed in Chapters 2 to 5 are applied to two examples to explain and show their life prediction differences.

2

Stress Analysis

2.1

Introduction

This chapter presents the stress analysis of a thick walled pipe subjected to thermal and mechanical loads. This problem is commonly observed in piping and components of thermal power plant facilities. The fluid that flows inside the pipe changes temperature and pressure during operational transients[1]. This creates, along the time, variation in mechanical stresses caused by internal pressure and variation in the thermal stresses caused by the temperature gradient induced in the pipe wall due to the change in temperature of the internal fluid.

The resulting mechanical and thermal stresses are independent of each other as long as the principal of linear superposition holds true, e.g. the analysis is linearly elastic. That is why they are calculated separately. The final result is obtained by superposing the results (mechanical plus thermal stresses).

This chapter also presents the concept known as stress linearization, used in the ASME Code to perform the simplified elasto-plastic fatigue assessment. To apply the stress linearization procedure, it is necessary to fully determine the mechanical and thermal stress distributions along the component's wall.

In order to determine these stress distributions, the fluid temperature and pressure time histories must be known. **Figure 2.1** shows the fluid pressure and temperature time histories that will be used in this chapter. These histories started on 10/15/2012 at 3:16 p.m. and ended on 10/16/2012 at 8:43 p.m. They represent a generic power plant pipe component's measured history that occurred during the plant's startup and shut down periods. In the present case, temperature and pressure values were measured and recorded within a 60 second interval.

[1] Particularly, the combination of constant internal pressure and transient thermal loading is very common.

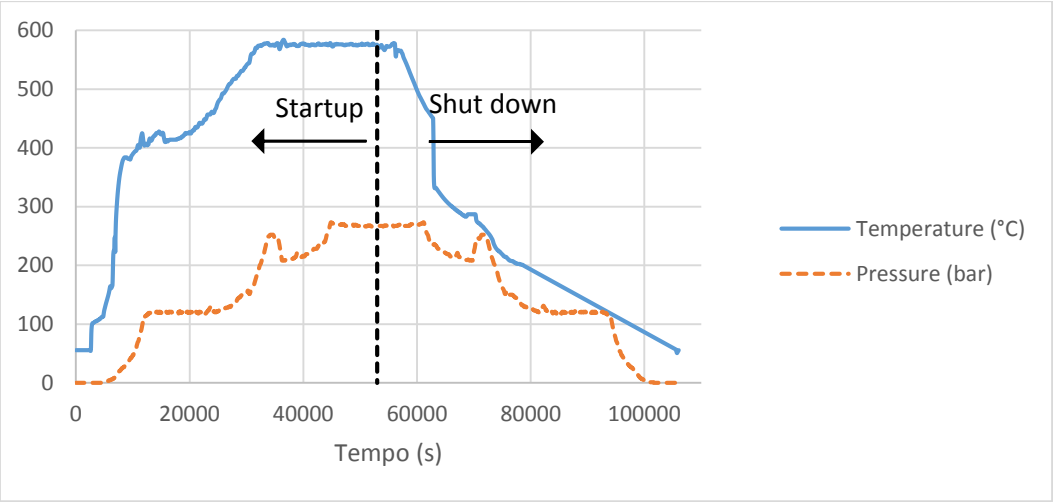

Figure 2.1: History of temperature and pressure.

The pipe's material and geometric properties used in this example are: modulus of elasticity (E) = 210 GPa, Poisson's ratio (v) = 0.3, thermal conductivity (λ) = 33 $W/(m \cdot K)$, coefficient of thermal expansion (α_T) = 12,9 $\cdot 10^{-6}\,°C^{-1}$, specific heat (c) = 622 $J/(kg \cdot K)$, density (ρ) = 7760 kg/m^3, internal radius (r_i) = 100 mm and outer radius (r_o) = 212 mm.

Another important parameter in the thermal solution is the fluid's heat transfer coefficient (h). The heat transfer coefficient can be given in terms of a time history, as shown in **Figure 2.1**, for temperature and pressure. However, in this chapter, the coefficient was assumed to be constant throughout the operation, since it did not present a significant variation over the range of the fluid's temperature. The heat transfer coefficient used in this chapter is equal to 1000 W/m^2K.

2.2
Mechanical Solution

The mechanical stress solution is given by using the Lame's equations for thick walled pipes subjected to internal and external pressure:

$$\sigma_r(r) = \frac{p_i r_i^2 - p_o r_o^2}{r_o^2 - r_i^2} - \frac{r_i^2 r_o^2 (p_i - p_o)}{r^2 (r_o^2 - r_i^2)} \tag{2.1}$$

$$\sigma_\theta(r) = \frac{p_i r_i^2 - p_o r_o^2}{r_o^2 - r_i^2} + \frac{r_i^2 r_o^2 (p_i - p_o)}{r^2 (r_o^2 - r_i^2)} \tag{2.2}$$

$$\sigma_z = \frac{p_i r_i^2 - p_o r_o^2}{r_o^2 - r_i^2} \tag{2.3}$$

where σ_r is the radial stress, σ_θ is the circumferential stress, σ_z is the longitudinal stress, r_o is the external radius, r_i is the internal radius, p_o is the external pressure, and p_i is the internal pressure (which, in the case studied here, is equal to the history of the internal pressure shown in **Figure 2.1**).

In equations (2.1) and (2.2) one can see that the radial and circumferential stresses are functions of the radial coordinate. Therefore, it is possible to calculate the distribution of stress along the pipe's thickness, which is a prerequisite for performing the stress linearization. Equation (2.3) is not a function of the radial coordinate because the longitudinal stress is constant along the thickness of the pipe.

Using the Lame's equations, the pipe's geometric properties and the load history presented in **Figure 2.1** it is possible to calculate the stress components that the pipe is subjected during the startup and shut down periods of the plant. **Figure 2.2** shows the history of the stress components acting on the inner wall of the pipe. **Figure 2.3** shows the stress distribution along the thickness of the pipe that occurred at the time step of 5:23 p.m. on 10/15/2012. As will be shown during the calculation of the thermal stress solution, this is the critical time step to be considered in the fatigue assessment.

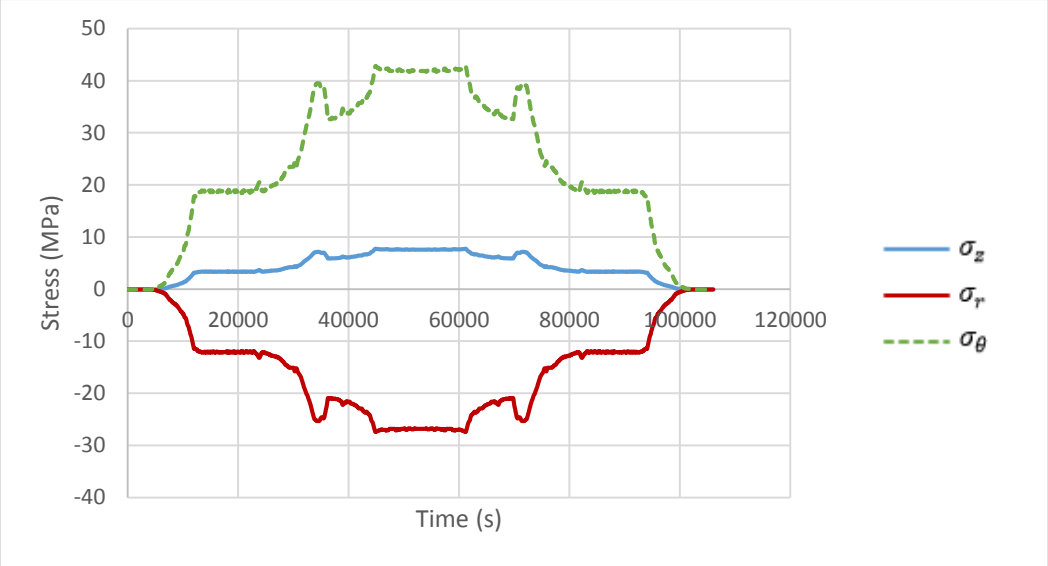

Figure 2.2: History of mechanical stresses calculated on the inner wall of the pipe.

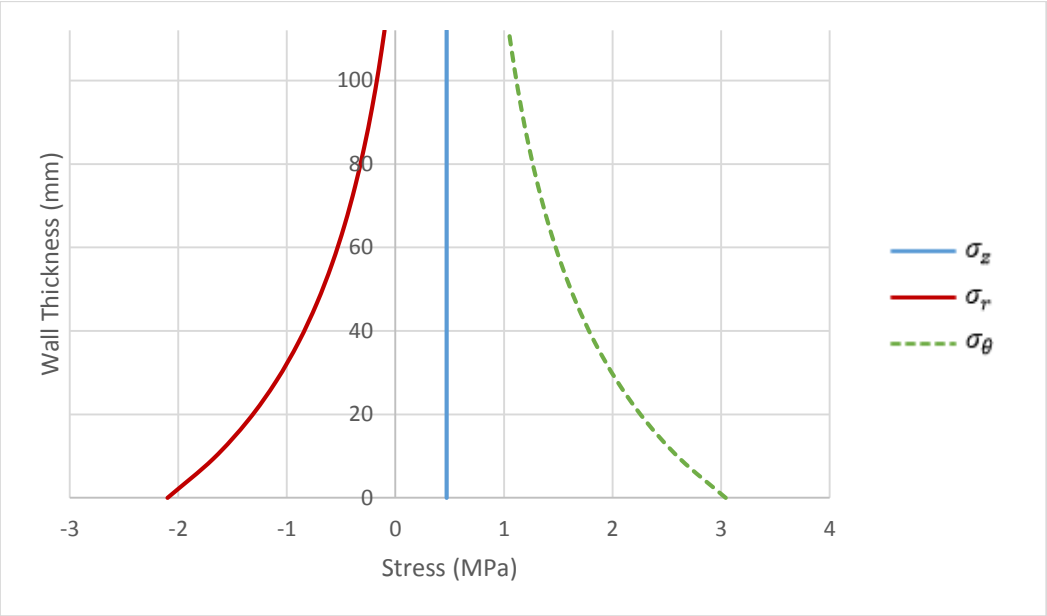

Figure 2.3: Distribution of the mechanical stresses along the wall thickness at the time step of 5:23 p.m. on 10/15/2012.

2.3
Thermal Solution

The thermal solution is not as simple as the mechanical solution. Mechanical stresses acting at each time step are function of the pressure at the respective time step. Thermal stresses acting at each time step are function of the temperature distribution across the pipe's thickness at the respective time step.

Therefore, it is necessary to calculate the temperature distribution across the thickness at each time step. What hampers the thermal stress solution is the fact that this temperature distribution is not only a function of the temperature at the time step being considered, but it also depends on the temperature history that occurred prior to this time step. Hence, it is a thermal transient calculation.

This problem is usually solved using a finite element analysis. However, the finite element analysis normally consumes too much computational time to evaluate the final result. For that reason, this chapter proposes an analytical approach developed by Albrecht [5]. In this thesis, the Albrecht's closed form solution was developed in such a way as to end up with a fast and accurate evaluation of the thermal stresses involved in this problem.

Since this method is not commonly employed, and its use for the present purpose was not found in the literature, it is necessary to guarantee the validity of the proposed procedure. Thus, the example was solved using a finite element

analysis in such a way that the analytical results could be checked using the finite element results.

Albrecht proposed several solutions to this problem in [5]. Two of those are explained in the following paragraphs.

2.3.1

Albrecht's First Solution

Albrecht's first solution was developed in such a way that stresses can be calculated directly from the temperature gradient of the fluid without calculating the temperature distribution. All the calculations that lead to this equation are available in reference [5]. The solution consists of two equations:

$$\sigma_{\theta i}(t) = \sigma_{zi}(t) = \frac{\alpha_T \cdot E \cdot \Delta T}{1-v} \sum_{n=1}^{\infty} A_n e^{-a \cdot k_n^2 \cdot t} \tag{2.4}$$

$$\sigma_{\theta o}(t) = \sigma_{zo}(t) = \frac{\alpha_T \cdot E \cdot \Delta T}{1-v} \sum_{n=1}^{\infty} B_n e^{-a \cdot k_n^2 \cdot t} \tag{2.5}$$

where equation (2.4) is the solution for the circumferential and longitudinal stresses acting on the inner wall, and equation (2.5) is the solution for the circumferential and longitudinal stresses acting on the outer wall. In both equations, t is the time in seconds and a is the factor of thermal diffusivity (m^2/s).

$$a = \frac{\lambda}{\rho \cdot c} \tag{2.6}$$

The constants A_n and B_n are given by the following equations:

$$A_n = \frac{2\left[\frac{2r_i^2}{r_i^2 k_n^2 \left(r_o^2 - r_i^2\right)} - \frac{\lambda}{h \cdot r_i}\right]}{\left[1 + \left(\frac{r_i k_n \lambda}{h \cdot r_i}\right)^2\right] - \frac{\left[\left(\frac{r_i k_n \lambda}{h \cdot r_i}\right) \cdot J_1(r_i k_n) + J_0(r_i k_n)\right]^2}{J_1^2(r_o k_n)}} \tag{2.7}$$

$$B_n = \frac{\frac{2r_i}{r_o J_1(r_o k_n)}\left[\frac{J_1(r_i k_n)}{h \cdot r_i/\lambda} + \frac{J_0(r_i k_n)}{r_i k_n}\right] - \frac{4r_i^2}{(r_o^2 - r_i^2) r_i^2 k_n^2}}{\left[1 + \left(\frac{r_i k_n \lambda}{h \cdot r_i}\right)^2\right] - \frac{\left[\left(\frac{r_i k_n \lambda}{h \cdot r_i}\right) \cdot J_1(r_i k_n) + J_0(r_i k_n)\right]^2}{J_1^2(r_o k_n)}} \tag{2.8}$$

where $J_\alpha(x)$ is the Bessel function of the first kind, $Y_\alpha(x)$ is the Bessel function of the second kind, and the n values of k_n are obtained by finding the n ($n = 1, 2, 3, ...$) roots of the following equation:

$$[\lambda \cdot k_n \cdot J_1(r_i \cdot k_n) + h \cdot J_0(r_i k_n)] \cdot Y_1(r_o k_n) - [\lambda \cdot k_n \cdot Y_1(k_n r_i) + h \cdot Y_0(k_n r_i)] \cdot J_1(r_o k_n) = 0 \quad (2.9)$$

With these equations, it is possible to calculate the thermal stresses on the inner and outer surfaces of the thick walled pipe.

A numerical solution algorithm was implemented in order to calculate the stresses. The solution's first step consists in admitting that, at the first time step, the stresses are equal to zero.

The second step of the routine considers the first interval between the first and second time steps. The mean heat transfer coefficient is found for this interval, between these two time steps.[2] Using the geometrical and material properties of the pipe, equation (2.9) is solved using the Newton-Raphson algorithm to find the first root k_n. Using this value, equations (2.7) and (2.8) are solved with n equal to one.

The routine continues finding the roots k_n and calculating the values of A_n and B_n until the difference between the preview values of the summations of equations (2.4) and (2.5) and the current values of the summations reach a prescribed tolerance (this tolerance was made equal to 10^{-4}).

For example, after calculating M roots k_n, the M values of A_n and B_n, and defining the values of the summations as X_{M_A} and X_{M_B}, the routine calculates the next root and the next values of A_n and B_n. The values of the summations with M + 1 roots can be defined as X_{M+1_A} and X_{M+1_B}. If the difference between X_{M_A} and X_{M+1_A} and the difference between X_{M_B} and X_{M+1_B} are less than 10^{-4}, the routine stops and returns the values of the summations of equations (2.4) and (2.5) using the M roots and M values of A_n and B_n.

The temperature gradient (ΔT) is obtained as the difference in temperature between the first and second time steps. Using the above procedure, it is possible to fully solve equations (2.4) and (2.5). At this stage of the procedure, only the stresses caused by the first interval are considered. However, the temperature

[2] Even with the heat transfer coefficient being constant in the problem (presented in this thesis), the algorithm developed herein was implemented in such a way that histories where this coefficient varies through time can be solved as well.

gradient that occurs in the first interval will cause stress at the second time step and at the time steps that follow. Consequently, it is necessary to calculate the history of stresses caused by the first interval, as is observed in **Figure 2.4**. This result can be accomplished by solving equations (2.4) and (2.5) for all the time steps in the history, changing the parameter t, needed in the cited equations, to the respective time of each time step.

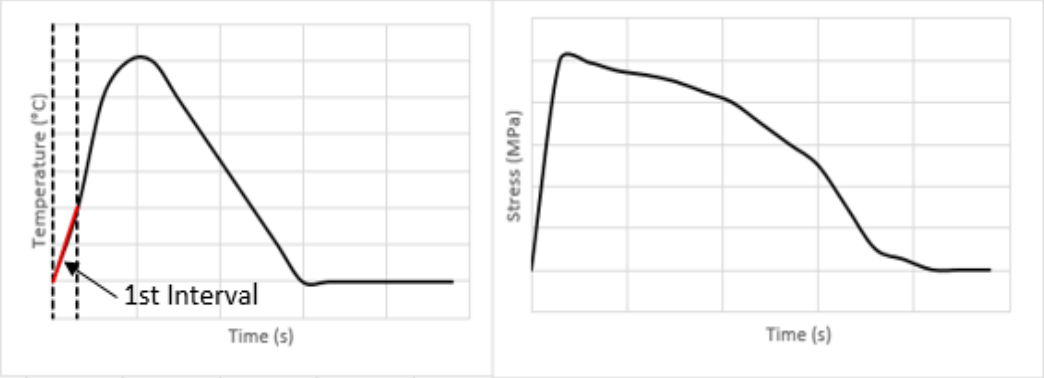

Figure 2.4: Schematic chart of one stress component history calculated using the first temperature interval.

The routine continues to the second stage, repeating the same procedure with the second interval and resulting in another stress history, which is now equal to zero at the first and second time steps. An example of the resulting stress history is shown in **Figure 2.5**.

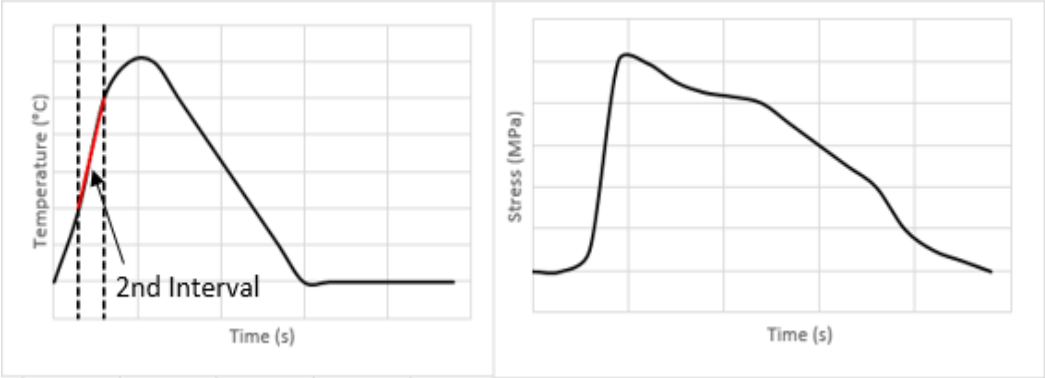

Figure 2.5: Schematic chart of a stress component history calculated using the second temperature interval.

The procedure continues until all the intervals are evaluated. After that, all the stress histories (using the first, second, third, …, and last intervals) are added up in order to provide the final result. The limitation regarding Albrecht's first solution is due to the fact that it is only possible to calculate the stresses on the inner and outer walls. Since this precludes the stress linearization procedure, another solution is presented.

2.3.2

Albrecht's Second Solution

Albrecht's second solution does not calculate the stresses directly. Before calculating the stresses, the temperature distribution along the thickness is required. This distribution is obtained using the following equation:

$$T(r,t) = T_0 - T_0 \pi h \sum_{n=1}^{\infty} \frac{J_0(r\,k_n)[\lambda\,k_n\,Y_1(r_i\,k_n)+h\,Y_0(r_i\,k_n)]-Y_0(r\,k_n)[\lambda\,k_n\,J_1(r_i\,k_n)+h\,J_0(r_i\,k_n)]}{(\lambda^2 k_n^2+h^2)-\frac{[\lambda\,k_n\,J_1(r_i\,k_n)+h\,J_0(r_i k_n)]^2}{J_1^2(r_o k_n)}} \cdot$$

$$\cdot\, e^{-a\cdot k_n^2\cdot t} \qquad (2.10)$$

where T_0 is the initial temperature, and k_n are the roots of equation (2.9). A procedure similar to the one explained previously (during Albrecht's first solution) was implemented to solve this equation. The major differences between the two procedures are:

- The goal of the second procedure is not to obtain the stresses in a first step, but the transient temperature distribution.
- The assumption that the value at the first time step of the interval being evaluated is equal to zero is no longer valid. The value of the first time step is now equal to its initial temperature.
- The equation to be solved (equation (2.10)) is a function of the radial position. Thus the thickness of the pipe is divided into ND parts of the same size.
- The values of the summation in equation (2.10) are now the ones used to reach the given tolerance.

The temperature distribution is obtained by repeating, at each one of the ND+1 divisions of the pipe, the explained procedure for the Albrecht's first solution using the above modifications. **Figure 2.6** presents a flowchart of the routine for a better visualization of the procedure.

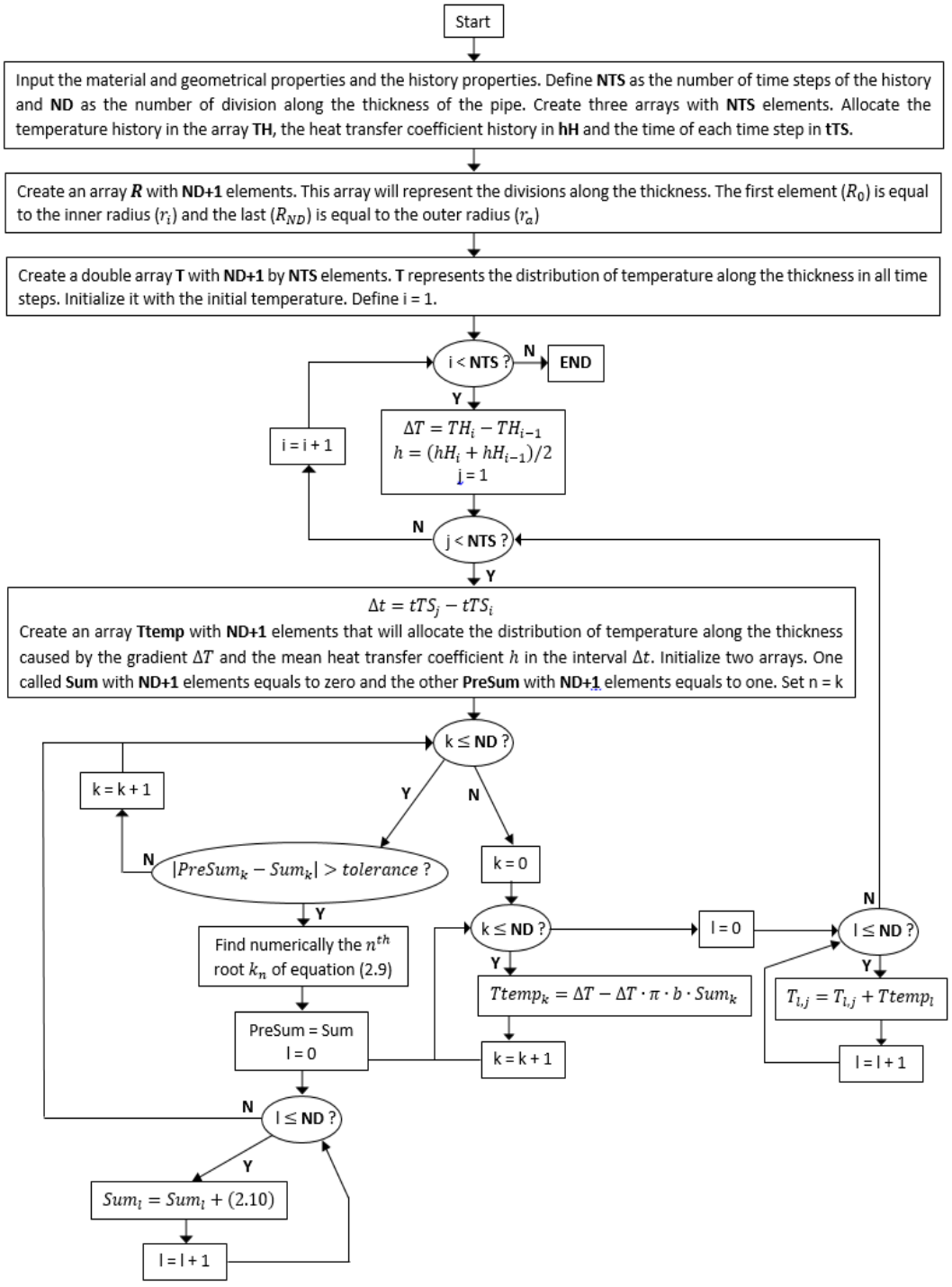

Figure 2.6: Flowchart of the algorithm that solves Albrecht's second solution.

After calculating the temperature distribution along the thickness, the stresses are calculated using the following equations:

$$\sigma_r(r,t) = \frac{\alpha_T E}{1-\nu}\left[\frac{r^2-r_i^2}{r^2(r_o^2-r_i^2)}\int_{r_i}^{r_o} T(r,t)\, r\, dr - \frac{1}{r^2}\int_{r_i}^{r} T(r,t)\, r\, dr\right] \qquad (2.11)$$

$$\sigma_\theta(r,t) = \frac{\alpha_T E}{1-\nu}\left[\frac{1}{r^2}\int_{r_i}^{r} T(r,t)\, r\, dr + \frac{r^2+r_i^2}{r^2(r_o^2-r_i^2)}\int_{r_i}^{r_o} T(r,t)\, r\, dr - T(r,t)\right] \quad (2.12)$$

$$\sigma_z(r,t) = \frac{\alpha_T E}{1-\nu}\left[\frac{2}{r_o^2-r_i^2}\int_{r_i}^{r_o} T(r,t)\, r\, dr - T(r,t)\right] \quad (2.13)$$

Since the temperature values along the thickness are obtained discreetly, the integrations are solved using the trapezoidal rule.

2.3.3
Finite Element Solution

The finite element solution was implemented using the ANSYS® software. The simulation used a 2D axisymmetric analysis. Since the finite element solution was implemented in 2D, a rectangle was drawn to represent the pipe (**Figure 2.7 (a)**). The rectangle is 112 mm in width and 1000 mm in height, where the left side of the rectangle is 100 mm from the Y axis. Using that and the axisymmetric on the Y axis, the representation of the pipe is obtained.

The height of the rectangle represents the length of the pipe. The results of the simulations, used for comparison with the analytical results, were obtained in the nodes at the middle of the mesh (**Figure 2.7 (c)**). Hence, a very long pipe was simulated so that it would not be necessary to select any boundary conditions.

The finite element solution was separated into two different solutions; the first one was a thermal transient solution, where a convective load was selected for the inner wall of the pipe (**Figure 2.7 (b)**). The input load required for this kind of solution is the temperature and heat transfer coefficient history. The result of this analysis is the temperature history in all the nodes at every time step.

The thermal transient solution results are used in the mechanical static analysis, i.e. the temperature distribution along the pipe at each time step is analyzed as a static problem. The result of this analysis is the thermal stresses for each node at every time step.

The meshes used in the thermal and mechanical solutions were the same (**Figure 2.7 (a)**). The mesh refinement and the step size selection used in the thermal transient solution were accomplished by observing the progressive changes in the results acquired at the node indicated in **Figure 2.7 (c)**. The mesh and the transient's step sizes were refined until there were no longer any significant changes in the final stress results observed in this node.

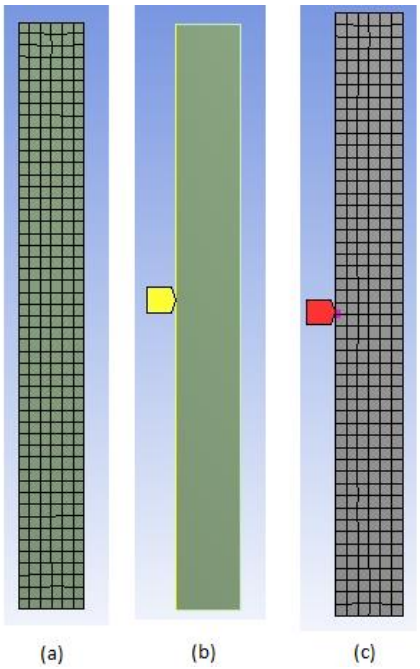

Figure 2.7: (a) Mesh used in the simulation; (b) edge where the convection load was applied; (c) node where the results were obtained.

It is important to point out that optimizing the time consumed on the finite element analysis was not within the scope of this work. The goal herein is to verify if the analytical solutions proposed in the subchapters regarding Albrecht's first and second solutions were accurate enough to solve the problem. In cases where the optimizing the time on the finite element solution is important, simulations with optimized meshes and shorter specimen lengths should be pursued.

2.3.4

Thermal Results

The analytical and finite element solutions were compared to validate the former results. First, a simple temperature history was used. The history started with pipe and fluid in equilibrium at 50°C. Then the fluid was heated up to 270°C and maintained at that temperature, configuring a temperature change caused by a step impulse. The heat transfer coefficient was kept constant and equal to 1000 W/m^2K.

The material and geometrical properties used were cited previously.

The results of the three solutions for the inner wall of the pipe were compared: Albrecht's first solution equation (2.4); Albrecht's second solution, equations (2.12) and (2.13); the finite element solution results at the node marked with a red flag in **Figure 2.7 (c)**.

The agreement of this comparison led to the second stage of comparison. That it used the more complex history presented in **Figure 2.1**.

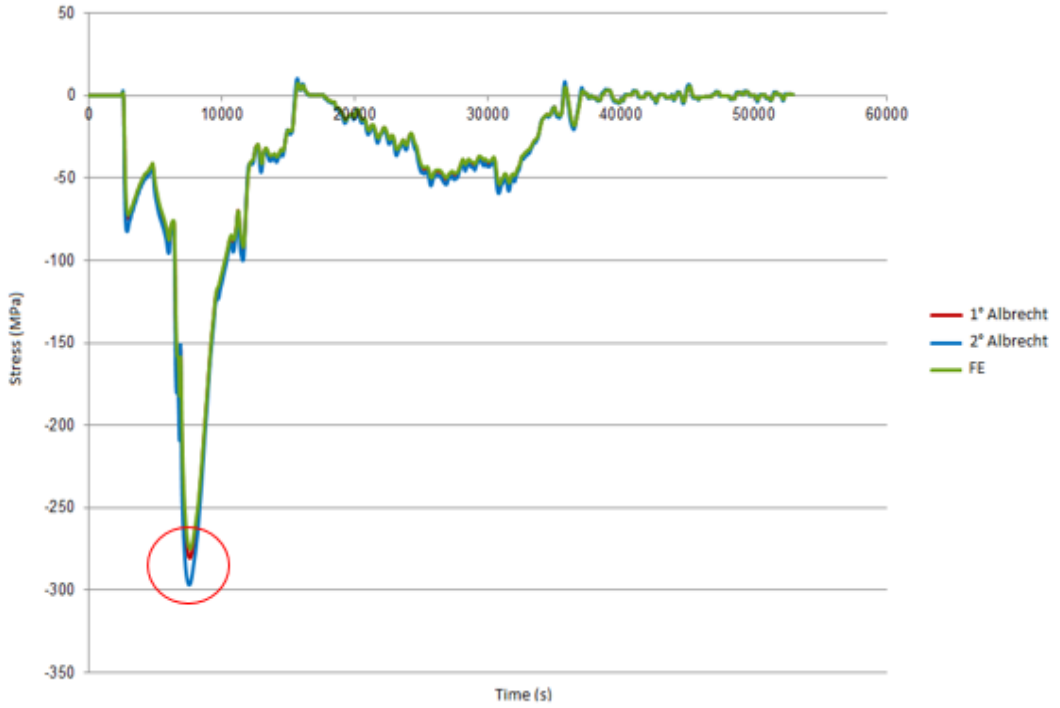

Figure 2.8: History of the circumferential stress during the startup period.

The results once again were similar; the history of circumferential stress for the startup period of operation, using the three proposed solutions, is presented in **Figure 2.8**. One can see that the results were very similar. It is even difficult to notice the difference between them, especially Albrecht's first solution.

The largest difference among the three solutions can be observed at the red circle in **Figure 2.8**. At this instant in time, the stress values are the highest, and it is possible to note that the Albrecht's solutions give results slightly more conservative than the FE solution.

Based on the facts that Albrecht's first solution precludes stress linearization and that Albrecht's second solution was faster at calculating the result for the time interval (23.25 seconds), one can conclude that Albrecht's second solution was the best one for the component fatigue assessment.

Aspects to highlight from the previous paragraphs and from observing **Figure 2.8** and **Figure 2.2** are: the thermal stress solution is more complex than the mechanical solution, and the values of the thermal stresses are significantly higher than the values of the mechanical stresses.

Using Albrecht's second solution, the thermal stress components acting on the inner wall were calculated along the entire temperature history. The history of thermal stresses is presented in **Figure 2.9**.

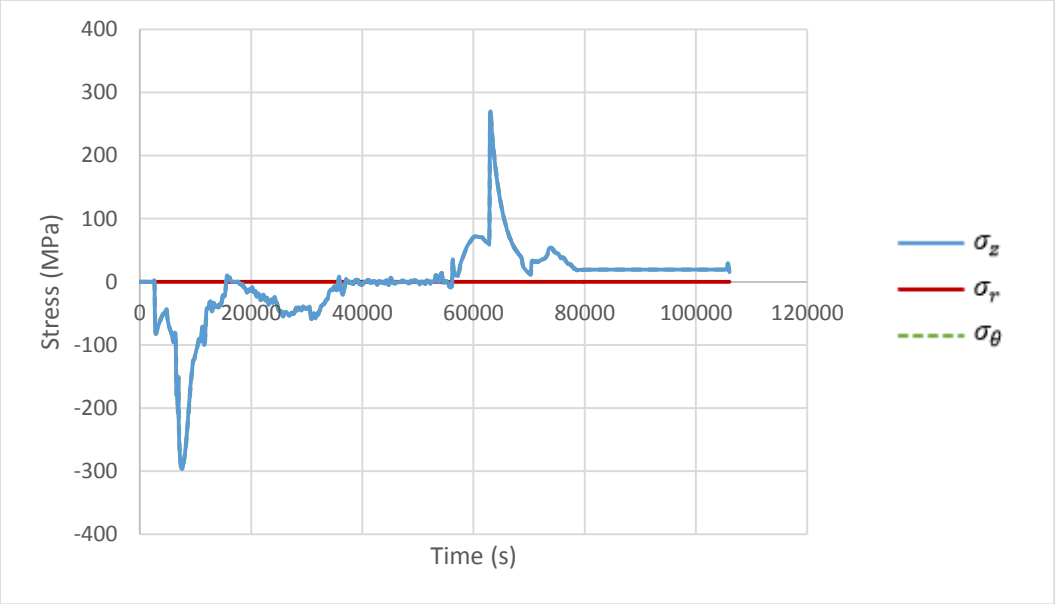

Figure 2.9: History of thermal stresses calculated on the inner wall of the pipe using the Albrecht's second solution.

From **Figure 2.9** one can see that the circumferential and longitudinal stresses are equal - as they should be according to equation (2.4) derived from the Albrecht's first solution. In addition, the radial stress is always equal to zero on the inner wall of the pipe, as expected.

Figure 2.10 shows the distribution of stresses across the thickness of the pipe at the time step referent to 5:23 p.m. on 10/15/2012, which is the critical time step marked with a red circle in **Figure 2.8**. The critical time step for the thermal solution is equal to the critical time step for the final solution, since the critical stress values for the mechanical solution are almost irrelevant when compared with the critical stress values for the thermal solution.

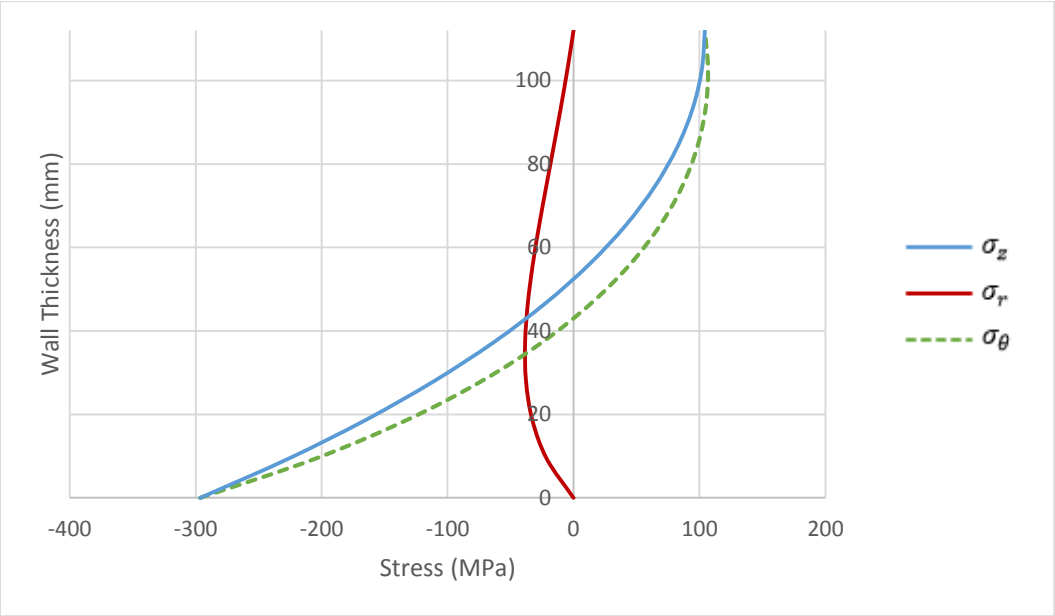

Figure 2.10: Distribution of the thermal stresses along the wall thickness at time step of 5:23 p.m. on 10/15/2012 using Albrecht's second solution.

One can see in **Figure 2.10** that the circumferential and longitudinal stresses are equal and that the radial stress is zero only on the inner and outer walls. This is not true along the thickness of the pipe and may lead to different circumferential and longitudinal stress values on the inner and outer walls for the linearized stresses.

After having calculated the mechanical and thermal solutions, it is possible to obtain the final result, obtained by superposing both solutions. **Figure 2.11** shows the history of stresses on the inner wall (summation of the results in **Figure 2.9** and **Figure 2.2**). **Figure 2.12** presents the stress distributions across the thickness of the wall pipe at the critical time step (summation of the results in **Figure 2.10** and **Figure 2.3**).

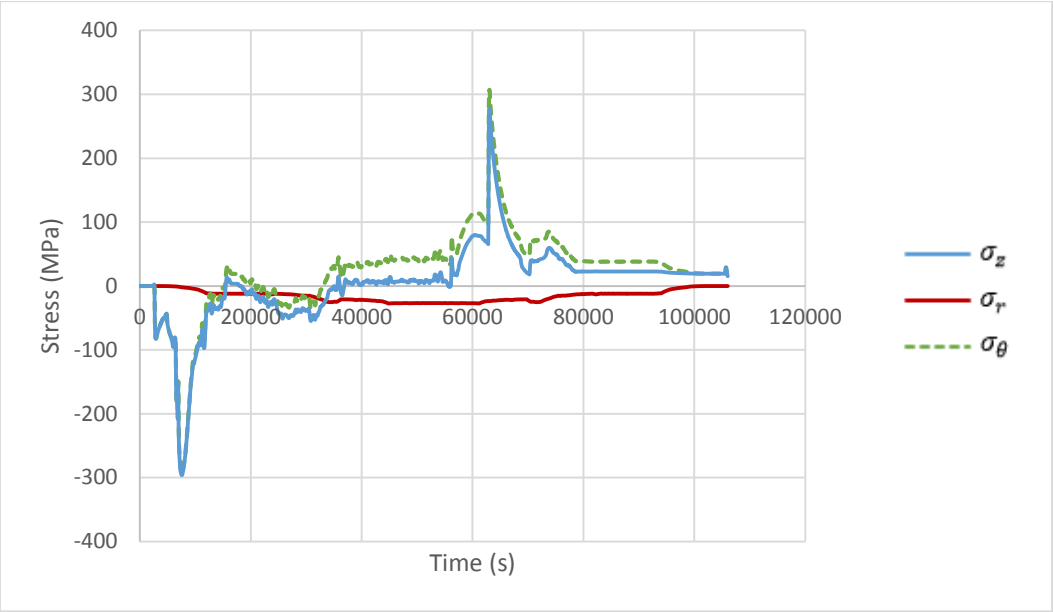

Figure 2.11: History of thermal plus mechanical stresses calculated on the inner wall of the pipe.

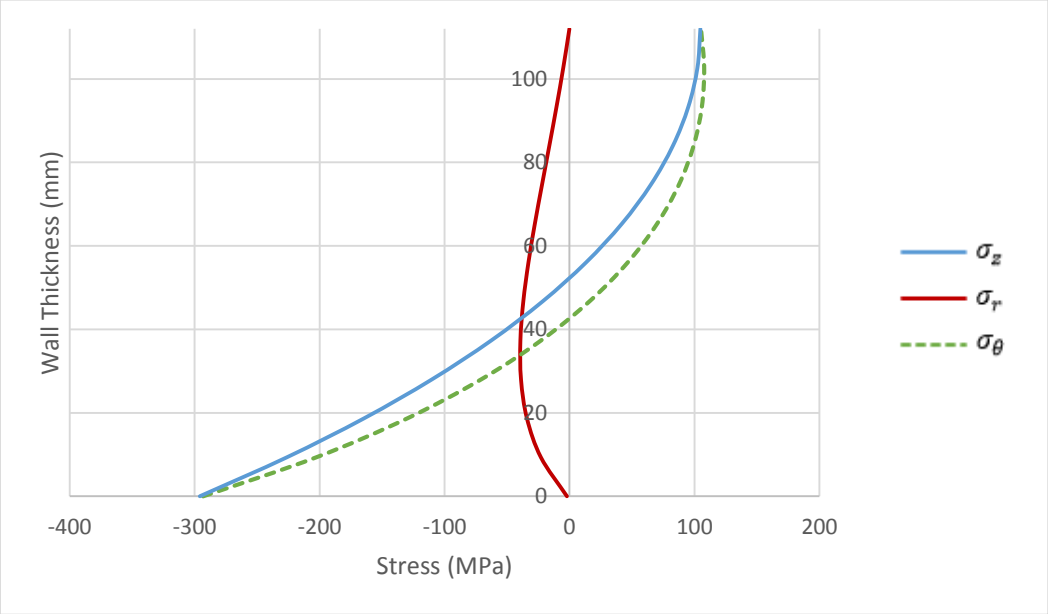

Figure 2.12: Distribution of the thermal plus mechanical stresses along the wall thickness at the time step of 5:23 p.m. on 10/15/2012.

In **Figure 2.11**, it is possible to observe that the mechanical stresses make the circumferential and longitudinal stresses no longer equal to each other on the inner and outer walls, and that the radial stress is no longer zero.

Even with the mechanical stresses being small when compared with the thermal stresses, it is the mechanical part that is responsible for making the history of the stresses present values non-proportional with each other (although principal stress directions remain unchanged). At this point, it is necessary to define a non-proportional history.

A loading with fixed principal stress directions is said to be a proportional history, even if the principal stresses value changes in a non-proportional manner. A non-proportional history is defined as a history where the principal directions change along the time. Using these definitions, the history shown in the pipe example is proportional, although it is possible to observe that the stress value changes are non-proportional to each other.

2.4
Stress Linearization

The stress linearization method is proposed by the ASME Code in a way that allows fatigue assessment by using an elastic finite element analysis, even when loading causes plastic behavior. The procedure is called simplified elasto-plastic fatigue analysis. Stress linearization is required to calculate the standard plasticity correction factor K_e.

Full stress distributions are usually obtained by means of finite element analysis. The application of a stress linearization process through the thickness of a specific section of the component makes it possible to determine the membrane, bending and peak stress components that are used to calculate equivalent stresses, which is used later in the fatigue analysis procedure recommended by the ASME Code [Section VIII – Div.2 – Annex 5].

The linearized stress components can be calculated using the following equations:

$$\sigma_{ij,m} = \frac{1}{t}\int_0^t \sigma_{ij} dx \tag{2.14}$$

$$\sigma_{ij,b} = \frac{6}{t^2}\int_0^t \sigma_{ij}\left(\frac{t}{2} - x\right) dx \tag{2.15}$$

$$\sigma_{ij,P}(x)|_{x=0} = \sigma_{ij}(x)|_{x=0} - \left(\sigma_{ij,m} + \sigma_{ij,b}\right) \tag{2.16}$$

$$\sigma_{ij,P}(x)|_{x=t} = \sigma_{ij}(x)|_{x=t} - \left(\sigma_{ij,m} - \sigma_{ij,b}\right) \tag{2.17}$$

where t is the thickness of the selected cross section. Equation (2.14) calculates the membrane stress ($\sigma_{ij,m}$) in the ij direction, equation (2.15) calculates the bending stress ($\sigma_{ij,b}$) in the ij direction, and equations (2.16) and (2.17) calculate the peak stress ($\sigma_{ij,P}$) in the ij direction on the inner and outer walls, respectively.

It is important to note that the same stress linearization procedure can also be applicable for any known analytical solution.

In the thick-walled pipe case study discussed in this chapter, Albrecht's second solution gives the full stress component distribution as a function of the radial position on the pipe.

Using the trapezoidal rule to solve the integrations in equations (2.14) and (2.15), and also by solving equations (2.16) and (2.17), the results of Albrecht's second solution were linearized and compared with the linearization of the finite element solution given by the ANSYS® software. This software has a standard module to linearize the stresses; the algorithm is based on the same equations presented here.

The results of the analytical solution and the finite element solution were compared in order to verify the analytical solution, this time by means of the stress linearization procedure. In this case, only the thermal solutions were compared. Since the ANSYS® linearizes the stresses at one selected time step, the comparison was performed at the critical time step during the startup (time step on 10/15/2012 at 5:23 p.m.).

		$\sigma_{ij,m}$	$\sigma_{ij,b}$	$\sigma_{ij,P}(x)\|_{x=0}$	$\sigma_{ij,P}(x)\|_{x=t}$
σ_θ	Albrecht's 2nd	-0.62	-187.55	-108.24	-82.65
	ANSYS	-0.60	-168.49	-107.03	-74.03
σ_z	Albrecht's 2nd	-23.84	-199.23	-73.34	-71.12
	ANSYS	-21.76	-181.66	-77.40	-63.96
σ_r	Albrecht's 2nd	-23.22	-11.68	34.90	11.54
	ANSYS	-21.52	-11.46	29.58	10.20

Table 2.1: Linearization of the stresses (values in MPa).

In **Table 2.1** one can observe again that the values of Albrecht's second solution are similar when compared with the finite elements analysis, the analytical solution being slightly more conservative. These results validate the linearization of the stresses using the analytical solution.

In the fatigue analysis, The ASME Code uses two parameters that result from the stress linearization procedure: S_n, which is the addition of the primary plus secondary stresses, and S_p, which is the summation of the primary, secondary and peak stresses. The primary, secondary and peak stresses are categories of stresses.

Primary stress is separated into three subcategories:

- Primary General Membrane: described as the average stress across the solid section. It is only produced by mechanical loads, such as pressure and dead weight, and it excludes stresses caused by stress concentrations and discontinuities.
- Primary Local Membrane: similar to the Primary General Membrane. The difference is that the Primary Local Membrane considers stresses caused by discontinuities, but not stresses caused by stress concentrations.
- Primary Bending: the bending component of the primary stress. It is produced by mechanical loads, and excludes stresses caused by discontinuities and stress concentrations.

The secondary stress is not separated, and it considers the addition between the membrane and bending stresses. It is described as a self-equilibrating stress that is necessary to satisfy the continuity of the structure, and it is present in structural discontinuities. It can be caused by either mechanical or thermal loads, and it excludes stresses caused by local concentrations.

The peak category is described as the addition to the primary or secondary stress caused by the presence of a notch and/or certain thermal stresses that may cause fatigue but not distortion in the shape.

For a better categorization of the stresses, the code should be consulted. To summarize, in the problem presented here, the S_n stress is the summation of the membrane and bending stresses due to pressure and thermal loads calculated using equations (2.14) and (2.15), and the S_p stress is the summation of the membrane, bending and peak stresses.

Table 2.1 shows that the stresses in the inner wall of the pipe have the highest stress values. Hence, it can concluded that the critical part for the initiation and growth of a crack in the pipe is the inner wall. Consequently, a fatigue analysis is performed using the stresses acting at this location of the pipe.

The conclusion of this chapter is that, by using the mechanical solution and Albrecht's second solution for the thermal stress, it is possible to calculate all the stresses components along the thickness of the pipe. Thus, the stresses can be linearized and the S_n and S_p parameters needed for the ASME Code fatigue analysis are obtained.

One advantage of the method proposed here is that, unlike the finite element solution, S_n and S_p can be calculated along the given stress history for the entire period that the input (temperature, pressure and heat transfer coefficient history) is given. Using a finite element solution performed as the one shown, using ANSYS®, linearization is only possible at one selected time step.

The histories of the S_n and S_p stresses in the inner wall were calculated and are presented below. It is important to point out that the nomenclatures $S_{n,r}$, $S_{n,\theta}$, $S_{n,z}$ mean the S_n stress for the radial, circumferential and longitudinal components respectively, and that the nomenclature for the S_p stresses is analogous. This type of nomenclature is only allowed by Section VIII of the ASME code, since in Section III of the code the S_n and S_p stresses are defined using the principal stresses.

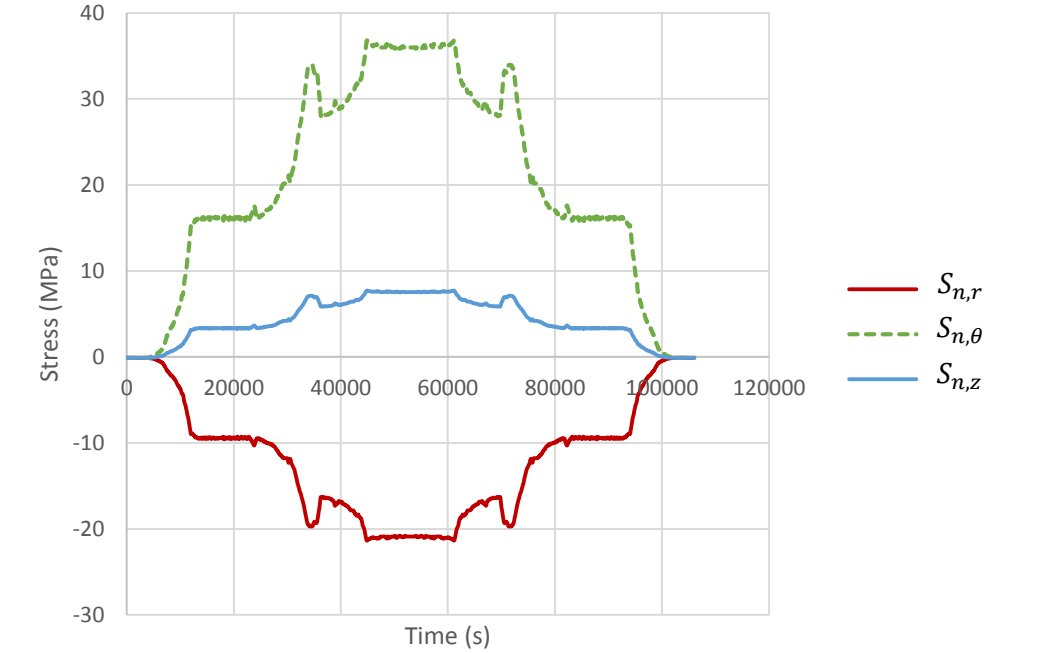

Figure 2.13: History of S_n stresses caused by the mechanical loads.

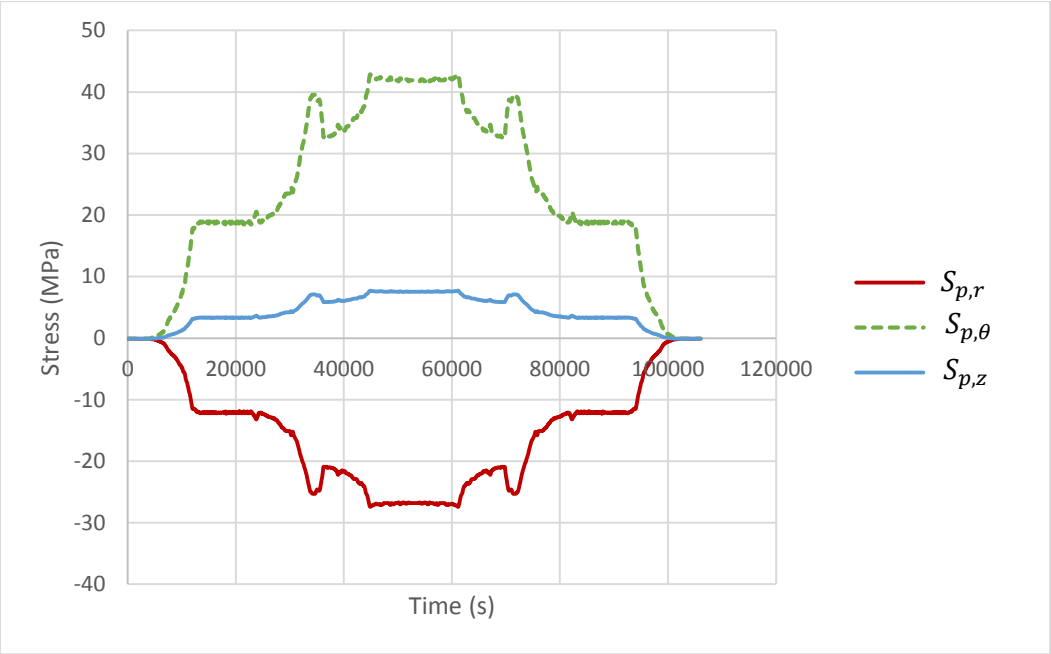

Figure 2.14: History of S_p stresses caused by the mechanical loads.

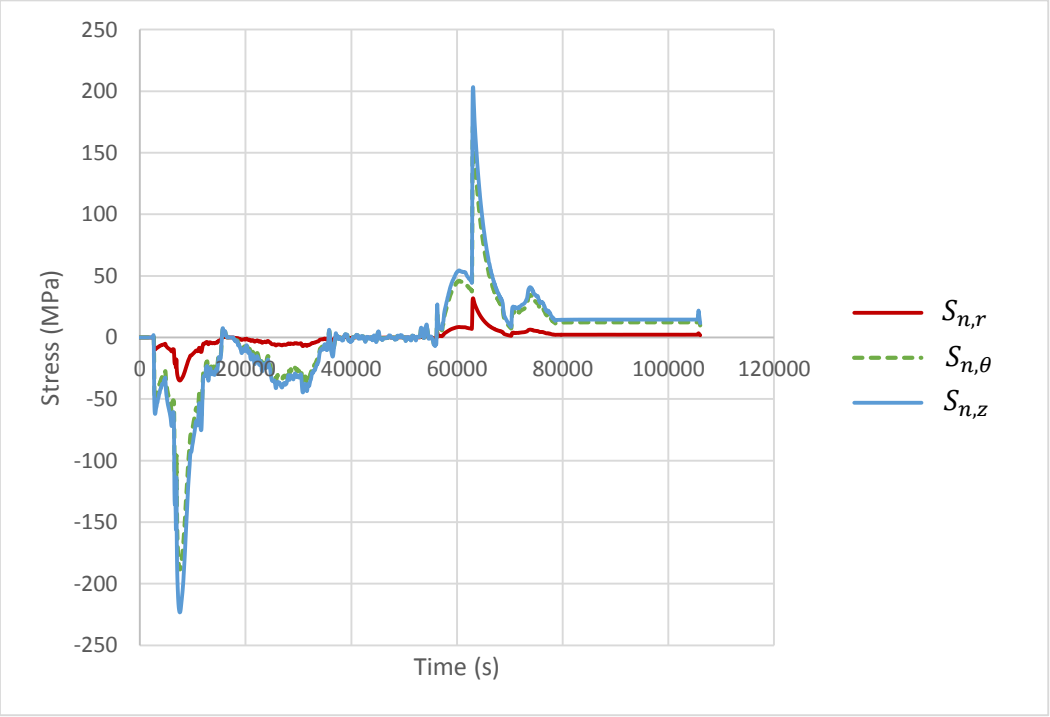

Figure 2.15: History of S_n stresses caused by the thermal loads.

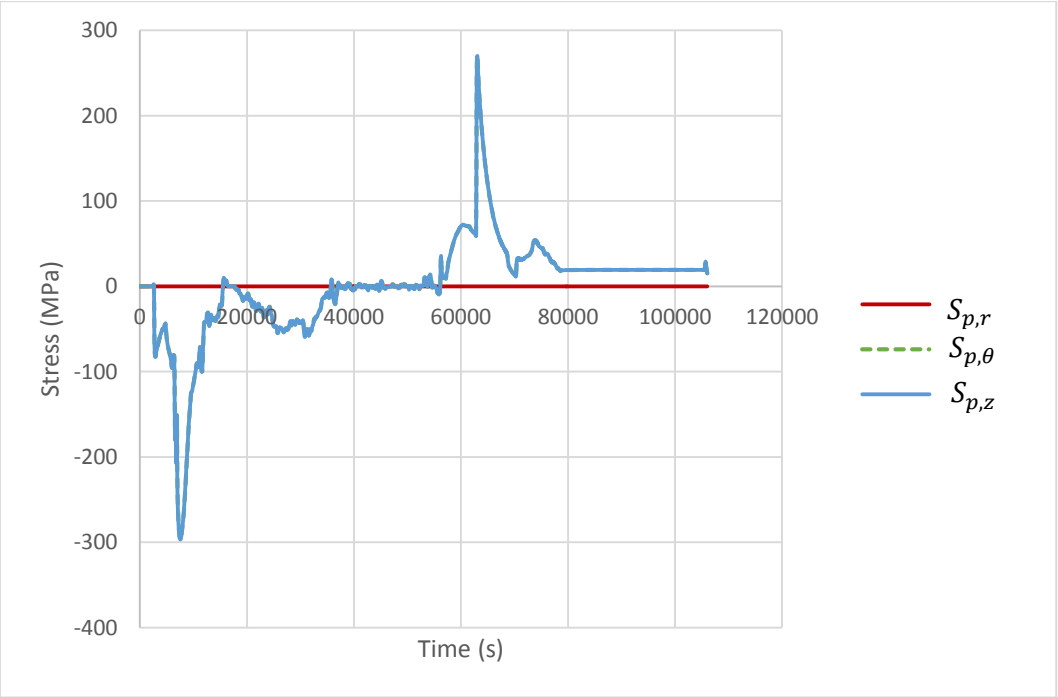

Figure 2.16: History of S_p stresses caused by the thermal loads.

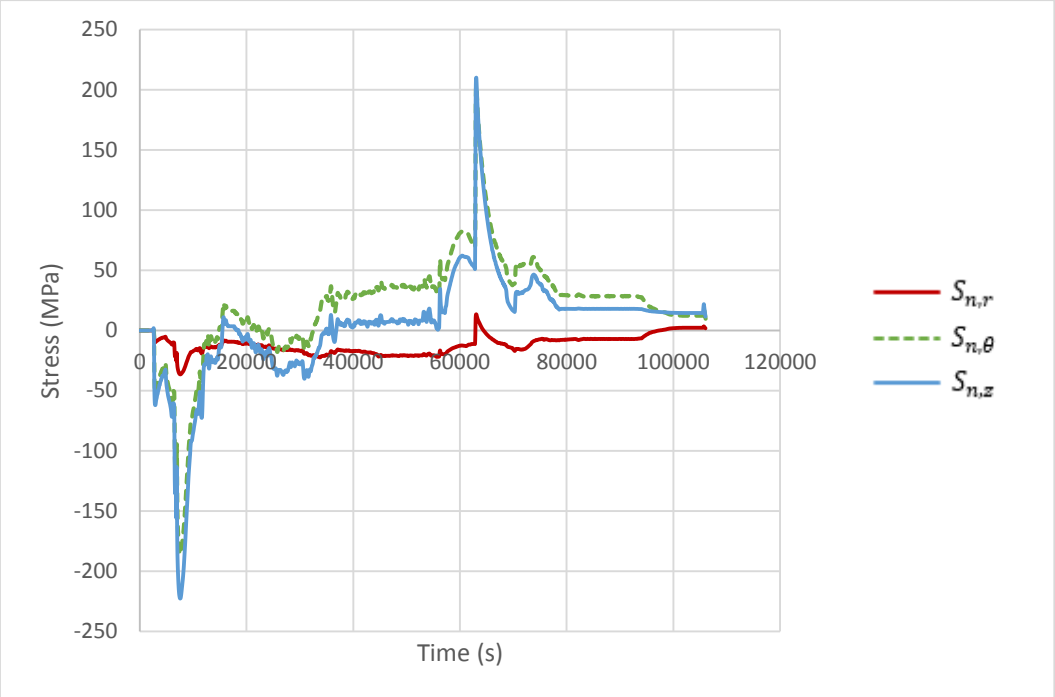

Figure 2.17: History of S_n stresses caused by the thermal plus mechanical loads.

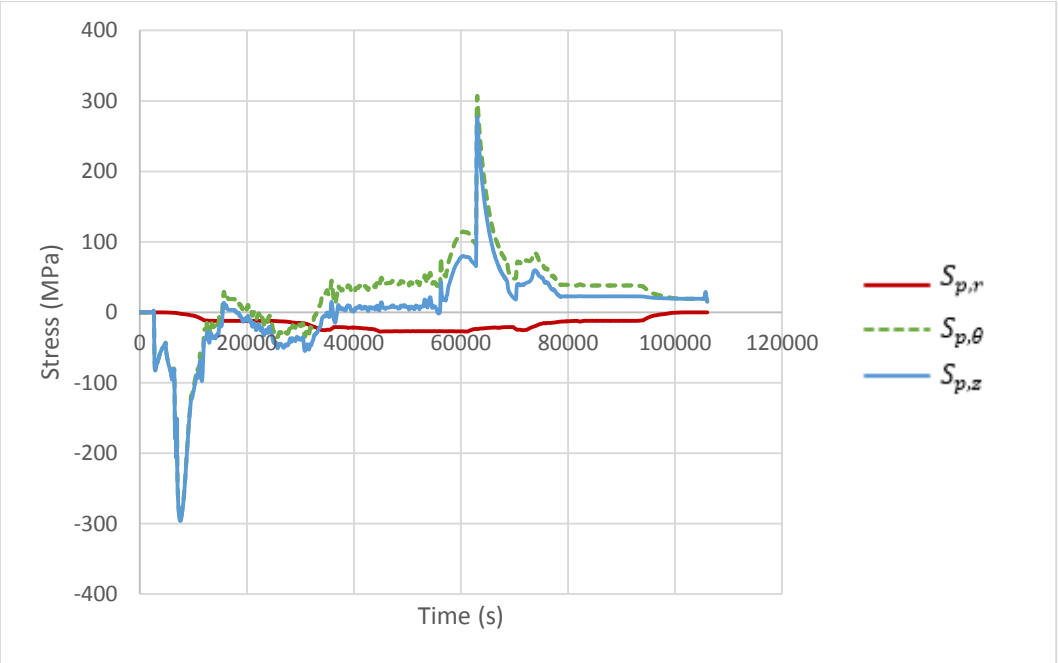

Figure 2.18: History of S_p stresses caused by the thermal plus mechanical loads.

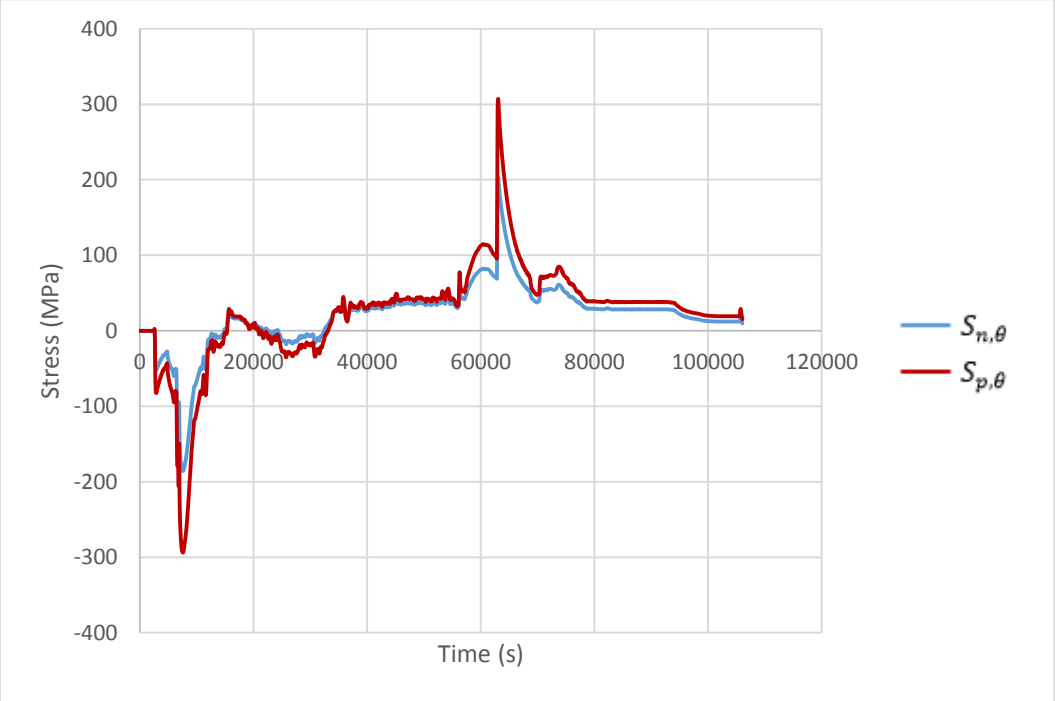

Figure 2.19: History of the circumferential stresses caused by the thermal plus mechanical loads.

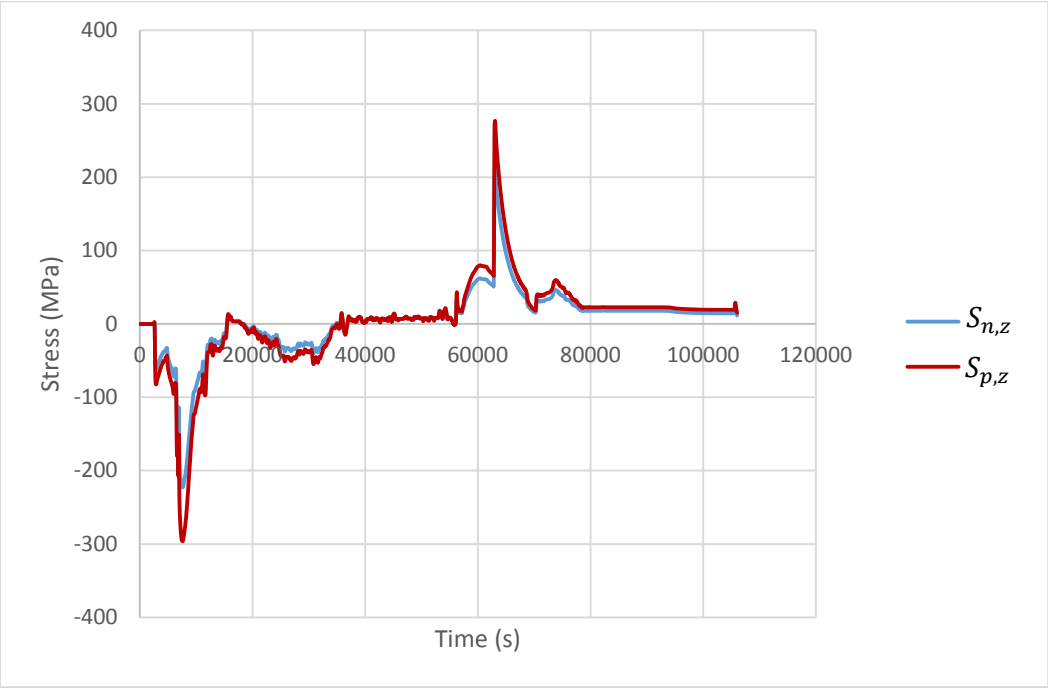

Figure 2.20: History of the longitudinal stresses caused by the thermal plus mechanical loads.

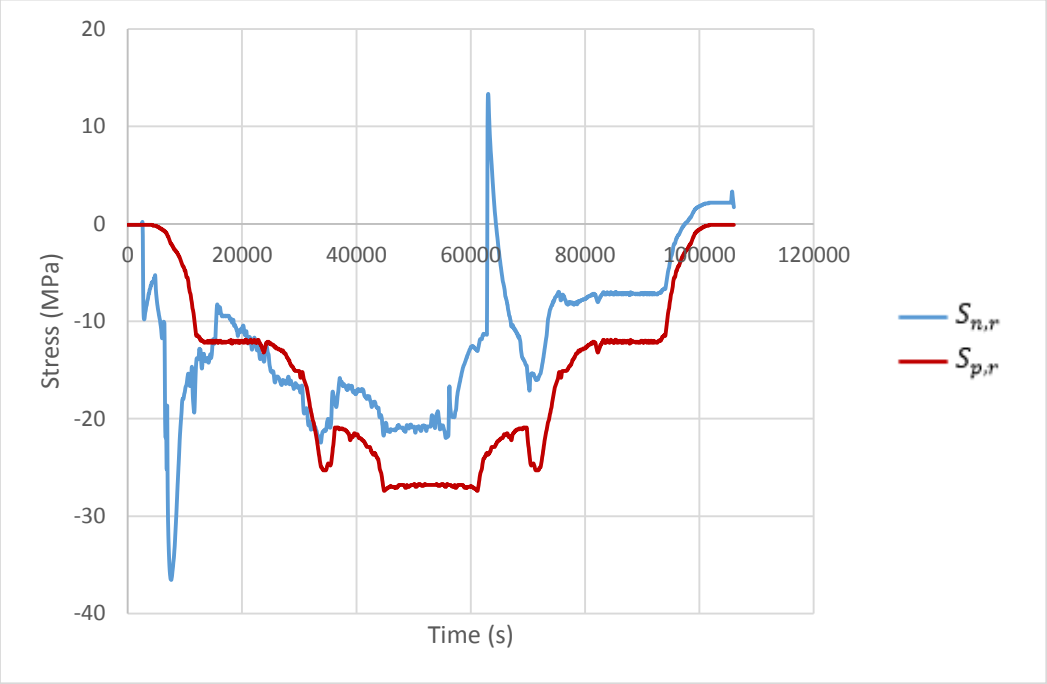

Figure 2.21: History of the radial stresses caused by the thermal plus mechanical loads.

3

Multiaxial Fatigue Damage Models

3.1

Damage Models

Fatigue damage models relate strain, or stress ranges or energy variables, to the number of cycles they actuate until a crack begins.

Damage models can be separated into three different groups: stress-based models, where the ranges of stress are related to the number of cycles required to initiate a crack; strain-based models, where the ranges of strain are related to the number of cycles needed to initiate a crack; and energy-based models, where the product of stress and strain is related to the number of cycles required to initiate a crack.

There are several stress-based models for multiaxial fatigue evaluation, such as the Sines [6], Findley [7], McDiarmid [8] and Dang Van [9] models, the last three models being applicable to non-proportional histories. Stress-based models are good for predicting high-cycle fatigue, where stresses are generally less than the material's yield strength, and the number of cycles required to initiate a crack is high.

With the growing need to design structures with high stress and strain values, which implies a low number of cycles needed to initiate a crack, Coffin and Manson proposed a model for calculating the number of allowed cycles using the strain ranges as a parameter. In so doing, they created a strain-based model.

Subsequent to that model, other models were proposed for evaluating the number of cycles allowed, using not only strain or stress, but their product instead. These models are known as energy-based models.

The strain-based and the energy-based models are the models recommended for low-cycle fatigue. Since this work focuses on the low-cycle fatigue approach, these models are the ones that will be discussed herein.[3]

3.2

Coffin-Manson or Morrow Model

Some of the literature [4] calls this equation (3.1) the Coffin-Manson equation (or model); others [10], the Morrow model. This is the most common model for low-cycle fatigue evaluation. It relates the range of the strain ($\Delta\varepsilon$) to the number of cycles to failure (N).

[3] Although only the strain and energy-based models are recommended for low-cycle fatigue, all the models can be used for high-cycle fatigue. However, the stress-based models are more frequently used for high cycle fatigue, due their simplicity.

$$\frac{\Delta\varepsilon}{2} = \frac{\Delta\varepsilon_{el}}{2} + \frac{\Delta\varepsilon_{pl}}{2} = \frac{\sigma'_f}{E}(2N)^b + \varepsilon'_f(2N)^c \quad (3.1)$$

where $\Delta\varepsilon_{el}$ is the elastic strain amplitude, $\Delta\varepsilon_{pl}$ is the plastic strain amplitude, σ'_f is the fatigue strength coefficient, ε'_f is the fatigue ductility coefficient, b is the fatigue strength exponent, c is the fatigue ductility exponent, and $2N$ is the total number of reversals to failure. The resulting curve is presented in **Figure 3.1**.

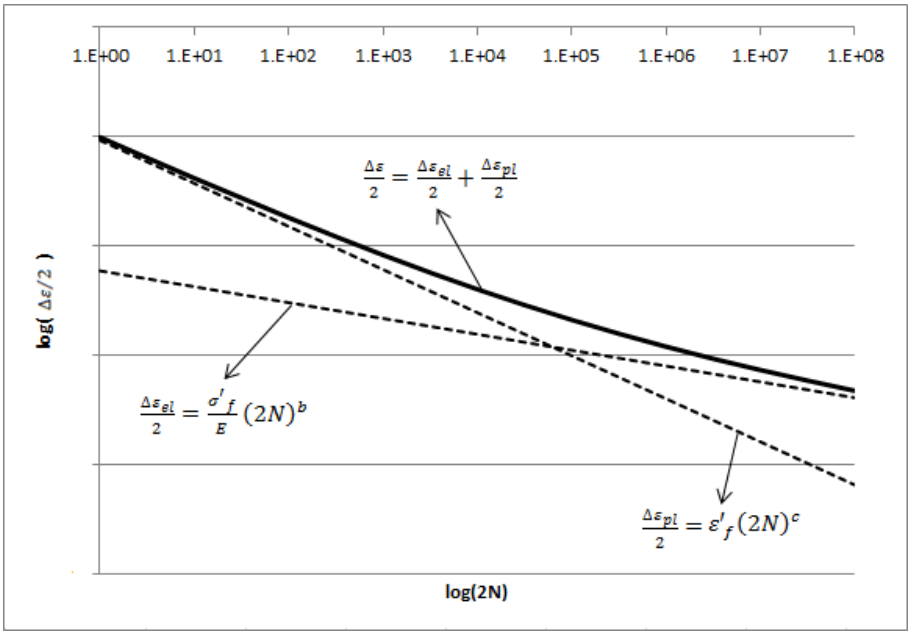

Figure 3.1: Representative curve of equation ($\Delta\varepsilon x N$).

Figure 3.1 helps to show the difference between the denominations and behaviors of so-called low-cycle fatigue and high-cycle fatigue. One can see that, for low numbers of N (low-cycle fatigue); the plastic strain range dominates the curve expressed by the second term of equation (3.1). For high numbers of N (high-cycle fatigue), the curve is dominated by the elastic strain range.

The parameters required in equation (3.1) are obtained by testing the material of interest. The test entails subjecting specimens of the material to strain-controlled tests. For each specimen the same range of strain (**Figure 3.2**) is applied several times until the specimen fails. The strain range and the total number of reversals to failure for each specimen are then plotted on a diagram such as the one in **Figure 3.1**, the resulting curve being the one that best fits the experimental data points.

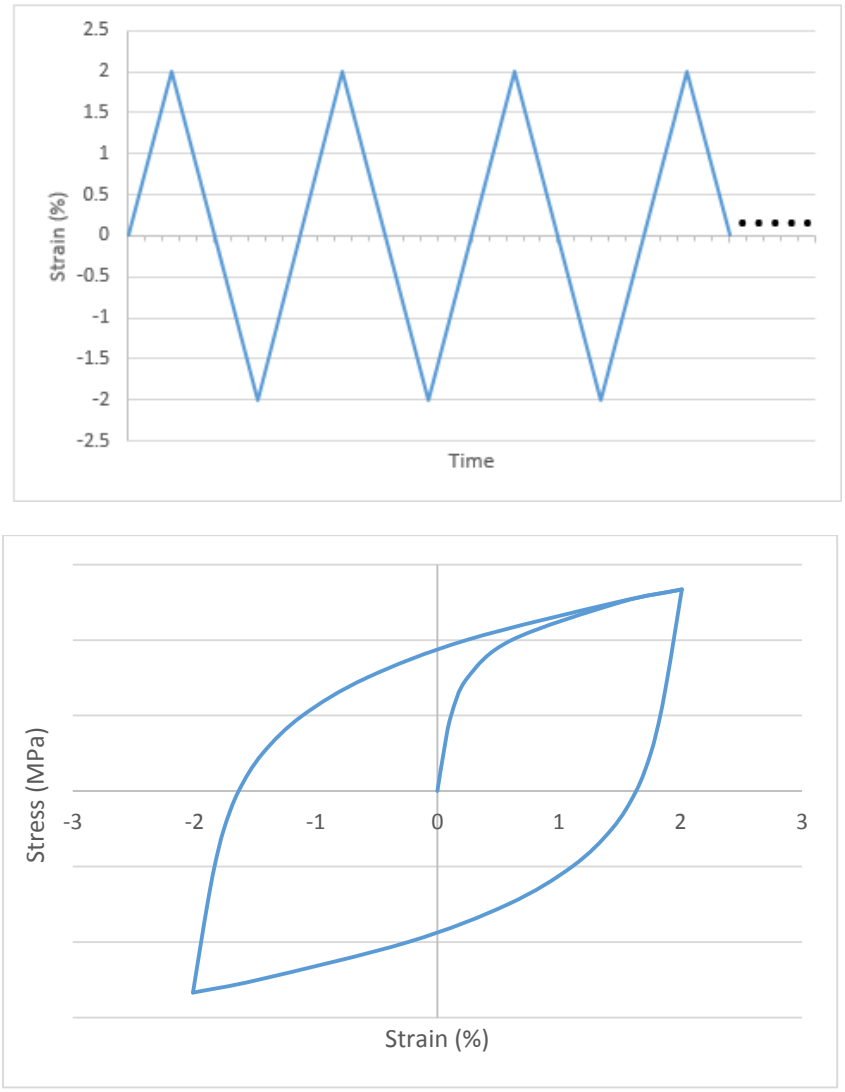

Figure 3.2: (a) Illustration of the strain history in a strain controlled test. (b) Representation of the hysteresis loop of the strain history presented in (a).

For non-proportional histories, this model is frequently used by replacing the left side of equation (3.1) with the equivalent Mises strain range.

3.3
ASME B&PV Code

A fatigue analysis using the ASME Boiler and Pressure Vessel Code [11, 12] is required to use the fatigue curves presented in the code. The fatigue curves in the ASME Code are derived from results of experimental tests. Unnotched and polished test specimens without welds are subjected to strain controlled tests with fully reversed loads at room temperature. The alternated stress (S_a) results x the number of cycles to failure (N) are plotted on a log-log scale chart, where the

alternated stress is the value of $\Delta\varepsilon/2$ – as presented in **Figure 3.1** – multiplied by the elasticity modulus of the steel.

The failure of the specimens is defined as the time that the tensile load drops 25% from its steady test value [13]. The number of cycles to failure is the number of cycles necessary to present this stress drop. The specimens are usually cylindrical and are between 9 and 12 mm in diameter, so this drop in stress represents a crack of approximately 3 mm in depth [13].

The fatigue curves in the ASME Code are the best-fit curves obtained from the experimental results [14]. The curves presented in the code consider margins of 2 on the stress and 20 on the cycles (12 for new curves). These factors are introduced in order to take into consideration effects that change the fatigue strength of components such as size, surface, mean stress, environment, and the fact that fatigue is intrinsically a stochastic phenomenon.

ASME Code Section VIII [12] presents the fatigue curve in two different ways. The first one relates the alternated stress (S_a) to the number of cycles allowed (N) using the following equations:

$$N = 10^X \tag{3.2}$$

$$X = \frac{C_1+C_3Y+C_5Y^2+C_7Y^3+C_9Y^4+C_{11}Y^5}{1+C_2Y+C_4Y^2+C_6Y^3+C_8Y^4+C_{10}Y^5} \tag{3.3}$$

$$Y = \left(\frac{S_a}{C_{us}}\right)\left(\frac{E_{FC}}{E_T}\right) \tag{3.4}$$

where the value of the constants C_n depends on the material and the range of S_a. The value of C_{us} is a conversion factor (equal to 1.0 if S_a is in ksi, and equal to 6.894757 if S_a is in MPa), E_{FC} is the modulus of elasticity used in the evaluation of the fatigue curve and given in the code, and E_T is the modulus of elasticity of the material at the average temperature of the cycle that is being evaluated.

The second way that the fatigue curve is presented in the ASME Code is as a table. There are nine tables (as nine groups of constants C_n) that represent the fatigue curve in the code. Each table is related to one different group of steel. The tables present values of N and the correspondent value of S_a. If a value under consideration is found to be between two values, the code recommends doing an interpolation of the values.

ASME Code, Section III (section for nuclear power plant assessment) presents fatigue curves in the table format. Section VIII presents fatigue curves in both formats.

It is important to note that the fatigue curve presented in the ASME Code gives results similar to those calculated using equation (3.1) of the Coffin-Manson model, if a margin factor of 2 on stress (elastic part) and 20 on life (plastic part) are applied.

The next three paragraphs present a comparison between the fatigue curves presented by the ASME Code and by the Coffin-Manson model. The comparison uses information from the 304 stainless steel presented in [15] and in the ASME Code, Section VIII (the tables presented in this section are the same as those in Section III), in Annex 3-F, group 3.F.3 – the group for 304 stainless steel.

The material properties used for equation (3.1) were: E = 196 GPa, σ'_f = 1287 MPa, ε'_f = 0.122, b = -0.145 and c = -0.394, [15]. For the comparison, equation (3.1) was multiplied by the modulus of elasticity (E), and the factor of 2 on the stress and 20 on the life were included, thus:

$$S_a = E\frac{\Delta\varepsilon}{2} = E\left[\frac{\sigma'_f}{2E}(2N)^b + \varepsilon'_f(20\cdot 2N)^c\right] \quad (3.5)$$

Using the previous equation with the parameters already given, in addition to the table in the ASME Code (presented in **Table 3.1** for 304 stainless steel), a log-log chart $S_a \; x \; N$ was plotted in **Figure 3.3**.

Number of Cycles (N)	Alternated Stress (Sa)
1.00E+01	870
2.00E+01	624
5.00E+01	399
1.00E+02	287
2.00E+02	209
5.00E+02	141
1.00E+03	108
2.00E+03	85.6
5.00E+03	65.3
1.00E+04	53.4
2.00E+04	43.5
5.00E+04	34.1
1.00E+05	28.4
2.00E+05	24.4
5.00E+05	20.5
1.00E+06	18.3
2.00E+06	16.4

5.00E+06	14.8
1.00E+07	14.4
1.00E+08	14.1
1.00E+09	13.9
1.00E+10	13.7
1.00E+11	13.6

Table 3.1: ASME Code data for the 304L stainless steel fatigue curve.

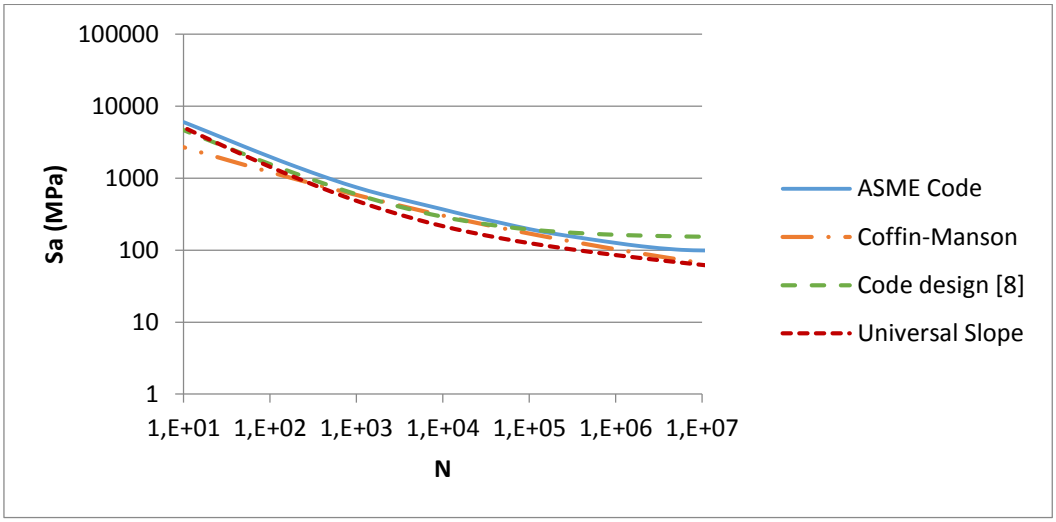

Figure 3.3: ASME Code and Coffin-Manson (with factor) fatigue curves.

One can see in **Figure 3.3** that both curves are similar to each other, with the Coffin-Manson curve being a little more conservative than the ASME code curve. The difference between the two curves can be attributed to different experimental tests.

Figure 3.3 also shows two other fatigue curves. One is given by equation (3.6) and is called the Universal Slope Method, which was proposed by Manson.[4] The material's ultimate strength S_u was taken from reference [15], and the coefficient ε'_b was calculated using RA (area reduction taken from reference [14]) and equation (3.7).

$$S_a = E\frac{\Delta\varepsilon}{2} = E\left[3.5\frac{S_u}{E}(N)^{-0.12} + {\varepsilon'_b}^{0.6}(N)^{-0.6}\right]\frac{1}{2} \tag{3.6}$$

$$\varepsilon'_b = ln\left(\frac{1}{1-\frac{RA}{100}}\right) \tag{3.7}$$

[4] It is important to highlight the fact that none of the models that attempted to establish a relationship between the fatigue parameters and properties of simpler tests (such as tensile, hardness tests) were successful [16]. On that way, using the Coffin-Manson model with the measured fatigue properties it is a better choice than using models such as the Universal Slope Method.

The second curve (equation (3.8)) is given in [14]. The parameters used are valid for 304 stainless steel. This latter equation is the best fit equation for experimental data points used by the ASME curve [14].

$$S_a = \frac{E}{4\sqrt{N}} ln \frac{100}{100-RA} + S_e \tag{3.8}$$

To compare these curves with the one in the ASME Code, the factor of 2 for the stress and 20 for the life must be included; thus, equations (3.6) and (3.8) become, respectively:

$$S_a = E\frac{\Delta\varepsilon}{2} = E\left[3.5\frac{S_u}{2E}(N)^{-0.12} + {\varepsilon'_b}^{0.6}(20N)^{-0.6}\right]\frac{1}{2} \tag{3.9}$$

$$S_a = \frac{E}{4\sqrt{20N}} ln \frac{100}{100-RA} + \frac{S_e}{2} \tag{3.10}$$

To use the fatigue curve of the ASME Code, it is necessary to define the alternated stress in accordance with the code. Section VIII of the code presents two different types of analyses, one based on an elastic analysis and the other based on an elastic-plastic analysis.

3.3.1

Fatigue Assessment Using Elastic Stress Analysis

This method requires the calculation of two types of stress: S_n, which is calculated from the linearization of the stresses and is equal to the primary plus secondary stresses, and S_p, which is calculated using the primary plus secondary plus peak stresses. The method is applied to each range of stress. The stress ranges are calculated using the stresses that occur at the beginning and at the end of each stress cycle. The cycle counting methods are described in the next chapter; nevertheless, it is important to point out the fact that the ASME Code uses only the Extreme Value Method and the Simplified Rainflow methods, the first being applicable to proportional and non-proportional load histories, and the latter to proportional histories.

For each stress cycle, the ASME Code[5] gives two load points in the time history for ${}^{m}t$ and ${}^{n}t$. Using these points, it is possible to calculate the stress ranges ΔS_p for the time-cycle being considered:

[5] This definition is for Section VIII of the ASME Code. In Section III, the S_n and S_p equivalent stress ranges are defined using Tresca instead of von Mises.

$$\Delta S_p = \frac{1}{\sqrt{2}}\left[\left(\Delta\sigma_{xx} - \Delta\sigma_{yy}\right)^2 + \left(\Delta\sigma_{xx} - \Delta\sigma_{zz}\right)^2 + \left(\Delta\sigma_{yy} - \Delta\sigma_{zz}\right)^2 + 6\left(\Delta{\tau_{xy}}^2 + \Delta{\tau_{xz}}^2 + \Delta{\tau_{yz}}^2\right)\right]^{0.5} \quad (3.11)$$

where:

$$\Delta\sigma_{ij} = \left|{}^{m}\sigma_{ij} - {}^{n}\sigma_{ij}\right| \quad (3.12)$$

The alternated stress is then defined as:

$$S_a = \frac{K_f \cdot K_e \cdot \Delta S_p}{2} \quad (3.13)$$

where K_f is the fatigue strength reduction factor, and K_e is the fatigue penalty factor. The value of the fatigue strength reduction factor is one if the calculated stresses already take the effects of a local notch or weld into consideration. If this is not the case, the value of K_f must be calculated.

The value of K_e depends on the S_n stress range. The S_n stress range is calculated similar to the way the S_p stress is calculated - using equation (3.6). The difference is that the stress range S_n considers only the linearized summation of the primary plus the secondary stresses. The value of K_e is then obtained by using the following equation:

$$\begin{cases} K_e = 1 & for \quad \Delta S_n \le S_{PS} \\ K_e = 1 + \frac{(1-n)}{n(m-1)}\left(\frac{\Delta S_n}{S_{PS}} - 1\right) & for\ S_{PS} < \Delta S_n < mS_{PS} \\ K_e = \frac{1}{n} & for \quad \Delta S_n \ge mS_{PS} \end{cases} \quad (3.14)^6$$

where the values of m and n are material properties and the value of S_{PS} is the maximum value between three times the average value of the allowable stress at the highest and lowest temperature occurring in the cycle, and two times the average value of the yield stress at the highest and lowest temperature occurring in the cycle, as given by the equations described in **Figure 3.4**. The values of m and n are given in Table 5.13 of the code for different materials, and their values vary from 1.7 to 3 for m and from 0.2 to 0.3 for n.

[6] This equation is defined in Section VIII of the ASME Code. In Section III, the S_{PS} value is replaced with the S_m property given in the code.

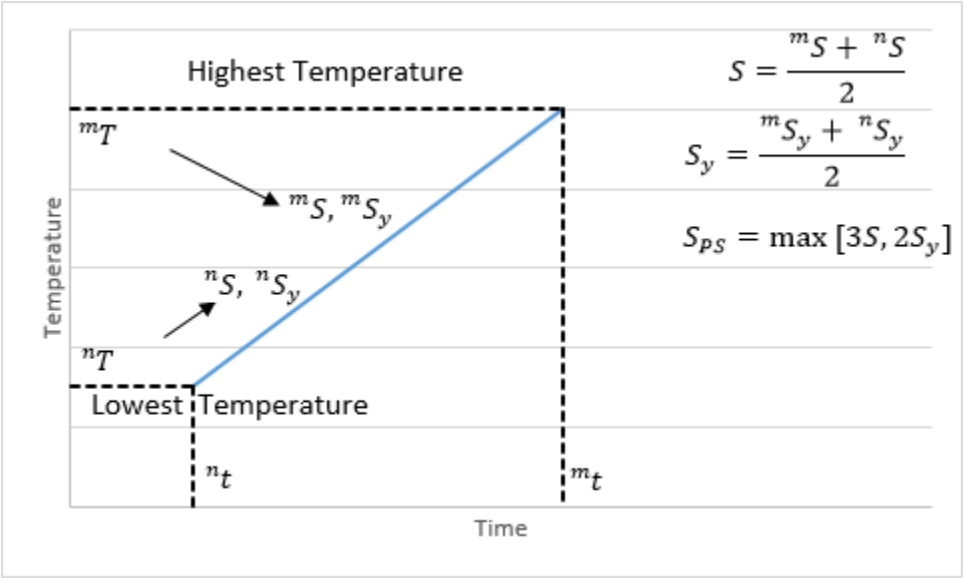

Figure 3.4: Exemplification of the calculation of S_{PS}.

The advantage of this method is that, by including the fatigue penalty factor, it is possible to perform a fatigue evaluation of a component under cyclic plasticity employing an elastic stress analysis. One can see in equation (3.9) that the value of K_e varies between 1.0 and 3.3 or 5.0 (depending on the value of n). This constitutes the simplified elasto-plastic fatigue analysis.

If a component is subjected to a minor cyclic loading (causing an irrelevant plastic deformation), the value of K_e is 1.0, and the value of the alternating stress is not changed by the penalty factor. However, if the cyclic load is large enough to make the plastic deformation relevant, the value of K_e increases, as does the value of the alternating stress. This is how this method includes the effect of cyclic plasticity in the framework of an elastic stress analysis.

Even though this procedure (of doing a large-strain low-cycle fatigue evaluation with the results from an elastic stress analysis) is an excellent idea, it has already been shown [14] that the results of this procedure can lead to over conservative results. The code also includes a different method for evaluating the value of the penalty factor, but it is first necessary to do an elastic-plastic analysis, which would negate the largest advantage of this method. New methods for evaluating K_e are being studied to fix this problem, but the best way to not deal with over conservative results is by using an accurate elasto-plastic analysis.

3.3.2

Fatigue Assessment Using Elasto-Plastic Stress Analysis

This method requires performing a full elasto-plastic stress analysis instead of an elastic stress analysis. This method also requires some sort of cycle counting.[7] Using the results of the cycle counting, the effective strain range is evaluated accordingly by applying equation (3.15).

$$\Delta\varepsilon_{eff} = \frac{\Delta S_p}{E_{ya}} + \Delta\varepsilon_{peq} \tag{3.15}$$

where ΔS_p is as defined in equation (3.6), E_{ya} is the average value of the elasticity modulus at the highest and lowest temperature of the cycle, and $\Delta\varepsilon_{peq}$ is the same plastic strain range defined in equation (3.16), which is analogous to equation (3.6):

$$\Delta\varepsilon_{peq} = \frac{\sqrt{2}}{3}\left[\left(\Delta p_{xx} - \Delta p_{yy}\right)^2 + \left(\Delta p_{xx} - \Delta p_{zz}\right)^2 + \left(\Delta p_{yy} - \Delta p_{zz}\right)^2 + 1.5\left(\Delta {p_{xy}}^2 + \Delta {p_{xz}}^2 + \Delta {p_{yz}}^2\right)\right]^{0.5} \tag{3.16}$$

where Δp_{ij} is the plastic strain range of the ij component. The value of the alternated stress is then calculated with:

$$S_a = \frac{E_{ya} \cdot \Delta\varepsilon_{eff}}{2} \tag{3.17}$$

Using the value of the alternated stress, it is possible to get the allowed number of cycles.

What all the damage models presented so far have in common is that they use some type of equivalent strain or stress range; for example, one based on the von Mises parameter for evaluating fatigue life. However, it is well-known that, for the fatigue assessment of non-proportional histories, the models that have the best behavior are usually the critical plane models.

3.4

Critical Plane Models

Critical plane models investigate the stresses and strains that occur on each possible plane that passes through the material point, and they evaluate the

[7] The cycle counting performed here counts the stresses and relates the plastic strain ranges in the same way as explained in equation (3.7). In cases were the strains are already measured, the cycle counting can be performed on the strains, and the $\Delta\varepsilon_{eff}$ value can be calculated by the von Mises equivalent strain equation using the total strain values instead of separating them into plastic and elastic parts as in equation (3.10).

fatigue damage on each one of those planes. The plane that presents most damage will be the critical one. It is assumed that the fatigue crack propagates on that plane.

The first step is to calculate the stresses and strains that are acting on the plane that is to be investigated. For a given plane, as presented in **Figure 3.5**, the stresses acting on the plane can be obtained with equations (3.18), (3.19) and (3.20). For strains, equations (3.21), (3.22) and (3.23) should be used.

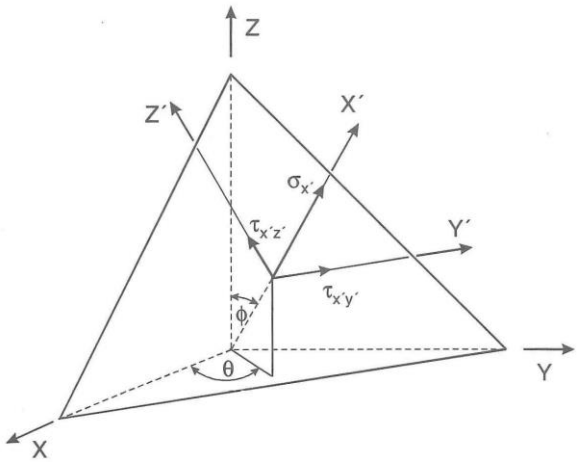

Figure 3.5: Illustration of the stresses acting on a particular plane. [10]

$$\sigma_{x\prime} = sin^2(\phi) \cdot \left[\sigma_y sin^2(\theta) + \sigma_x cos^2(\theta)\right] + \sigma_z cos^2(\phi) + 2\tau_{xy} sin^2(\phi) \cdot \sin(\theta) \cdot \cos(\theta) + 2\sin(\phi) \cdot \cos(\phi) \cdot \left[\tau_{xz}\cos(\theta) + \tau_{yz}\sin(\theta)\right] \quad (3.18)$$

$$\tau_{x\prime y\prime} = \sin(\phi) \cdot \cos(\theta) \cdot \sin(\theta) \cdot \left(\sigma_y - \sigma_x\right) + \tau_{xy}\sin(\phi) \cdot [cos^2(\theta) - sin^2(\theta)] + \cos(\phi) \cdot \left[\tau_{yz}\cos(\theta) - \tau_{xz}\sin(\theta)\right] \quad (3.19)$$

$$\tau_{x\prime z\prime} = \sin(\phi) \cdot \cos(\phi) \cdot \left[\sigma_z - \sigma_x cos^2(\theta) - \sigma_y sin^2(\theta)\right] - 2\tau_{xy}\sin(\phi) \cdot \cos(\phi) \cdot \sin(\theta) \cdot \cos(\theta) + sin^2(\phi) \cdot \left[\tau_{xz}\cos(\theta) + \tau_{yz}\sin(\theta)\right] - cos^2(\phi) \cdot \left[\tau_{xz}\cos(\theta) + \tau_{yz}\sin(\theta)\right] \quad (3.20)$$

$$\varepsilon_{x\prime} = sin^2(\phi) \cdot \left[\varepsilon_y sin^2(\theta) + \varepsilon_x cos^2(\theta)\right] + \varepsilon_z cos^2(\phi) + \gamma_{xy} sin^2(\phi) \cdot \sin(\theta) \cdot \cos(\theta) + \sin(\phi) \cdot \cos(\phi) \cdot \left[\gamma_{xz}\cos(\theta) + \gamma_{yz}\sin(\theta)\right] \quad (3.21)$$

$$\gamma_{x'y'} = 2 \cdot \{\sin(\phi) \cdot \cos(\theta) \cdot \sin(\theta) \cdot (\varepsilon_y - \varepsilon_x) + (\gamma_{xy}/2) \cdot \sin(\phi) \cdot [cos^2(\theta) - sin^2(\theta)] + \cos(\phi) \cdot [(\gamma_{yz}/2) \cdot \cos(\theta) - (\gamma_{xz}/2) \cdot \sin(\theta)]\} \quad (3.22)$$

$$\gamma_{x'z'} = 2 \cdot \{\sin(\phi) \cdot \cos(\phi) \cdot [\varepsilon_z - \varepsilon_x cos^2(\theta) - \varepsilon_y sin^2(\theta)] - \gamma_{xy} \sin(\phi) \cdot \cos(\phi) \cdot \sin(\theta) \cdot \cos(\theta) + sin^2(\phi) \cdot [(\gamma_{xz}/2) \cdot \cos(\theta) + (\gamma_{yz}/2) \cdot \sin(\theta)] - cos^2(\phi) \cdot [(\gamma_{xz}/2) \cdot \cos(\theta) + (\gamma_{yz}/2)\sin(\theta)]\} \quad (3.23)$$

Critical plane models are usually based on the same concept. This concept entails predicting the initiation and growth of a short crack (undetectable with normal industrial procedures). The existing models predict that the crack will start and propagate in either Mode I or Mode II [10]. It is known that cracks can also propagate in Mode III, but the models considered in this thesis do not predict such behavior.

It bears pointing out that the Mode I, Mode II and Mode III nomenclatures are used in the fracture mechanics field. However, it is also used herein to subcategorize models that evaluate fatigue in materials more sensitive to normal stress (Mode I) and materials more sensitive to shear stress (Mode II or Mode III).

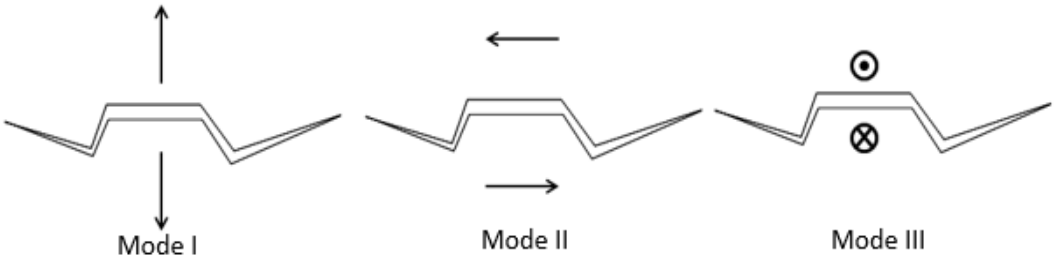

Figure 3.6: Illustration of cracks under Mode I, Mode II and Mode III conditions.

A few these models will be presented and discussed.

3.5
Brown-Miller Model

After having observed multiaxial low-cycle fatigue tests, Brown and Miller [17] concluded that the equivalent strain was not a good parameter for evaluating the fatigue life of low-cycle fatigue problems. Hence, they decided to conduct axial and torsion tests, keeping the shear strain range constant to better understand the problem. They concluded that two strain parameters were needed to predict the

life of a multiaxial low-cycle fatigue condition. They also concluded that these two parameters had to involve the normal and shear strain ranges.

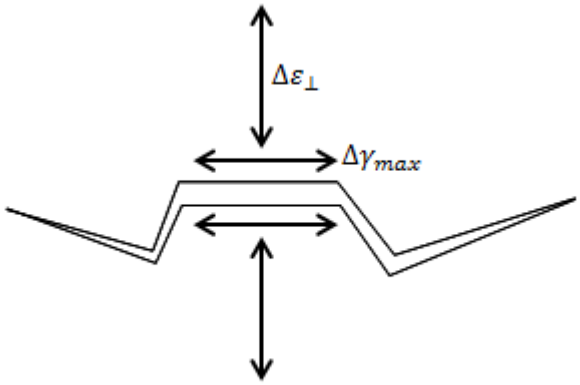

Figure 3.7: Illustration of the strain range parameters of the Brown-Miller model.

Brown and Miller proposed calculating the equivalent shear strain range by using the shear and normal strain ranges acting on the plane with maximum shear strain with the following equation:

$$\frac{\Delta\hat{\gamma}}{2} = \frac{\Delta\gamma_{max}}{2} + S\Delta\varepsilon_{\perp} \tag{3.24}$$

where $\Delta\hat{\gamma}$ is the equivalent shear strain range, $\Delta\gamma_{max}$ is the maximum shear strain range, S is a material property, and $\Delta\varepsilon_{\perp}$ is the normal strain range acting on the plane where the $\Delta\gamma_{max}$ is found.

Considering a uniaxial stress state, the ranges of maximum shear and normal strains can be calculated as:

$$\frac{\Delta\gamma_{max}}{2} = (1+v)\frac{\Delta\varepsilon}{2};\ \ \Delta\varepsilon_{\perp} = (1-v)\frac{\Delta\varepsilon}{2} \tag{3.25}$$

Substituting equation (3.25) in equation (3.24):

$$\frac{\Delta\hat{\gamma}}{2} = \frac{\Delta\varepsilon}{2}[(1+v) + S(1-v)] \tag{3.26}$$

Separating the right side of equation (3.26) into plastic and elastic parts yields:

$$\frac{\Delta\hat{\gamma}}{2} = \frac{\Delta\varepsilon_{el}}{2}[(1+v_{el}) + S(1-v_{el})] + \frac{\Delta\varepsilon_{pl}}{2}\left[\left(1+v_{pl}\right) + S(1-v_{pl})\right] \tag{3.27}$$

This equation can be simplified as:

$$\frac{\Delta\hat{\gamma}}{2} = A\frac{\Delta\varepsilon_{el}}{2} + B\frac{\Delta\varepsilon_{pl}}{2} \tag{3.28}$$

Where $A = (1 + v_{el}) + S(1 - v_{el})$ and $B = \left(1 + v_{pl}\right) + S(1 - v_{pl})$. If one considers that v_{pl} = 0.5 and that v_{el} = 0.3 for most types of steels, the A and B values are: $A = 1.3 + 0.7S$ and $B = 1.5 + 0.5S$. Substituting equation (3.24) in equation (3.1) and equation (3.20) yields:

$$\frac{\Delta\gamma_{max}}{2} + S\Delta\varepsilon_{\perp} = A\frac{\sigma'_f}{E}(2N)^b + B\varepsilon'_f(2N)^c \quad (3.29)$$

This is the equation of the Brown-Miller Model. This model is a critical plane model, so all possible planes must be investigated so that the plane with the least number of cycles required to initiate a crack may be found. Parameter S is one of the problems of this solution, this parameter not only depends on the material, but also on temperature and the value of N.

As shown in [4], when N is close to the fatigue limit of the material, the value of S is close to 0.3. However [10] shows this property obtained for short lives (close to one thousand cycles), where the results for S can vary widely. In 304 stainless steel at 20°C, the value of S is 1.57, while at 550°C, S is 1.0, and in 316 stainless steel at 550°C, the value of S is 2.4.

The need to determine S for different ranges of numbers of cycles and different ranges of temperatures is seen as a considerable disadvantage of the Brown-Miller Model.

3.6
Fatemi-Socie Model

The Brown-Miller Model has another disadvantage. It is possible to show that using only the shear and normal strain ranges cannot correctly predict the allowed number of cycles. For example, consider two specimens of the same material, both being subjected to the same shear and normal strain ranges, but the first with a negative mean normal stress and the second one with a positive mean normal stress. The first one will resist more cycles than the second one.

This happens because, whereas in the first case a micro crack in the specimen closes due to the negative mean normal stress, in the second case, the micro crack opens due to the positive mean normal stress, and with this opening, the micro crack will grow until it becomes detectable. This problem was the one studied by Socie and Shield [18].

Socie and Shield tested several Inconel specimens with different biaxial loading histories. They designed the histories so that all of them would have similar maximum shear and normal strain amplitudes in common, similar equivalent axial and shear stress, and similar plastic work. The only relevant difference was the normal stress. The results that should have been the same according to the Brown-Miller model were actually much different. Hence, Fatemi and Socie proposed [19] the following equation:

$$\frac{\Delta\gamma}{2}\left(1 + k\frac{\sigma_{\perp max}}{S_y}\right) = \frac{\tau'_f}{G}(2N)^{b_\gamma} + \gamma'_f(2N)^{c_\gamma} \tag{3.30}$$

where Δγ is the range of shear strain on the plane being evaluated, $\sigma_{\perp max}$ is the maximum stress normal to the plane that is being evaluated, k is a material constant, S_y is the yield strength, τ'_f is the shear fatigue strength coefficient, γ'_f is the shear fatigue ductility coefficient, b_γ is the shear fatigue strength exponent, c_γ is the shear fatigue ductility exponent, and G is the shear elastic model.

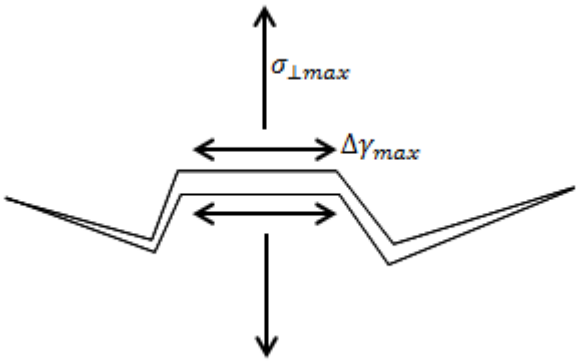

Figure 3.8: Illustration of the parameters required in the Fatemi-Socie model.

The parameters on the right side of equation (3.30) can be approximated by the parameters on the right side of equation (3.1) using the following relationships: $\tau'_f \approx \sigma'_f/\sqrt{3}$, $\gamma'_f \approx \sqrt{3}\varepsilon'_f$, $b_\gamma \approx b$, $c_\gamma \approx c$ and $G = E/2(1+v)$.

The material constant k can be calculated by comparing uniaxial test results with pure torsion test results. Reference [15] shows that the values of k are 0.15 for 304L stainless steel and 0.7 for 1050 steel. Reference [10] recommends using k = 1 if no tests results are available.

3.7
Smith-Watson-Topper Model

The critical plane models presented above were developed for materials where a crack initiates and initially grows in Mode II due to shear strain. The Smith-Watson-Topper Model is the alternative solution for evaluating fatigue damage in materials where the initiation and growth of short cracks is controlled by the Mode I condition. Cast iron and 304 stainless steel are examples of such materials.

This model was first developed as a way to also take into consideration the means stress value in uniaxial fatigue test results. Mean stress is an important parameter, as described above in the explanation of the Fatemi-Socie model.

It has been seen [17] that strain ranges alone, as in the Coffin-Manson model, for example, may not do a good job of predicting the life of a specimen. The strain range by itself cannot provide information if the short crack is opening under tension or closing under compression. Consequently, Smith [20] proposed a new model that is referred to in the literature as the SWT (Smith-Watson-Topper) model.

The SWT (Smith-Watson-Topper) model is controlled by the principal strain range $\Delta\varepsilon_1$ and by the maximum stress that actuates in the same direction as the principal strain range σ_{max1}. The rest of the parameters in equation (3.31) are the same as the ones described in equation (3.1).

$$\sigma_{max1}\frac{\Delta\varepsilon_1}{2} = \frac{{\sigma'_f}^2}{E}(2N)^b + \sigma'_f\varepsilon'_f(2N)^c \tag{3.31}$$

Although this model was initially created to evaluate fatigue in uniaxial tests, it has been modified over the years [4, 10] so that it can also be used for multiaxial conditions under proportional and non-proportional loadings. For non-proportional loadings, the equation is changed to a critical plane model:

$$\sigma_{max\perp}\frac{\Delta\varepsilon_\perp}{2} = \frac{{\sigma'_f}^2}{E}(2N)^b + \sigma'_f\varepsilon'_f(2N)^c \tag{3.32}$$

Since this model is a critical plane model, all possible planes must be investigated so that the plane with the least number of cycles for initiating a crack may be found. The parameters shown in equation (3.32) are the strain range perpendicular to a candidate critical plane under investigation ($\Delta\varepsilon_\perp$) and the maximum stress that acts in the same direction as the perpendicular strain range ($\sigma_{max\perp}$).

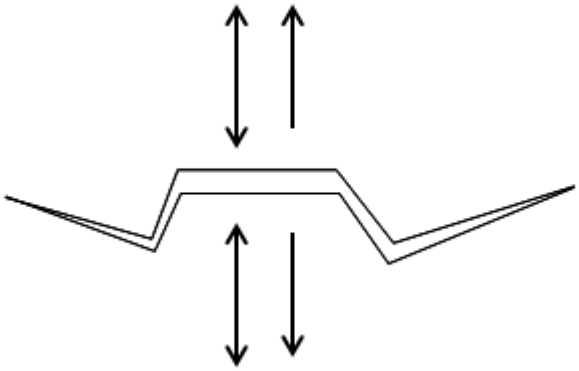

Figure 3.9: Illustration of the parameters required in the SWT model.

3.8
Gupta-Fesich Model

Gupta and Fesich [21] proposed a critical plane model for evaluating the fatigue damage from stress states subjected to fixed and rotating principal stress or strain directions. Loadings with fixed principal stress directions are considered proportional when the direction never changes. Cases where only the value of the principal strain (or stress) changes, and cases entailing a rotating principal direction are considered as a non-proportional history, where not only the value of the principal strain (or stress) changes, but the principal direction changes as well.

The model, developed at BARC and MPA University of Stuttgart, was created based on the experimental results obtained for specimens subjected to torsional loadings. The model's equation is similar to the one presented by the SWT model. The main modification is the inclusion of the shear strain range $\Delta\gamma$ and the shear stress range $\Delta\tau$.

$$\sigma_{\perp max}\frac{\Delta\varepsilon_{\perp}}{2}+\frac{\Delta\gamma}{2}\frac{\Delta\tau}{2}=\frac{{\sigma'_f}^2}{E}(2N)^b+\sigma'_f\varepsilon'_f(2N)^c \qquad (3.33)^8$$

This model is a critical plane model, so all possible planes must be investigated so that the plane with the least number of cycles required to initiate a crack may be found. The shear strain and stress values can be calculated as the ones acting on the plane perpendicular to the normal strain and stress.

[8] It is important to note that the models mixture damages. The right side of equation (3.33) presents only parameters regarding normal loads, while the left side of the equation mixture normal and shear parameters without any adjustment coefficient. Moreover, the equation mixes an energy criteria $(\Delta\gamma/2\cdot\Delta\tau/2)$ with other criteria that are not energy $(\sigma_{\perp max}\cdot\Delta\varepsilon_{\perp}/2)$. For that reason, Liu I and Liu II [10] are better recommended for evaluating damage while keeping a similar approach.

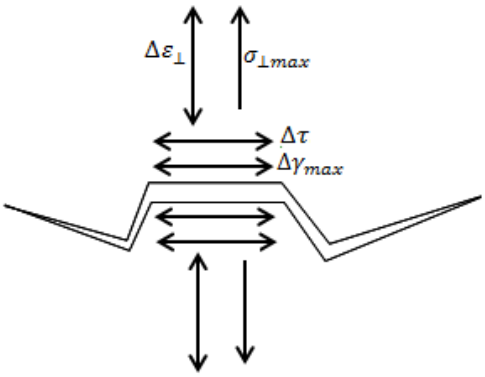

Figure 3.10: Illustration of the parameters required in the Gupta-Fesich model.

Fesich later proposed a modification not only on his method, but on the Fatemi-Socie model also. The improvement he proposed for those models was the addition of the strain gradient effect as a support effect. With that addition, equations (3.30) and (3.33) become, respectively:

$$\left(\frac{1}{1+\chi_\gamma}\right)\frac{\Delta\gamma}{2}\left(1+k\frac{1}{1+\chi_\varepsilon}\frac{\sigma_{\perp max}}{\sigma_y}\right)=\frac{\tau'_f}{G}(2N)^{b_\gamma}+\gamma'_f(2N)^{c_\gamma} \tag{3.34}$$

$$\left(\frac{1}{1+\chi_\varepsilon}\right)\sigma_{\perp max}\frac{\Delta\varepsilon_{\perp}}{2}+\left(\frac{1}{1+\chi_\gamma}\right)\frac{\Delta\gamma}{2}\frac{\Delta\tau}{2}=\frac{{\sigma'_f}^2}{E}(2N)^b+\sigma'_f\varepsilon'_f(2N)^c \tag{3.35}$$

where χ_ε is the normal strain gradient and χ_γ is the shear strain gradient, as defined by Sibel in [22]:

$$\chi_\varepsilon=\frac{1}{\varepsilon_{max}}\left(\frac{d\varepsilon}{dy}\right)_{max};\chi_\gamma=\frac{1}{\gamma_{max}}\left(\frac{d\gamma}{dy}\right)_{max} \tag{3.36}$$

Figure 3.11 illustrates the strain gradient parameters required for equation (3.36)**.**

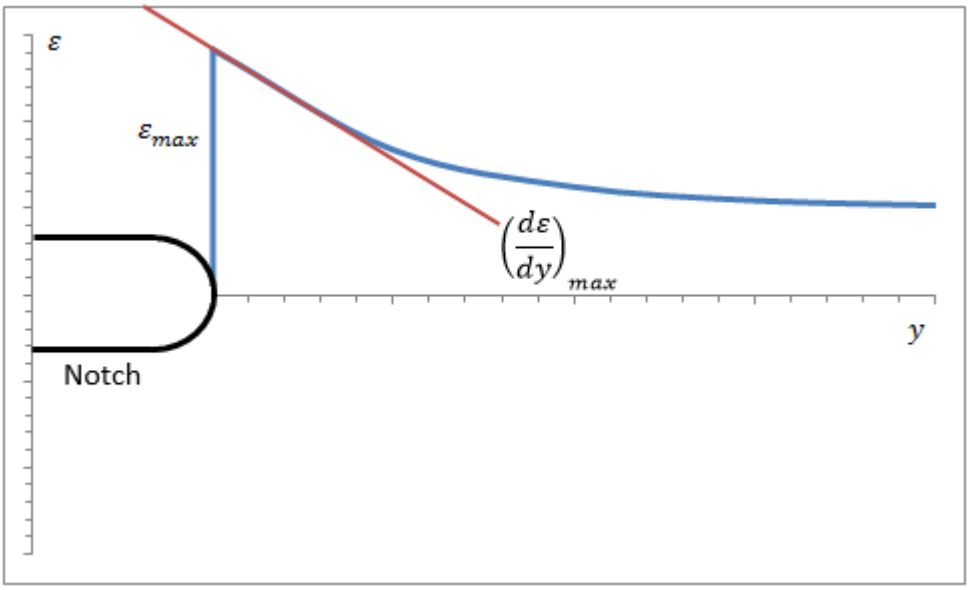

Figure 3.11: Illustration of the parameters required to evaluate the normal strain gradient.

A notched component will produce not only a strain (ε_{max}) and stress concentration, but also a strain ($\varepsilon(y)$) and stress distribution in the region close to the notch. This distribution (the blue line in **Figure 3.11**) reaches maximum value at the notch and stabilizes at minimum value in an area far from the notch (the exact distance depends on the shape and size of the notch).

The parameters needed in equation (3.36) can be evaluated as the maximum strain value and the maximum differentiation value of the strain distribution in relation to the distance (y). This was the modification proposed by Fesich for improving the evaluation of fatigue damage in notched components [13].

4

Cycle Counting

4.1

Cycle Counting Methods

There are several cycle counting methods available in the current literature. This chapter presents and discusses 7 of these methods that can be applied to non-proportional histories: the Extreme Value Method (EVM) [12, 23], the Rainflow Method [24, 4], the Simplified Rainflow Method [12], the Bannantine and Socie Method [25, 15], the Wang-Brown Method [27, 28], the Modified Wang-Brown Method [28] and the Path Dependent Maximum Range Method [30].

Cycle counting methods can be applied to count stress or strain histories, but conducting the cycle counting using the strain history in the low cycle fatigue cases is highly recommended to avoid non-conservative life evaluations.

However, in cases where strains are not measured and significant changes in temperature are observed, evaluating the stress-strain relationship becomes rather complex. To overcome this difficulty, industrial design codes, such as the ASME Code, enable the user to perform cycle counting using the calculated stress results.

Differences between the stress and strain based counting approaches will be evaluated and discussed in Chapter 6, where the fatigue life results obtained using different cycle counting routines based on stress and strain will be compared.

4.2

Extreme Value Method

The Extreme Value Method (EVM) is a simple, conservative cycle counting method. Its uniaxial form consists of selecting two points in the stress or strain load history, one with the highest value and the other with the lowest value. A range is determined with this pair of values and after it has been counted, the points are deleted from the load history. The procedure then continues until no more reversal points are found.

The idea behind this cycle counting method is to determine the highest range possible, then the second one, and so on.

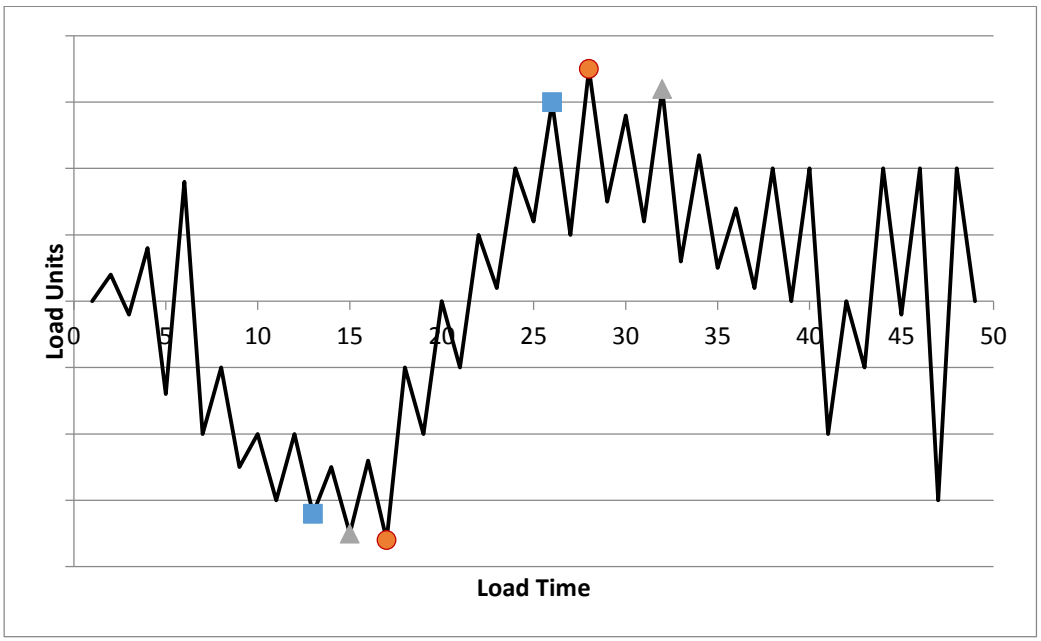

Figure 4.1: Example of the Extreme Value Method.

Figure 4.1 helps to show the sequence followed using the EVM cycle counting method. In this particular load history, the highest range is identified by the two points marked with circles, the second highest range with triangles, and the third highest with squares. The selection of pairs of points in the load history to determine the range continues until no more reversal points are left.

The EVM does not have to be used in the actual load history sequence. The load history can be organized in or out of order of stress or strain occurrences observed along a certain amount of time, as shown in **Figure 4.2**.

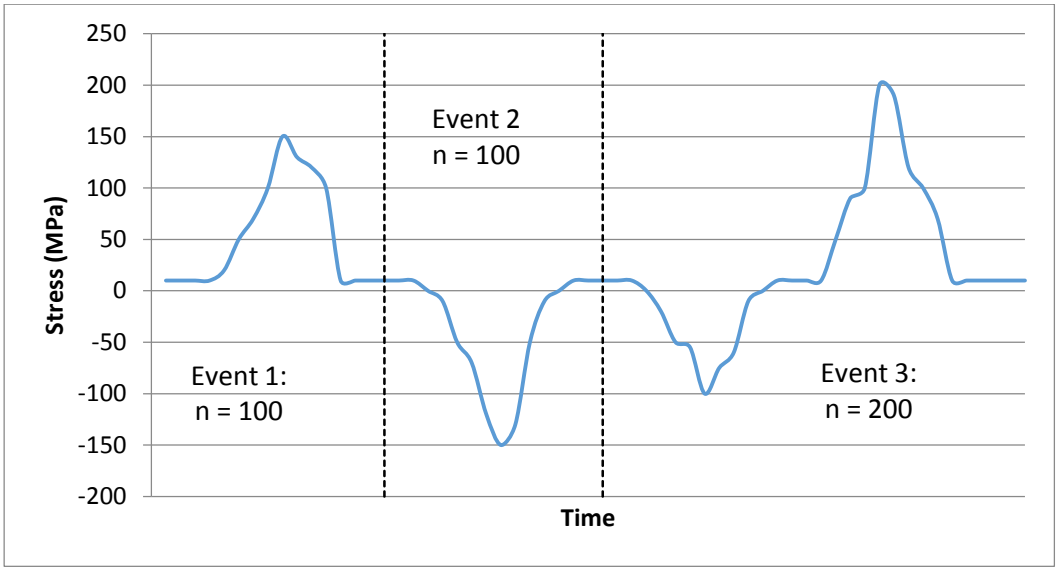

Figure 4.2: Example of representative load history.

Figure 4.2 presents a representative load history where a string of important events occurring during the operation life of an equipment are placed out of order. The events are organized, though not necessarily in order, and each one represents the load conditions (such as start-up, shut-down, normal operation, etc.) applied to the component. The history must be presented with the number of occurrences (expected or measured) of each event. **Figure 4.2** is an example of a representative load history with three events and their number of occurrences (n).

The Extreme Value Method is the method allowed by ASME Code for non-proportional histories. A summary of the steps presented in Annex 5 of the code is:

- Step 1: Calculate the stress history (the analysis must include peak stresses at local discontinuities).
- Step 2: Delete the points that are not reversal points (or peak or valley points).
- Step 3: Find in the history the pair of points (^{m}t, ^{n}t) that produces the highest range of the equivalent von Mises stress, using equation (4.1).

$$^{mn}\Delta S_{range} = \frac{1}{\sqrt{2}}[(^{mn}\Delta\sigma_{11} - {}^{mn}\Delta\sigma_{22})^2 + (^{mn}\Delta\sigma_{22} - {}^{mn}\Delta\sigma_{33})^2 + (^{mn}\Delta\sigma_{33} - {}^{mn}\Delta\sigma_{11})^2 + \\ +6(^{mn}\Delta\sigma_{12}{}^2 + {}^{mn}\Delta\sigma_{23}{}^2 + {}^{mn}\Delta\sigma_{31}{}^2)]^{0.5} \quad (4.1)$$

where:

$$^{mn}\Delta\sigma_{ij} = {}^{m}\sigma_{ij} - {}^{n}\sigma_{ij} \quad (4.2)$$

$$^{m}\sigma_{ij} = \sigma_{ij}(^{m}t) \text{ and } {}^{n}\sigma_{ij} = \sigma_{ij}(^{n}t) \quad (4.3)$$

- Step 4: Record the time points ${}^{m}t$ and ${}^{n}t$ and their specified number of repetitions ${}^{m}N$, ${}^{n}N$.
- Step 5: Determine the number of cycles repetitions:
  - If ${}^{m}N < {}^{n}N$: Delete point ${}^{m}t$, and reduce the number of repetitions at point ${}^{n}t$ to ${}^{n}N - {}^{m}N$.
  - If ${}^{m}N > {}^{n}N$: Delete point ${}^{n}t$, and reduce the number of repetitions at point ${}^{m}t$ to ${}^{m}N - {}^{n}N$.
  - If ${}^{m}N = {}^{n}N$: Delete both points ${}^{n}t$ and ${}^{m}t$.
- Step 6: Return to Step 3 and repeat Steps 3 to 6 until no more reversal points remains in the history.

For a better visualization of the procedure, the method is applied in the load history presented in **Figure 4.2**. Step 1 entails determining the stress history shown in **Figure 4.2**. The result of step 2 (elimination of the points that are not reversals) can be seen in **Figure 4.3**.

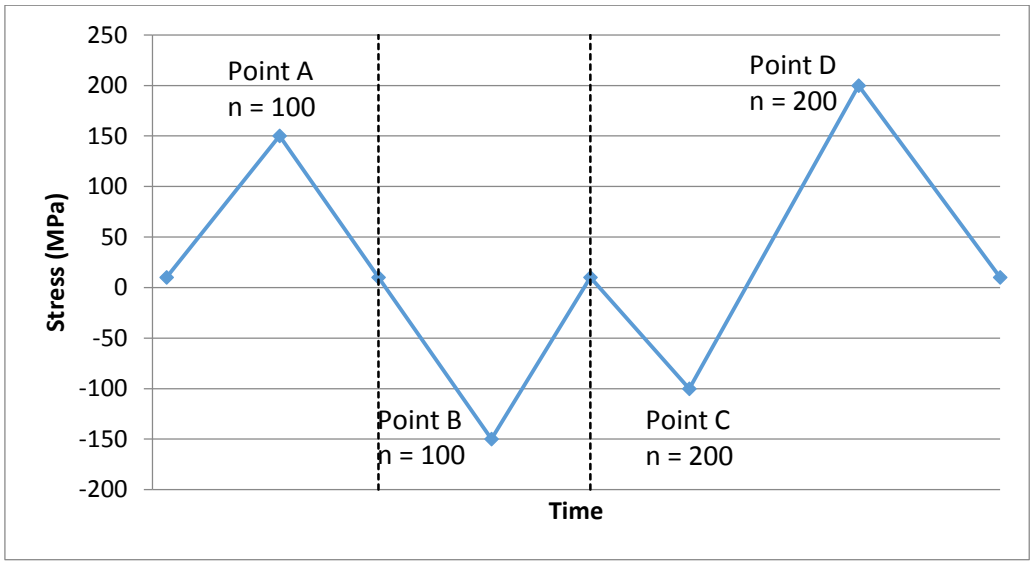

Figure 4.3: Example of the elimination of non-reversal points in the load history presented in **Figure 4.2**.

Step 3 selects the possible pairs that can be formed. The pair with the widest range is pair D-B. Since the number of occurrences at point B is less than the number of occurrences at point D, point B is deleted, the number of occurrences at point D is reduced to 100, and a range of 350 MPa with 100 repetitions is counted.

The procedure returns to step 3, and now the pair with the widest range is pair C-D. The same routine described above is applied, the range of 300 MPa with 100 repetitions is counted, and the history now contains only points A and C, both with 100 occurrences. Lastly, the final counting will return the range of pair A-C. Since both have the same number of occurrences, they are deleted and the cycle counting ends, because there are no more reversal points remaining in the history.

The Extreme Value Method can also be used to count cycles for a strain history. The procedure is the same described previously, the difference being the use of the equivalent von Mises strain in equation (4.4):

$$ {}^{mn}\Delta e_{range} = \frac{1}{\sqrt{2}(1+\bar{v})}[({}^{mn}\Delta\varepsilon_{11} - {}^{mn}\Delta\varepsilon_{22})^2 + ({}^{mn}\Delta\varepsilon_{22} - {}^{mn}\Delta\varepsilon_{33})^2 + ({}^{mn}\Delta\varepsilon_{33} - {}^{mn}\Delta\varepsilon_{11})^2 + $$
$$ +1.5\left({}^{mn}\Delta\varepsilon_{12}{}^2 + {}^{mn}\Delta\varepsilon_{23}{}^2 + {}^{mn}\Delta\varepsilon_{31}{}^2\right)]^{0.5} \quad (4.4) $$

where:

$$ {}^{mn}\Delta\varepsilon_{ij} = {}^{m}\varepsilon_{ij} - {}^{n}\varepsilon_{ij} \quad (4.5) $$

$$ {}^{m}\varepsilon_{ij} = \varepsilon_{ij}({}^{m}t) \text{ and } {}^{n}\varepsilon_{ij} = \varepsilon_{ij}({}^{n}t) \quad (4.6) $$

and $\bar{v}$ is the mean or effective Poisson coefficient, which is defined in equation (4.7):

$$ \bar{v} = \left(0.5\varepsilon_{pl} + v_{el}\varepsilon_{el}\right)/(\varepsilon_{pl} + \varepsilon_{el}) \quad (4.7) $$

where ε_{pl} and ε_{el} are, respectively, the plastic and elastic components of the strains.

As already mentioned, the EVM enables the user to evaluate the load history apart from its actual sequence. This characteristic makes it advantageous for use in the design phase of a component, where the expected loading sequence of events is unknown.

4.3
Rainflow

This method, proposed by the Japanese researchers Matsuishu and Endo toward the end of the 1960's [24], is the best way of cycle counting an entire complex history of uniaxial loads [4]. The name comes from the original description of the technique, where the process is described in terms of rain falling off a "pagoda roof". This method can be used either with stress or strain histories.

The step sequence is:

- Step 1: Eliminate all values that are not reversal points (peaks and valleys).
- Step 2: Start the counting at the first event in the history.
- Step 3: From the point under consideration, the cycle counting continues sequentially until:
    - Flow from a higher or equal peak (or a smaller or equal valley) than the initial point is met.
    - The flow counting from a previously initiated flow is met.
    - The load history is finished.
- Step 4: Count a half cycle using the values at the beginning and at the end of the cycle counting result, go to the next point in the history and repeat steps 3 and 4 until the load history is finished.

Figure 4.4 helps to show cycle counting using the Rainflow Method (RM) by way of an example.

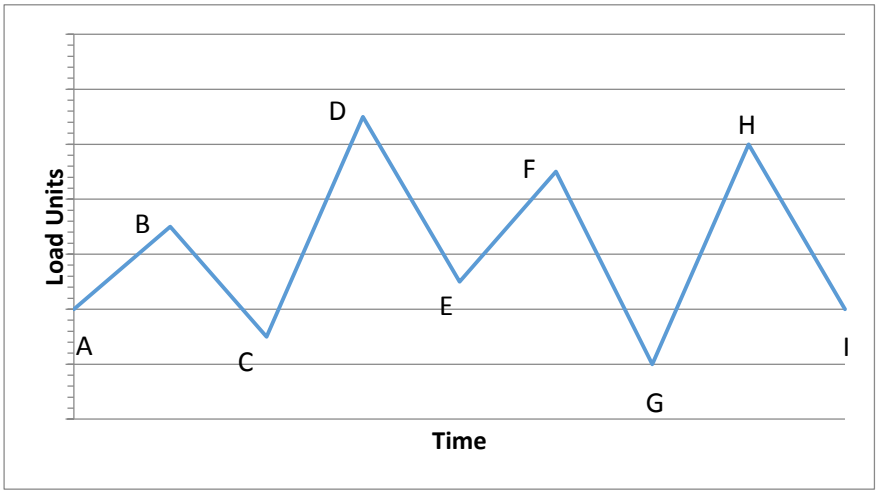

Figure 4.4: Load history.

The load history does not require step 1, since it only has reversal points. **Figure 4.5** shows the exemplification of the cycle counting. The counting starts at the beginning of the history, point A, which is a valley, and finishes at point C, which is a smaller valley compared to A. The counting continues sequentially, this time starting at point B and finishing at point D, which is a higher peak when compared to peak B. The counting that begins at point C ends at point G, which is a smaller valley when compared to valley C. The cycle counting continues until no more points are left in the history.

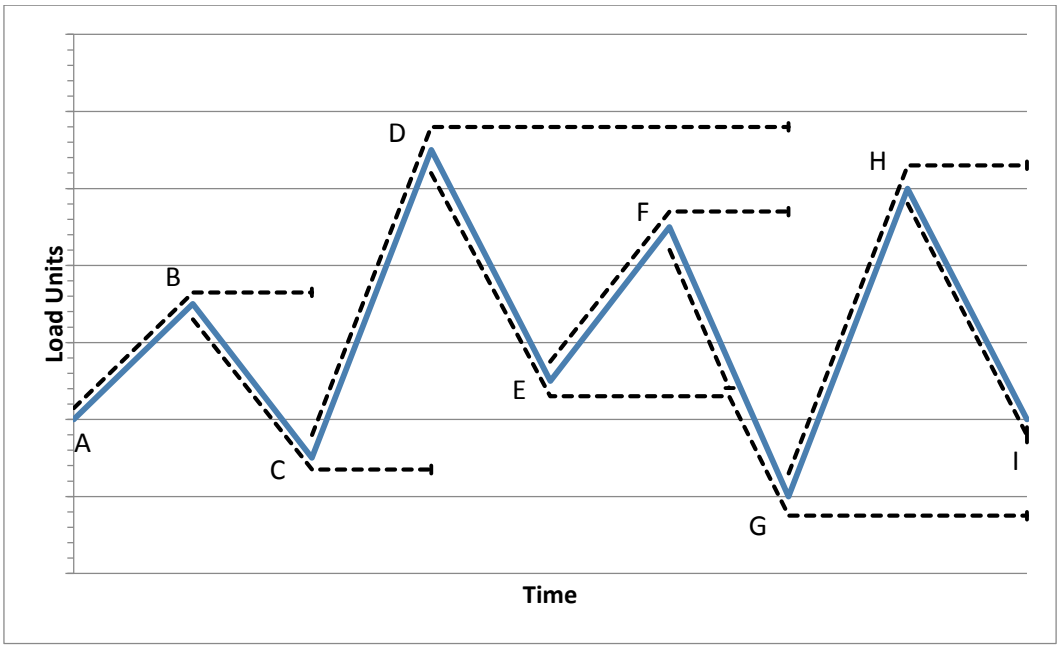

Figure 4.5: Example of the Rainflow cycle counting in the load history presented in **Figure 4.4**.

The final result of the cycle counting procedure can be summarized as six half cycles (A-B, B-C, C-D, D-G, G-H, H-I) and one full cycle (E-F). Each stress or strain range is determined as the modulus of the difference between the value of the point at the beginning and at the end of the cycle counting.

The Rainflow Method (RM) was developed and recommended for uniaxial load histories or so-called proportional load histories. However, the RM can also be used for non-proportional histories, if two modifications are made.

In the first modification, the cycle counting is applied to each stress or strain direction. Peaks and valleys belonging to the selected cycle counting stress direction determine the time steps where stress values have been taken from the other directions in order to calculate the equivalent stress compatible with the original counting. Thus, there will be as many counts as stress directions. The counting that gives the maximum fatigue damage is selected to represent the final damage.

In the second modification the stress (strain) range is no longer calculated as the modulus of the difference between values occurring at the start and end points of each half cycle counting. The range is calculated using all stress (strain) components for each half cycle counted. The ranges are calculated using the Mises equivalent or Tresca criteria. Equations (4.1) for stress and (4.4) for strains are examples of equivalent ranges to be calculated using the von Mises criterion.

Figure 4.6 is an example of a non-proportional loading history. The rainflow cycle counting performed using direction x returns the range between point A and B. The range of each direction is calculated as shown in Figure 4.7. Then, the range values are placed in equation (4.1) and the equivalent von Mises stress range is calculated.

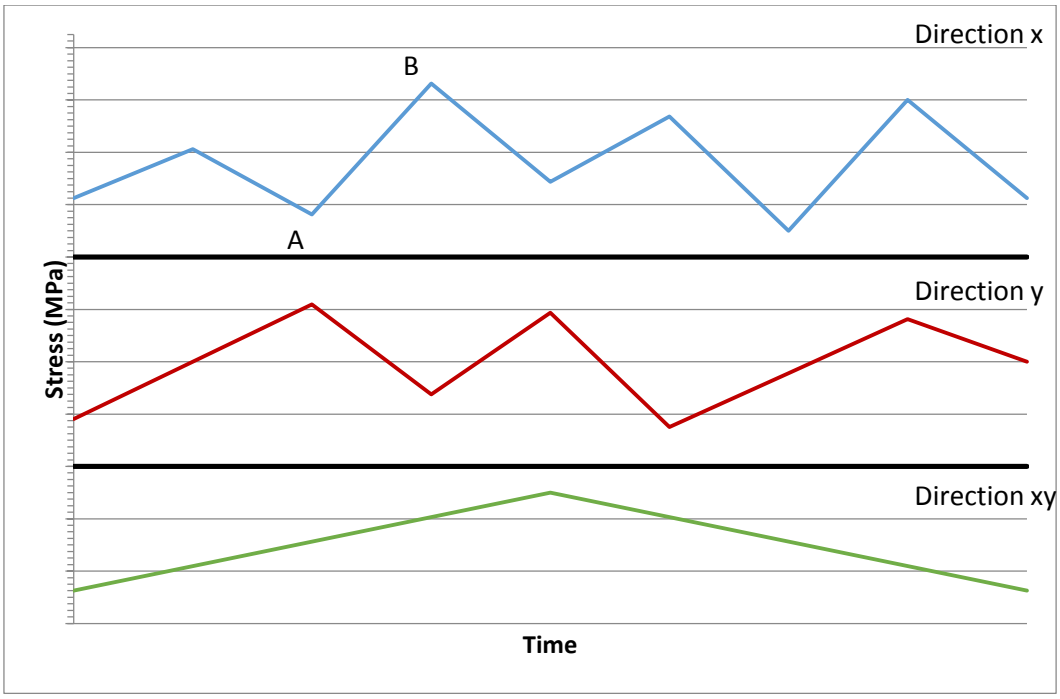

Figure 4.6: Example of a non-proportional loading history.

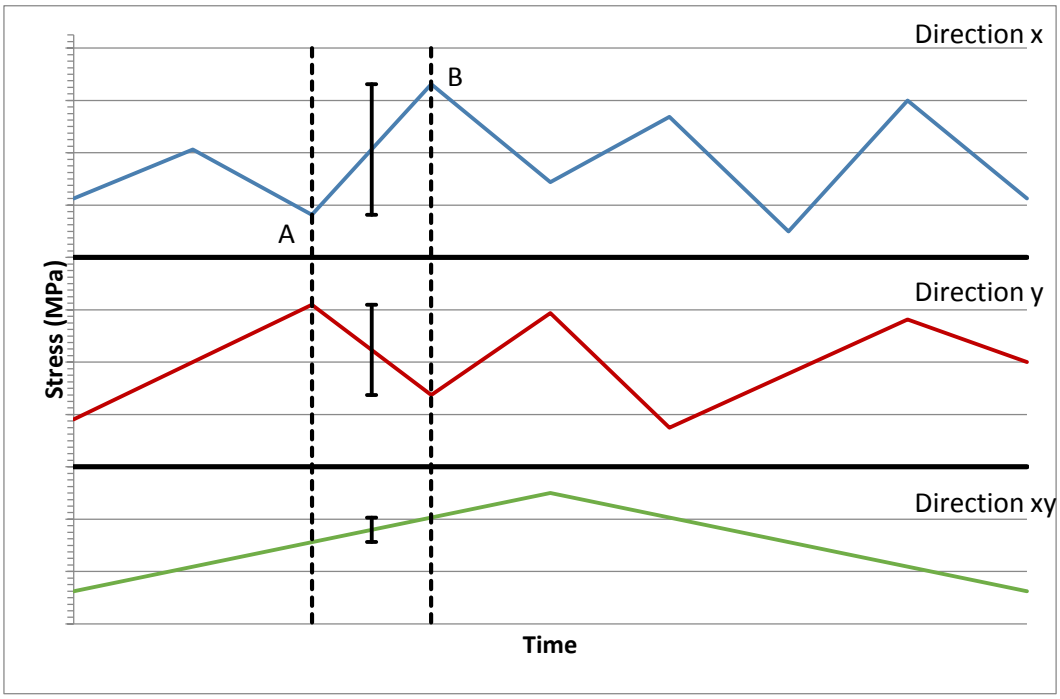

Figure 4.7: Example of the evaluation of ranges.

These two modifications, which allow a uniaxial cycle counting method to be applied to non-proportional histories, can also be implemented in the next method: The Simplified Rainflow.

4.4
Simplified Rainflow

The Simplified Rainflow is the Rainflow Method presented in ASME BPVC Section VIII, Division 2, Annex 5.B. It modifies the regular Rainflow by re-ordering the load history beforehand so that it begins and ends with either the highest peak or the lowest valley. This re-ordering eliminates the need to count half cycles; only full cycles are counted. The Simplified Rainflow routine presented in the ASME B&PV Code is summarized below:

- Step 1: Re-order the loading history to start and end at either the highest peak or lowest valley.
- Step 2: Eliminate the points that are not reversal points.
- Step 3: Read the first three points in the history.
- Step 4: Denote by X the range formed by the last two points, and by Y the range formed by the first two points.
- Step 5: Compare the absolute values of X and Y.
    - If $X < Y$, read the next point and return to Step 4.
    - If $X \geq Y$, go to Step 6
- Step 6: Count range Y as one cycle and discard its peak and valley.
- Step 7: Return to Step 3 and repeat Step 3 to 7 until no more reversal points remain.

As an example, the Simplified Rainflow is applied to the load history in **Figure 4.4**. The first step is to re-order the history so that it will begin and end at the highest peak, which is represented by point D.

Figure 4.8 shows the re-ordered history. After the history is re-ordered, one can see that points A and I have the same values and are now next to each other. Using step 2 of the procedure, points A and I have been transformed into only one point (Point I,A), as shown in **Figure 4.8**.

From step 3, after having read points D, E and F, and in agreement with step 4, range E-F is denoted X and D-E is denoted Y. Since X is less than Y, the next

point is read. This times, range F-G denotes range X and E-F denotes range Y. Because X is greater than Y, the range between E-F is counted as a full cycle and points E and F are eliminated. The result of eliminating of points E and F can be seen in **Figure 4.9**.

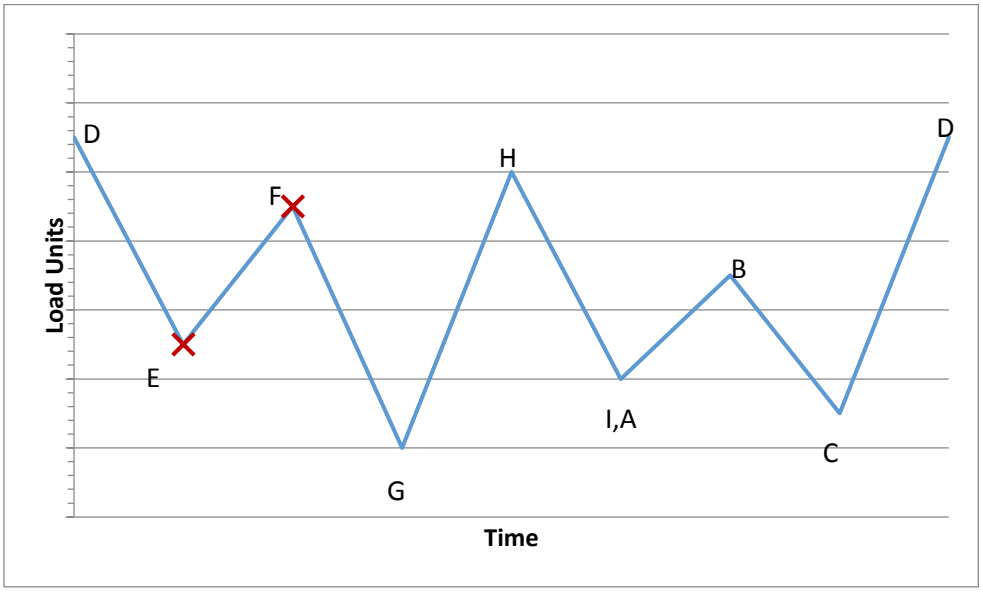

Figure 4.8: First part of the Simplified Rainflow method example.

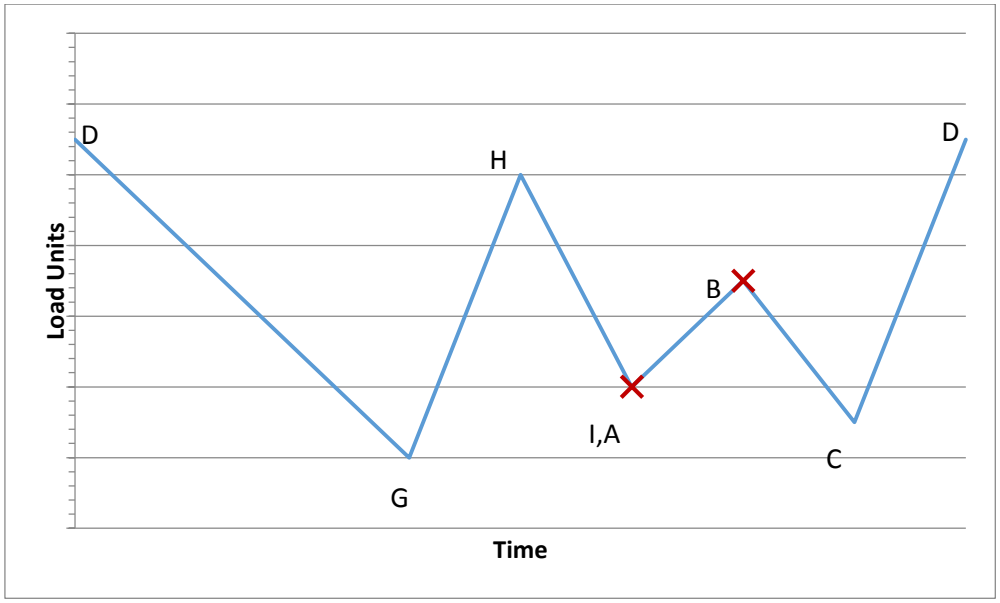

Figure 4.9: Second part of the Simplified Rainflow method example.

Once one cycle has been counted, the routine returns to step 3, now reading the first three points: D, G and H. The routine continues as described until points I, A and B are counted. The cycle counting continues as shown in **Figure 4.10** and **Figure 4.11**.

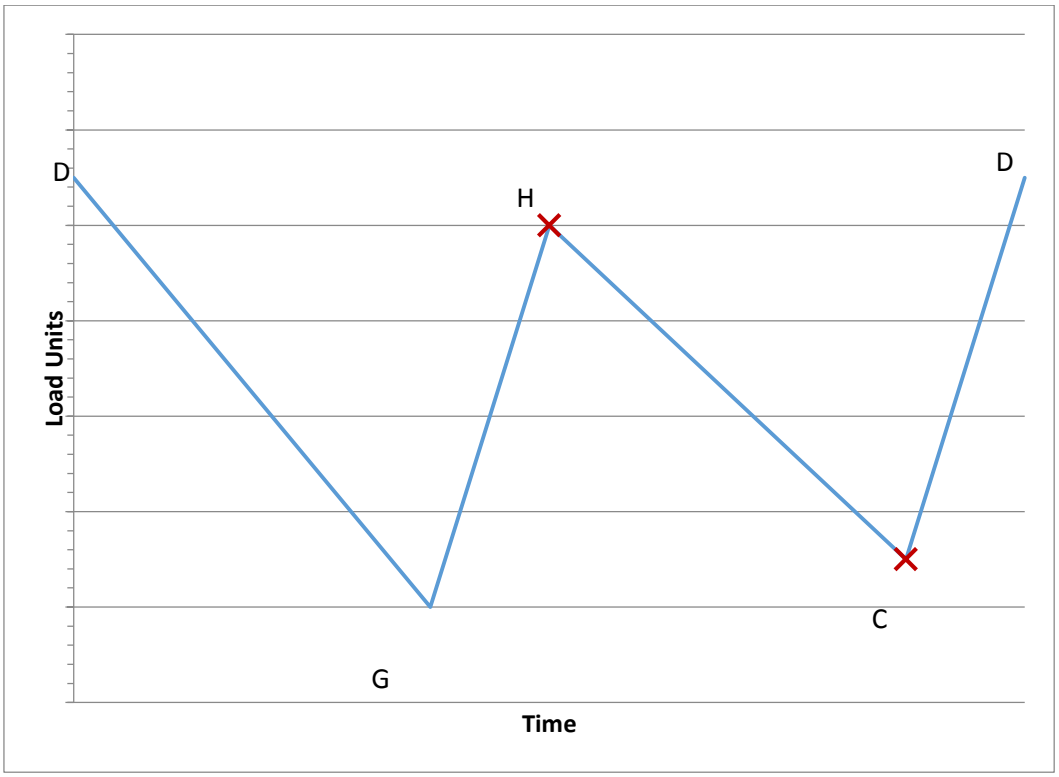

Figure 4.10: Third part of the Simplified Rainflow method example.

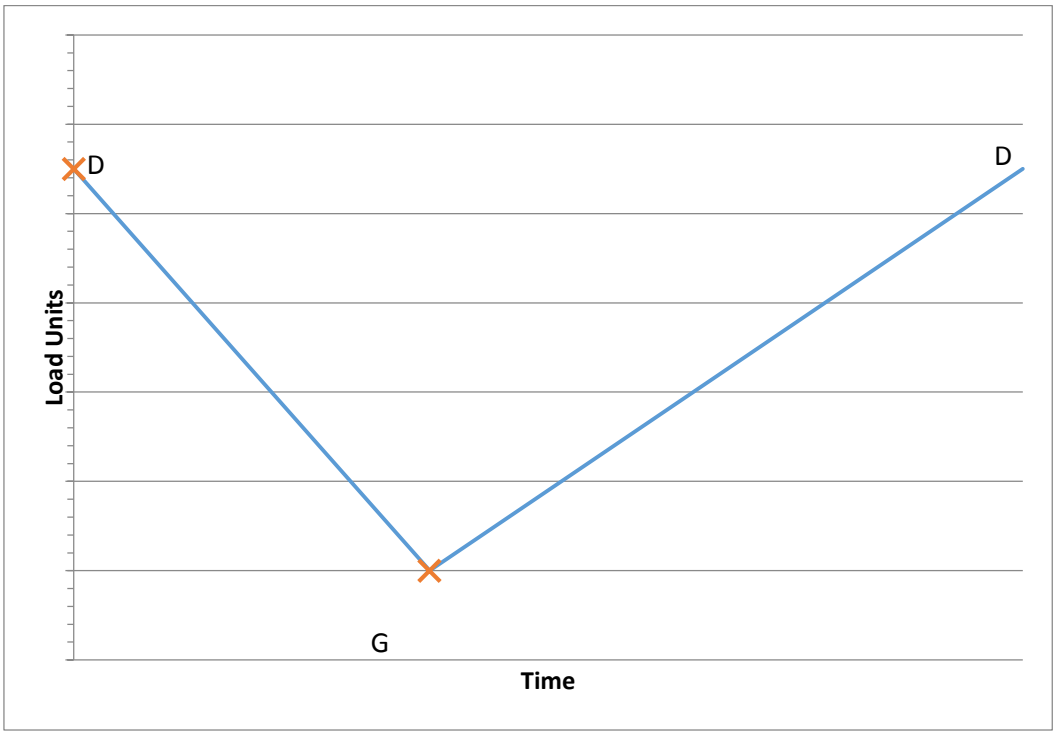

Figure 4.11: Last part of the Simplified Rainflow method example.

The cycle counting is finished because, after deleting point D and G, as shown in Figure 4.11, there are no more reversal points in the history. The final result is then four full cycles (E-F, B-I, A, H-C, D-G). These counting results are different from the one obtained with the traditional Rainflow. However, it is already

known that the results obtained with the Simplified Rainflow are equal to, or are more conservative than, those obtained with the traditional Rainflow Method.

4.5
Bannantine and Socie

The method proposed by Bannantine and Socie, [15, 24, 26], is based on a combination of the critical plane concept (explained in the previous chapter) and the Rainflow cycle counting method.

This method consists in analyzing the strain (or stress) components of the load history on a candidate failure plane, followed by the use of the Rainflow cycle counting method applied to the shear or normal strain acting on the candidate plane. Whether to count the shear strain or the normal strain depends on the failure mode of the material: shear strain for shear failure prone materials and normal strain for tensile failure prone materials. Consequently, the effects of the normal strain in the shear strain failure mode and vice versa are not considered.

Other required parameters, such as the maximum normal stress for the Fatamie and Socie damage model and for the Smith-Watson-Topper damage model, can be determined for each counted cycle as the maximum normal stress value that occurred during the cycle being counted, as shown in **Figure 4.12**.

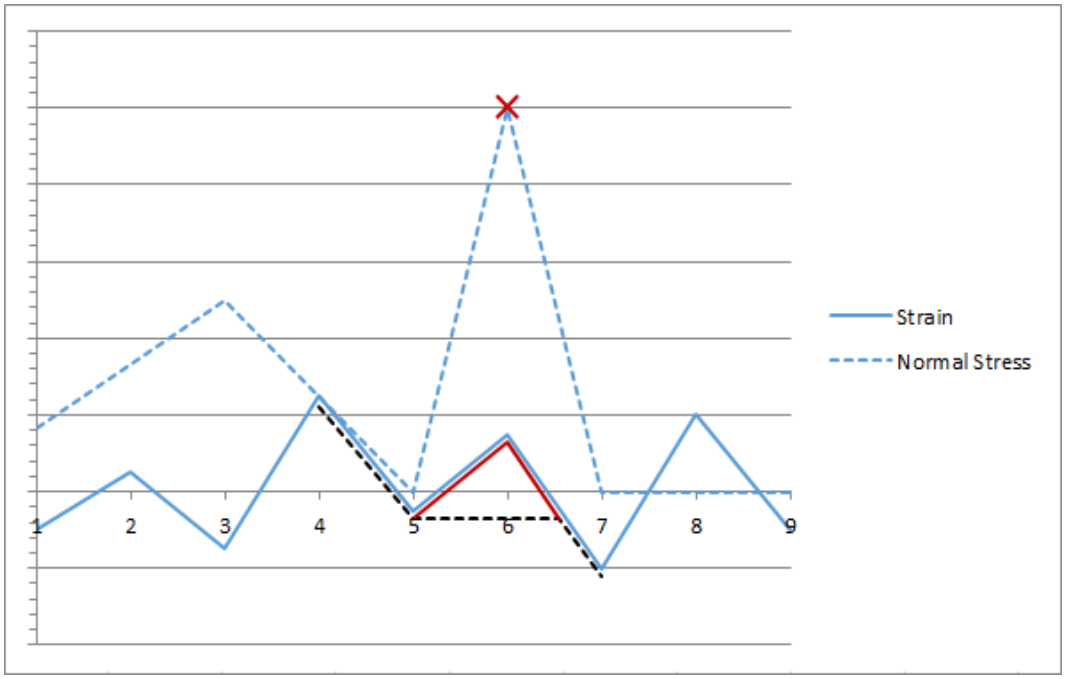

Figure 4.12: Example of the Bannantine and Socie method**.**

The example in **Figure 4.12** shows the Bannantine and Socie cycle counting method performed on the strains. At a certain point of the counting, the Rainflow will return the cycle counted indicated in red. The maximum value of the normal stress between these two points is the one marked with a red cross.

4.6
Wang-Brown

Wang and Brown proposed a cycle counting method [27] that is applicable to any proportional or non-proportional strain (or stress) history. This method generalizes the Rainflow Method and is based on cycle counting the equivalent von Mises strain.

Since the equivalent von Mises strain is always positive, the method uses the relative equivalent strain to count the cycles. The steps to apply the method are as follows:

- Step 1: Select the point in the history with the largest von Mises strain and re-order the history so that it will start and end at this point. Start the cycle-counting using this first point in the history.
- Step 2: Using this first point, calculate the relative von Mises strain for the entire history using equation (4.4) and changing ε_{ij} by $\Delta\varepsilon_{ij} = \varepsilon_{ij}^{T} - \varepsilon_{ij}^{P}$, (where ε_{ij}^{P} is the point under consideration and ε_{ij}^{T} is the other point in the strain history).
- Step 3: The final point to close the cycle is identified when the cycle counting routine reaches the highest value of the relative von Mises strain, or when it reaches a previously counted path.
- Step 4: Count that as a half cycle, go to the next point and repeat steps 2 to 4 until every point in the history is evaluated.

An example of this cycle counting in a $\gamma_{xy}\ x\ \varepsilon_x$ is represented in [28]. The example uses a non-proportional history with the following strains in percentage values: $(\varepsilon_x, \gamma_{xy}) = (2,1) \rightarrow (-1,2) \rightarrow (2,-2) \rightarrow (-2,-2) \rightarrow (2,2) \rightarrow (-2,0)$.

Assuming that v_{el}=0.3 and $\varepsilon_{el} \cong \varepsilon_{pl}$, equation (4.7) gives the mean Poisson coefficient ($\bar{v}$) equal to 0.4. Considering that $\sigma_x = \sigma_y = 0$ (since the history is given using the example of an torsion and tensile strain controlled experiment, only the

stress σ_z and the shear stress will be different than zero), Hooke's law implies $\varepsilon_y = \varepsilon_z = -\bar{\nu}\varepsilon_x$ and the equivalent von Mises strain presented in equation (4.4) can be simplified as:

$$\varepsilon_{Mises} = \sqrt{\varepsilon_x^2 + 3\left(\frac{\gamma_{xy}}{2(1+\bar{\nu})}\right)^2} \tag{4.8}$$

The procedure begins by re-ordering the history. The history starts and ends at points 1 and 7 with strains equal to $(2{,}2)$, as shown in **Figure 4.13**. Substituting Points 1, 5 and 6 in equation (4.8), one can see that the three points have the same equivalent von Mises strain, so choosing between points 1, 5 or 6 to start the history is just a matter of choice. The history can also be represented and counted using the strain plot in **Figure 4.14**.

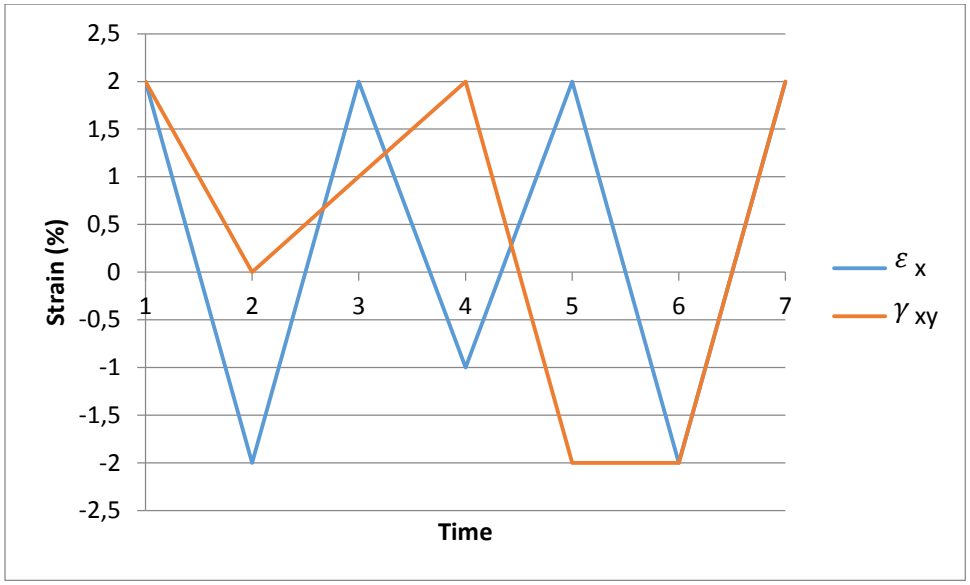

Figure 4.13: Re-ordered strain history for the given example.

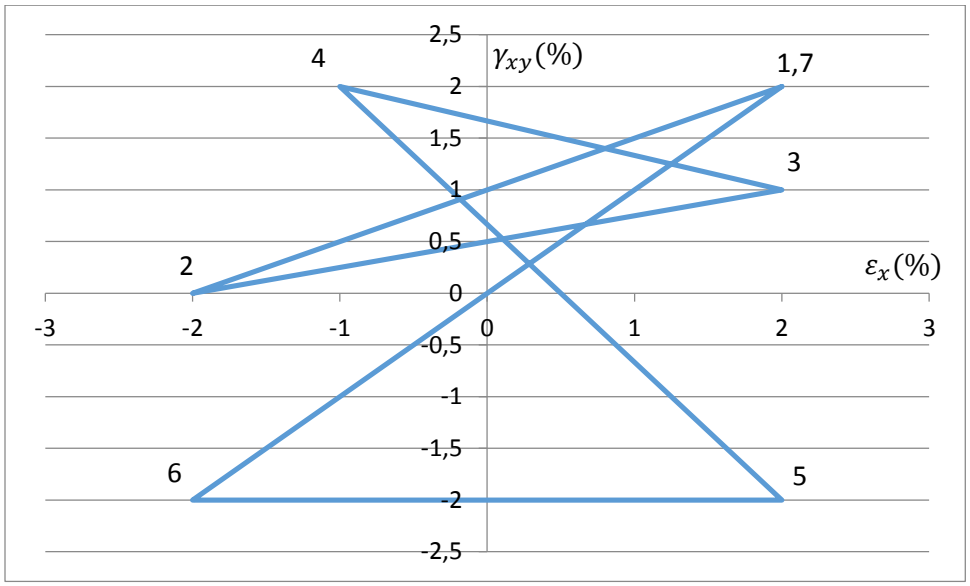

Figure 4.14: Representation of the history in a γ_{xy} x ε_x diagram.

The cycle counting starts at point 1. Using point 1 as the reference, the history of the relative von Mises strain is determined with equation (4.9) and illustrated in **Figure 4.15**. The relative von Mises strain with point 1 as the reference, equation (4.9) is obtained by rearranging equation (4.8).

$$\varepsilon_{Rel\ Mises}(Point\ 1) = \sqrt{(\varepsilon_x - 2\%)^2 + 3\left(\frac{\gamma_{xy}-2\%}{2(1+\bar{\nu})}\right)^2} \qquad (4.9)$$

After calculating the history of the relative von Mises strain, the cycle counting is performed and stops at the highest point. The result is a half cycle with points 1-2-2'-7, shown in **Figure 4.15**. Point 2' is the projection of the reversal point 2 onto the path between points 5 and 6; the position of the projection in the history needs to be calculated and is described with parameter α as:

$$\left(\varepsilon_x(2'), \gamma_{xy}(2')\right) = \left(\varepsilon_x(5), \gamma_{xy}(5)\right) + \alpha \cdot \left[\left(\varepsilon_x(6), \gamma_{xy}(6)\right) - \left(\varepsilon_x(5), \gamma_{xy}(5)\right)\right] \quad (4.10)$$

Thus, the values of the strains in terms of α are $\varepsilon_x(2')$ = 2 - 4α and $\gamma_{xy}(2')$ = -2. Since the value of the relative Mises strain with respect to point 1 must be equal at point 2 and point 2', the value of α can be found using equation (4.9), where the value on the left side is equal to 4.19% (the value of the relative Mises strain in **Figure 4.14** at point 2), the value of ε_x and γ_{xy} is equal to 2 - 4α and -2, respectively. Hence α is equal to 0.844, $\varepsilon_x(2')$ = -1.378%, and $\gamma_{xy}(2')$ = -2%.

Thus, the values of the strains in terms of α are $\varepsilon_x(2')$ = 2 - 4α and $\gamma_{xy}(2')$ = -2. Since the value of the relative Mises strain with respect to point 1 must be equal at point 2 and point 2', the value of α can be found using equation (4.9),

where the value on the left side is equal to 4.19% (the value of the relative Mises strain in **Figure 4.14** at point 2), the value of ε_x and γ_{xy} is equal to 2 - 4α and -2, respectively. Hence α is equal to 0.844, $\varepsilon_x(2') = -1.378\%$, and $\gamma_{xy}(2') = -2\%$.

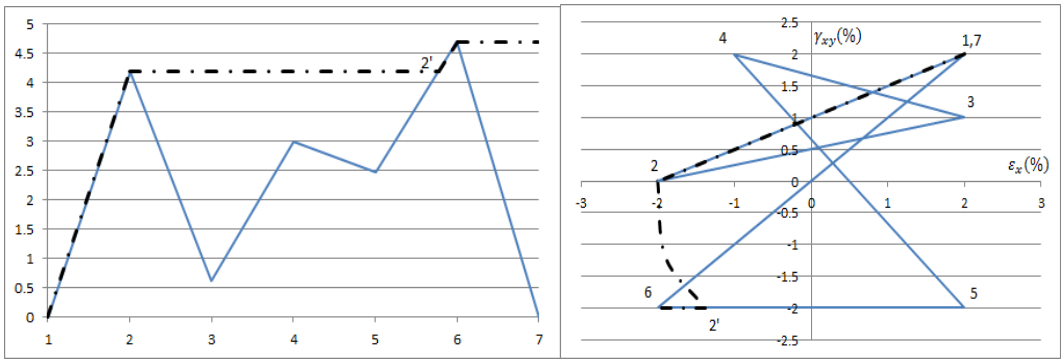

Figure 4.15: Count of the first event.

The need to calculate the location of the projection of the reversal point is due to the rule from step 3 of the procedure. During the count of the first event shown in **Figure 4.15**, path 2'-6 was counted, so if a subsequent count passes along this path, it will have to stop at point 2'.

Once the first cycle has been counted, the next step is to do the second count. This count starts at point 2, so the entire history is converted to a relative von Mises strain with respect to point 2. To do so, equation (4.9) is changed to:

$$\varepsilon_{Rel\ Mises}(Point\ 1) = \sqrt{(\varepsilon_x + 2\%)^2 + 3\left(\frac{\gamma_{xy} - 0\%}{2(1+\bar{\nu})}\right)^2} \qquad (4.11)$$

The counting ends at point 7 and the result is a half cycle with points 2-3-3'-4-7. The projection of reversal point 3' is calculated by changing equation (4.10) to equation (4.12), and the procedure is repeated as described before.

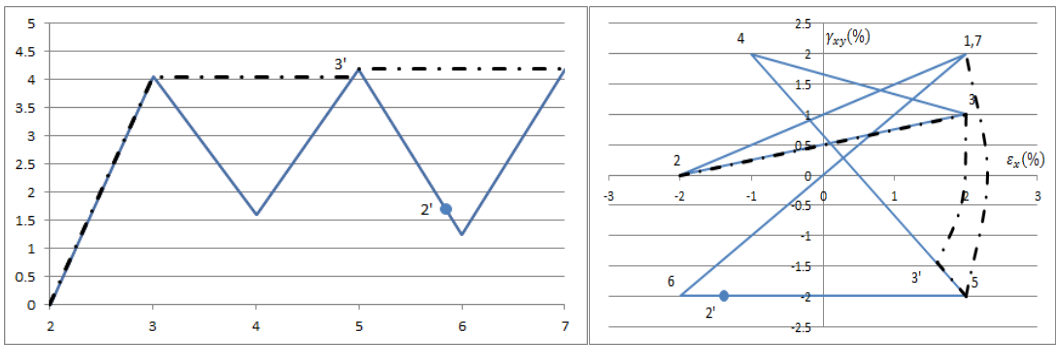

Figure 4.16: Count of the second event.

$$\left(\varepsilon_x(3'), \gamma_{xy}(3')\right) = \left(\varepsilon_x(4), \gamma_{xy}(4)\right) + \alpha \cdot \left[\left(\varepsilon_x(5), \gamma_{xy}(5)\right) - \left(\varepsilon_x(4), \gamma_{xy}(4)\right)\right] \qquad (4.12)$$

The routine of this cycle counting method continues until every point is counted - in this example, until the counting reaches point 6.

This method can also be applied using the stress in equation (4.1) instead of equation (4.4), and changing σ_{ij} to $\Delta\sigma_{ij} = \sigma_{ij}^{T} - \sigma_{ij}^{P}$.

The previous counting example was done using only two strain components. Nevertheless, the method can be applied even with a full tensor, with the procedures being analogous.

4.7
Modified Wang-Brown

Meggiolaro and Castro [28] proposed two modifications to the Wang-Brown method. The first one was to reduce the strain (or stress) history to a five dimensional Euclidian space. Hence, the entire history can be represented as points in space ($P_i = (e_1, e_2, e_3, e_4, e_5)$ for strains and $P_i = (S_1, S_2, S_3, S_4, S_5)$ for stresses. The dimensional reduction is accomplished with the following equations:

$$S_1 \equiv \sigma_x - \frac{\sigma_y}{2} - \frac{\sigma_z}{2},\ S_2 \equiv \frac{\sigma_y - \sigma_z}{2}\sqrt{3},\ S_3 \equiv \tau_{xy}\sqrt{3},\ S_4 \equiv \tau_{xz}\sqrt{3},\ S_5 \equiv \tau_{yz}\sqrt{3} \qquad (4.13)$$

$$e_1 \equiv \frac{2\varepsilon_x - \varepsilon_y - \varepsilon_z}{2(1+\bar{\nu})},\ e_2 \equiv \frac{\varepsilon_y - \varepsilon_z}{2(1+\bar{\nu})},\ e_3 \equiv \frac{\gamma_{xy}\sqrt{3}}{2(1+\bar{\nu})},\ e_4 \equiv \frac{\gamma_{xz}\sqrt{3}}{2(1+\bar{\nu})},\ e_5 \equiv \frac{\gamma_{yz}\sqrt{3}}{2(1+\bar{\nu})} \qquad (4.14)$$

where $\bar{\nu}$ was defined in equation (4.7).

This reduction makes the Wang-Brown counting routine simpler. In such reduced space, the distance between two points is the relative von Mises strain (or stress). Hence, there is no need to evaluate the relative von Mises strain (or stress) for every point, since this value can be easily obtained by calculating the distance between the points.

The second modification proposed by Meggiolaro and Castro involves the first step in the Wang-Brown cycle counting routine. Originally, the first step tries to guarantee the identification of the highest range of the load history. However, using a simple example it is possible to show that this will not occur in some histories.

Consider the following non-proportional history ($\varepsilon_x, \varepsilon_y$): (0.6%, 0%) → (0%, 0.8%) → (-0.5%, 0%). The Wang-Brown routine starts at the second point, the one that has the highest equivalent strain, resulting in two half cycles of combinations between the first and second points, with a relative von Mises strain equal to

$\sqrt{0.52}/(1+\bar{v})$. However, if the relative von Mises strain between the first and the third points is calculated, the result is equal to $\sqrt{0.605}/(1+\bar{v})$, resulting in a higher value when compared with the result of the Wang-Brown cycle counting.

Thus, the modification proposed by Meggiolaro and Castro (MWB) is to first find the pair of points that will produce the highest range of relative von Mises strains, and then use the point with the highest equivalent strain to start the cycle counting. With these modifications, the final routine of the MWB is expressed by the following steps:

- Step 1: Convert the entire history into a five dimensional Euclidian space. If it is a strain history, use equation (4.14), otherwise, use equation (4.13).
- Step 2: Find in the history the pair of points that are farthest from each other. Between those points, choose the one with the greatest distance from the origin. This is the point where the cycle count begins.
- Step 3: The point under consideration is going to be the initial point (P_i).
- Step 4: The final point, (P_f), is found when a point with the greatest distance in relation to P_i is found, or when a segment from a previous count is found.
- Step 5: Count a half cycle from P_f to P_i, go to the next point, and then return to step 3 until every point has been counted.

The example in subchapter 4.6 (Wang-Brown) is repeated to show how the MWB counting is performed. First, using equation (4.14), the entire strain history is converted into a five dimensional Euclidian space, using the assumptions made previously (that lead to the result $\varepsilon_y = \varepsilon_z = -\bar{v}\varepsilon_x$). The conversion can be simplified as: $e_1 = \varepsilon_x, e_3 = \gamma_{xy}\sqrt{3}/2(1+\bar{v}), e_2 = e_4 = e_5 = 0$. Therefore, the history can be presented using the diagram in **Figure 4.17**:

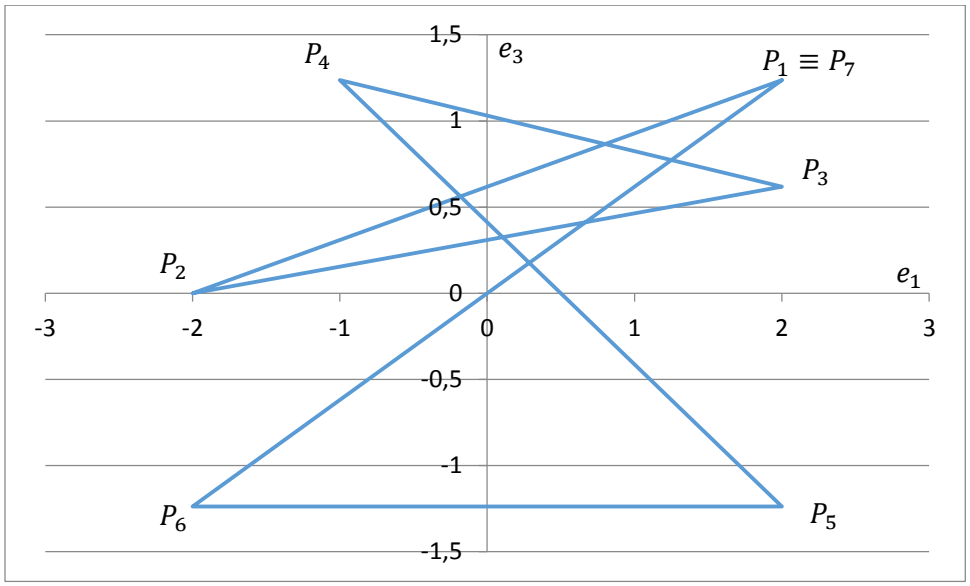

Figure 4.17: Strain history presented in a $e_1 x\ e_3$ diagram.

In step 2, a search is made among the pairs of points in the history, looking for the pair that has points that are located farthest from each other. The pair formed by points P_1 and P_6 returns the largest distance between them. Since both points have the same Mises strain, it does not matter which one of these points is chosen to start the counting process. In this example, point P_1 was chosen to start the cycle counting.

Proceeding to step 3, point P_1 is the point under consideration, point P_6 is the farthest point from the point under consideration, and the result of the counted cycle is P_1-P_2-P_2,-P_6, as shown in **Figure 4.18**.

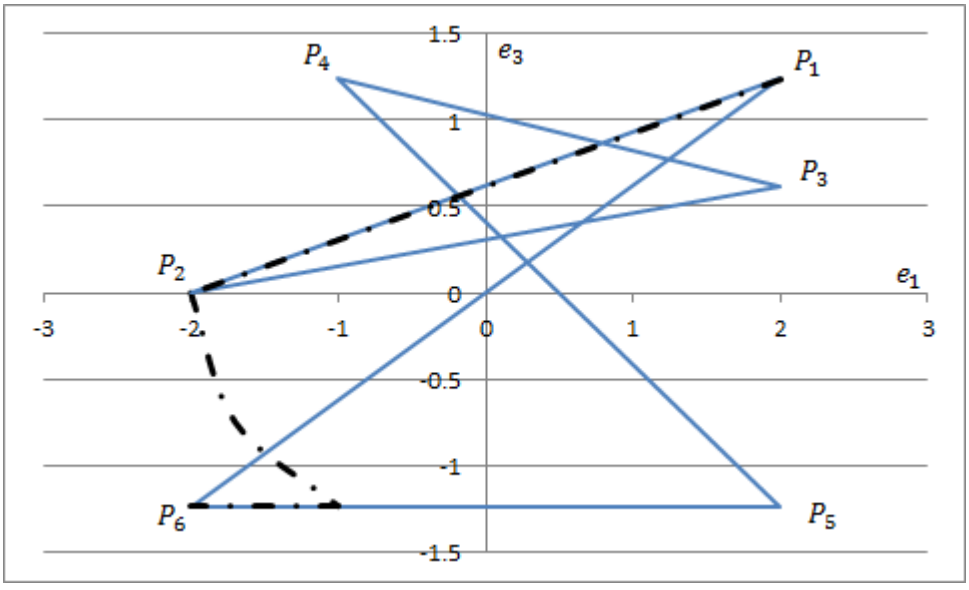

Figure 4.18: Count of the first event.

An easier way to locate the projections of the reversal points is also proposed in [28]. The idea is to calculate the value of α using Stewart's Theorem [29] for the triangle formed, in this case, by P_1, P_5, P_6.

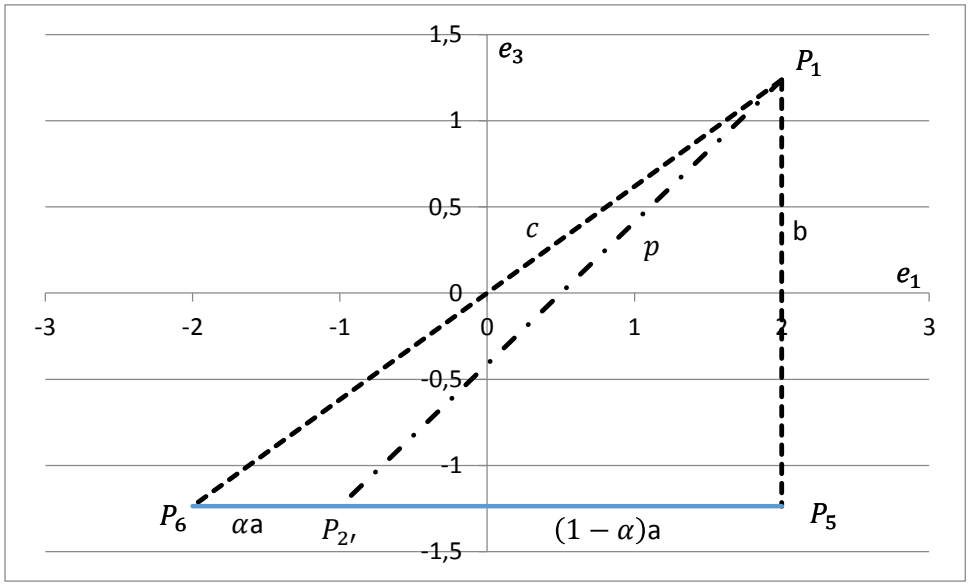

Figure 4.19: Example of the calculation to locate the projection of reversal point $P_{2'}$.

The letters in **Figure 4.19** are the distances between each point, a = $|P_6 - P_5|$, b = $|P_5 - P_1|$, c = $|P_6 - P_1|$ and p = $|P_2 - P_1|$. The solution for α is obtained using the following equation:

$$\alpha = \frac{(a^2+b^2-c^2) \pm \sqrt{(a^2+b^2-c^2)^2 - 4a^2(b^2-p^2)}}{2a^2} \quad (4.15)$$

The value of α is the lowest value between the two solutions that are inside intervals 0 and 1. In the example the values of α using equation (4.15) are 0.8444 and -0.8444 (the second solution is outside the interval allowed, so the value of α is 0.8444). This is the same value obtained in the example shown previously, the difference being the simplicity of implementation.

With the first cycle counted and the projection of the reversal point located, the cycle counting continues with the second cycle. The second cycle starts at point P_2, and the farthest point from the point under consideration is point P_7. The result of this count is a half cycle with points P_2-P_3-$P_{3'}$-P_5-P_7, where point P_3 is determined using the same method previously described (using triangle P_2, P_4, P_5).

The cycle counting continues until all the points are counted; in the case of this example, until point P_6 is counted.

Meggiolaro and Castro also recommend using an enclosing surface solution fitting the full and half cycles in order to calculate the parameters needed

to obtain the fatigue damage associated with each cycle. Then, to evaluate the total damage, a damage accumulation rule (Miner's rule for example) is adopted. If a critical plane approach is used, repeat the entire procedure for each plane using only the shear strains (or stresses) or the normal strain (or stress) acting on the plane of analysis - depending on the damage model that is being used - instead of the full tensor. The plane that maximizes the damage will be the critical plane and the damage accumulated on that plane will be the result.

4.8
Path-Dependent Maximum Range (PMDR)

The PMDR method is a cycle counting method proposed by Dong, Wei and Hong [30] for performing fatigue evaluations on components under variable-amplitude and arbitrary multiaxial conditions. With this method it is possible to determine the strain (or stress) ranges, in addition to another parameter that the authors called the path-dependent effective strain (or stress).

The PMDR can be defined as a cycle counting method that searches for the farthest two points in the stress (or strain) space of a given history. The path traveled between those two points is then recorded as the path-dependent effective stress (or strain). A history of normal and shear stresses presented in [30] is reproduced here to illustrate the method.

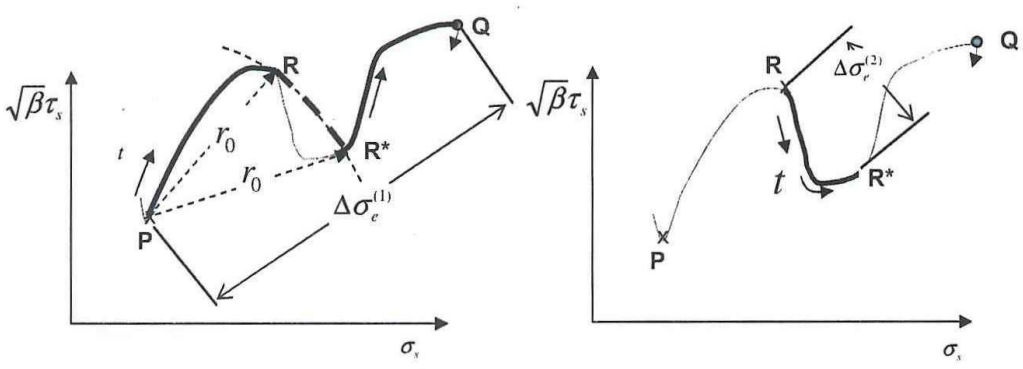

Figure 4.20: Illustration of the PMDR method.

The method can be described using the history from **Figure 4.20** from P to Q:

- Step 1: Convert the entire stress history into a $\sigma - \sqrt{3}\tau$ space, as shown in **Figure 4.20**.

- Step 2: Find the point (Q) farthest from the point under consideration (Point P). While searching, make sure that the distance is always increasing. If a point where the distance starts to decrease is found, the previous point (Point R) is identified as a local maximum or a turning point, and the projection of the turning point in the load path PQ (Point R*) has to be found.

  The projection is the intersection between the load path and the circumference centered at the point under consideration (Point P), with the radius equal to the distance of the local maximum (Point R). The search for the farthest point continues, starting from the projection of the turning point (R*) until the load path ends, no more turning points are found, or the farthest point is found (Point Q).

- Step 3: Count one half cycle and record the maximum distance ($\Delta\sigma_e$) between the two points counted (P and Q) as the stress range, and the path traveled between the two points (PR + RR*' + R*Q, where RR*' is the virtual path between R and R*) as the path-dependent effective stress.
- Step 4: Repeat Steps 2 and 3 for the remaining load paths (R-R*).
- Step 5: Repeat Steps 2 to 4 until every path has been counted only once.

This method can also be used on strains; the only modification needed is that the strain history has to be converted into a $\varepsilon - \gamma/\sqrt{3}$ space.

It is recommended that the PMDR be adopted in a critical plane approach. In this case the stresses (or strains) must be those that act on the plane of analysis, with the load history replaced by the three stress (or strain) components' history - one normal stress and two shear stresses.

The method can be used to transform the history into a $\sigma - \sqrt{3}\tau_s - \sqrt{3}\tau_z$ space (if the cycle counting is applied to the strain history, the strain space to be considered is the $\varepsilon - \gamma_s/\sqrt{3} - \gamma_z/\sqrt{3}$ space) as shown in **Figure 4.21**, where sub index s is the shear stress (or strain) in one direction and sub index z is the shear stress (or strain) perpendicular to s.

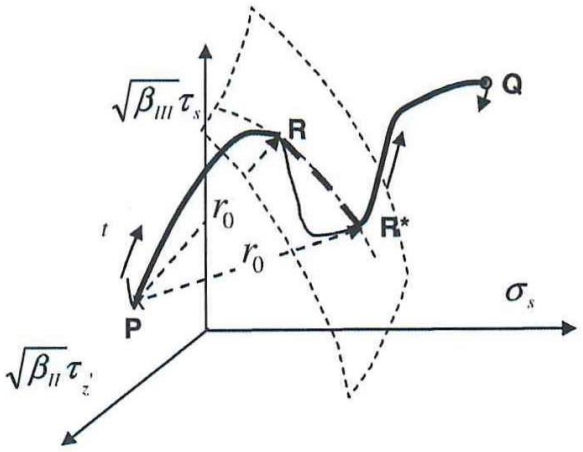

Figure 4.21: Illustration of the PMDR method in 3-D.

The major advantage of the PMDR and the MWB cycle counting methods is that they return not only stress or strain ranges, but they also return the paths between the two points that were counted. This is a very important parameter, since, as discussed in the previous chapter, the damage is also induced by the loading path.

It is interesting to note that if the PMDR method is applied to the example in subchapter 4.7, it will return exactly the same result as the cycle counting given by the Modified Wang-Brown.

Nevertheless, the computational implementation of the Modified Wang-Brown is simpler. In addition to that, the PMDR cycle counting method mix damage caused by tensile and shear strain (or stress), Figure 4.22 shows a case where this phenomenon is better observed.

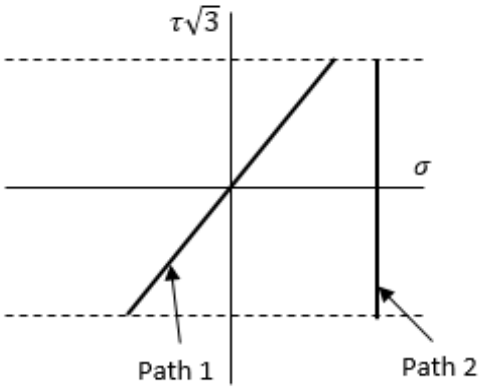

Figure 4.22: Illustration of the mixture of damage caused by tensile and shear stress.

In the above figure, one can see two loading paths. When calculating the damage using a model that mixes tensile and shear stress, the two paths will

display the same damage. However, this is not true since the two loading paths have the same shear amplitude, but path 2 has a higher value of mean normal stress, which will cause more damage.

For that reason, and for a more efficient way of detecting the projection of the reversal points, the MWB turns out to be the better choice. A small change on the flowchart presented in [28] is proposed in **Figure 4.23**.

With this small change, the algorithm for the Modified Wang-Brown cycle counting method will ensure the return of the path, by returning the points that the cycle counting passes when travelling between two extreme points.

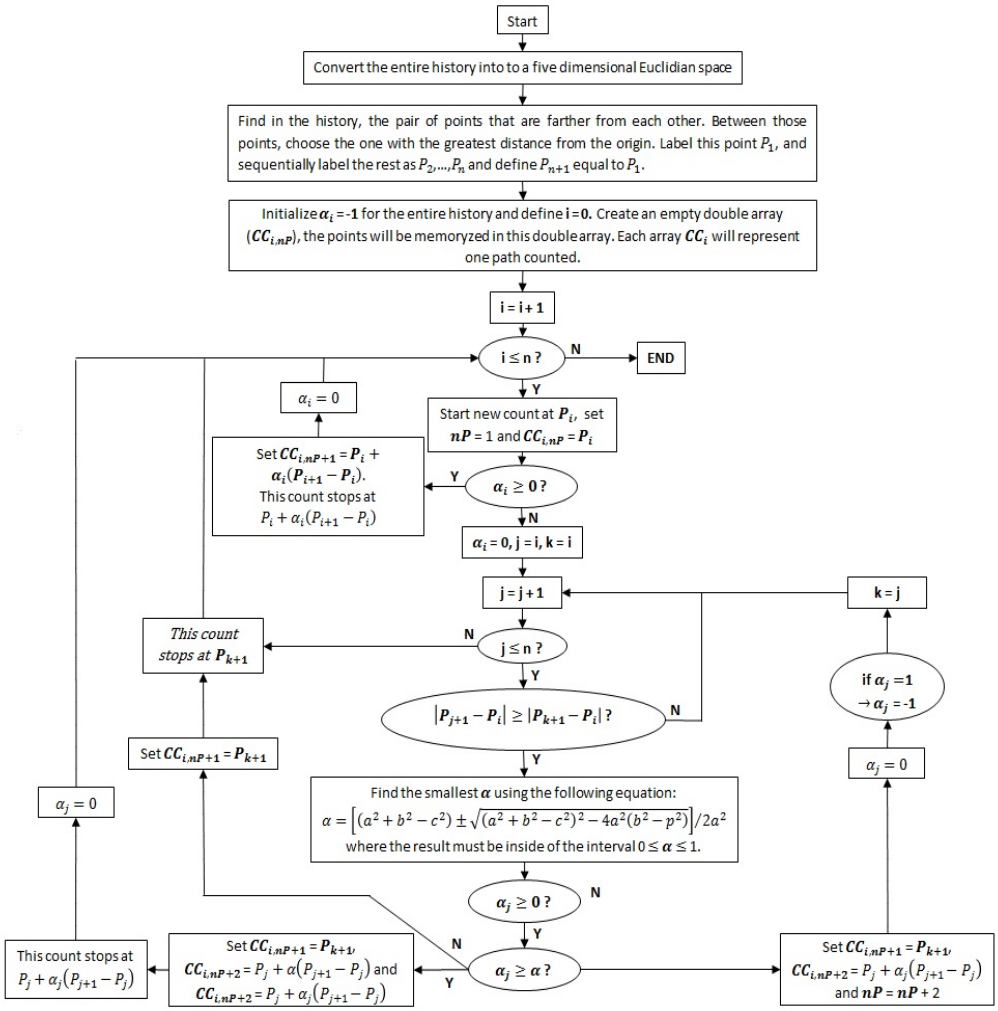

Figure 4.23: Flowchart of the proposed modification of the Modified Wang-Brown.

5

Non-Proportional Stress/Strain Time History

5.1

Introduction

Some of the models in Chapter 3 use not only the stress or the strain history, but also a combination of both parameters to evaluate the damage caused by fatigue. Therefore, the presentation of mathematical models capable of relating strains and stresses along the loading history are required for the damage models and cycle counting methods.

There are two different problems to solve. The first one involves the case where the strain history is already given and thus the stress history must be calculated. This happens in strain-controlled tests or in equipment in operation where strains are measured using strain-gauges. The second problem occurs when stresses are calculated based on geometry, material and loading conditions.

These problems can be subcategorized into two conditions: elastic and plastic. The proper way to evaluate the stress-strain relationship regarding non-proportional histories will be presented in this chapter for both elastic and plastic conditions.

5.2

Elastic Stress-Strain Relations

If the stress or strain values are small enough (typically less than the value of the yield stress or yield strain), the relationship can be established using a linear elastic isotropic model. The model used for this case is Hooke's law:

$$\varepsilon_x = \frac{1}{E}\left[\sigma_x - v(\sigma_y + \sigma_z)\right]$$

$$\varepsilon_y = \frac{1}{E}\left[\sigma_y - v(\sigma_x + \sigma_z)\right]$$

$$\varepsilon_z = \frac{1}{E}\left[\sigma_z - v(\sigma_x + \sigma_y)\right] \tag{5.1}$$

$$\gamma_{xy} = \frac{\tau_{xy}}{G}$$

$$\gamma_{xz} = \frac{\tau_{xz}}{G}$$

$$\gamma_{yz} = \frac{\tau_{yz}}{G}$$

where E is the elastic modulus of the material, v is the Poisson coefficient and G is the elastic shear modulus, calculated using the following equation:

$$G = \frac{E}{2(1+v)} \tag{5.2}$$

The equations can be rearranged in such a way that the stress values are calculated using known strain values:

$$\sigma_x = \frac{E}{(1+v)(1-2v)}\left[(1-v)\varepsilon_x + v\left(\varepsilon_y + \varepsilon_z\right)\right]$$

$$\sigma_y = \frac{E}{(1+v)(1-2v)}\left[(1-v)\varepsilon_y + v(\varepsilon_x + \varepsilon_z)\right]$$

$$\sigma_z = \frac{E}{(1+v)(1-2v)}\left[(1-v)\varepsilon_z + v\left(\varepsilon_x + \varepsilon_y\right)\right] \tag{5.3}$$

$$\tau_{xy} = \frac{E}{(1+v)}\frac{\gamma_{xy}}{2}$$

$$\tau_{xz} = \frac{E}{(1+v)}\frac{\gamma_{xz}}{2}$$

$$\tau_{yz} = \frac{E}{(1+v)}\frac{\gamma_{yz}}{2}$$

Equations (5.1) and (5.3) show that stress-strain relations are simpler and unique, meaning that, for a given value of a stress state, there is only one strain state value. This is not the case under a plastic condition.

5.3
Plastic Stress-Strain Relations

Under a plastic condition, the stress-strain relationship is no longer linear and uniquely defined. The visualization of this non-unique property can be seen in **Figure 3.2(b)** (and again in **Figure 5.1**).

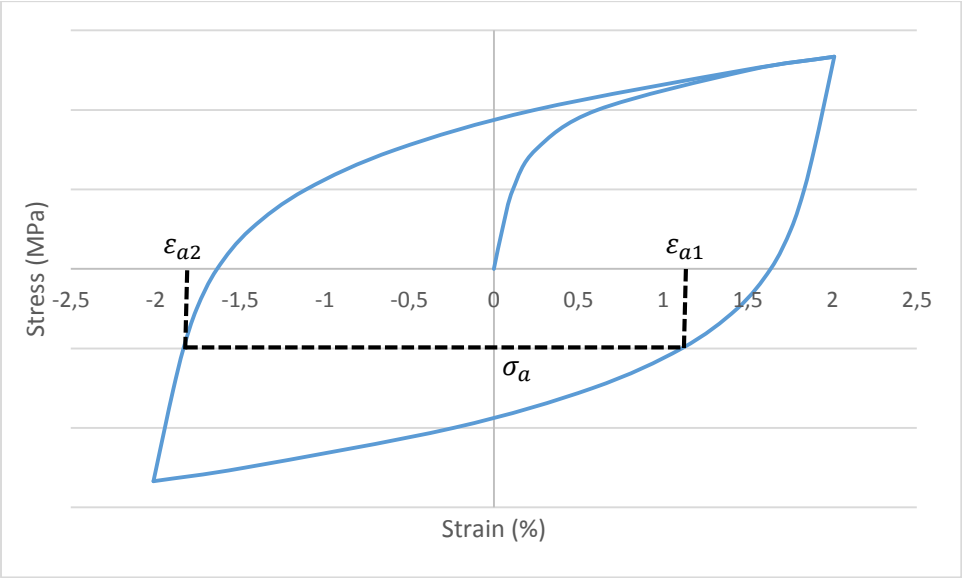

Figure 5.1: Representation of the non-unique stress-strain relationship.

As noted in Figure 5.1, two different strain values (ε_{a1} and ε_{a2}) can be related to a given state of stress, σ_a. Thus, strains cannot be related only to the present stress state. The proper relationship can be established by knowing the present stress state together with the previous stress-strain state. The reasons for using both conditions are explained further in the present chapter.

Since the main goal of this work is to evaluate the fatigue damage caused by repetitive loads, the models used here have to establish a proper knowledge of the strain-stress relationship under a cyclic deformation condition. Stress-strain relationships are modeled using certain plastic behaviors described by different models such as: isotropic hardening, kinematic hardening, cyclic creep or ratcheting, mean stress relaxation and non-proportional cyclic hardening.

Before delving further into explanations about the plasticity models mentioned above, two important concepts used in plasticity models must be explained: the Yield surface and the Ramberg-Osgood Model.

5.3.1
Yield Surface

The equation most commonly used to describe the yield surface F for various types of steel is based on the von Mises criterion, as presented in equation (5.4):

$$F = \frac{1}{2}\left[\left(\sigma_x - \sigma_y\right)^2 + (\sigma_x - \sigma_z)^2 + \left(\sigma_y - \sigma_z\right)^2 + 6\left({\tau_{xy}}^2 + {\tau_{xy}}^2 + {\tau_{xy}}^2\right)\right] - S_y = 0 \quad (5.4)$$

where S_y is the yield stress. For a plane stress, the yield surface is given by:

$$F = {\sigma_x}^2 + 3{\tau_{xy}}^2 - {S_y}^2 = 0 \quad (5.5)$$

It is important to note that the yield stress must be defined as the limit where a transition between the elastic and elasto-plastic behaviors of the material occurs. This stress limit can be defined as the stress that causes plastic strain greater than, say, 0.001% or any other reasonably small value. The traditional yield strength definition calls for a plastic strain of 0.2%, which is a very large value when accurate elasto-plastic analyses are required.

A simplification is obtained by assuming that all the stress components are equal to zero except components σ_x and τ_{xy}. In this case, the yield surface turns out to be a circumference on a $\sigma_x \, x \, \sqrt{3}\tau_{xy}$ plot, centered at (0,0) and with a S_y radius.

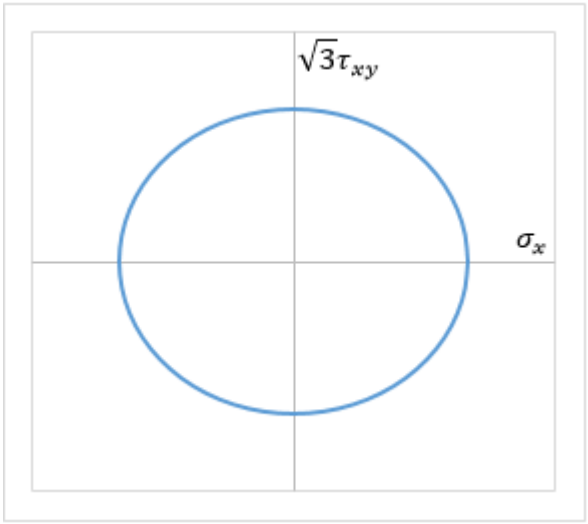

Figure 5.2: Illustration of the yield surface.

In Figure 5.2, every point inside the circumference is considered to be under elastic loading and every point outside the circumference is considered to be under plastic loading.

5.3.2

Ramberg-Osgood Model

The Ramberg-Osgood model [4, 31] establishes the stress-strain relationship under elasto-plastic conditions. Some modifications, to be presented later in this chapter, are necessary to describe a proper stress-strain relationship in the case of non-proportional loading.

The Ramberg-Osgood equation separates the entire strain into two different parts. One is the elastic part, where stress and elastic strains are related using the elasticity modulus. The plastic part is modeled in an exponential form using the Ramberg-Osgood parameters, K_m, the hardening coefficient, and n_m, the hardening exponent.

$$\varepsilon = \varepsilon_{el} + \varepsilon_{pl} = \frac{\sigma}{E} + \left(\frac{\sigma}{K_m}\right)^{\frac{1}{n_m}} \tag{5.6}$$

It is possible to get the values of the material parameters needed for the Ramberg-Osgood equation by best fitting the experimental results from a regular tensile test.

However, this model only represents the monotonic curve, which is determined using the $\sigma\ x\ \varepsilon$ curve obtained from the regular tensile test (specimen subjected to one axial loading). When the specimen is under reversed loading unloading, the stabilized cyclic deformation is also represented by the Ramberg-Osgood equation:

$$\Delta\varepsilon = \frac{\Delta\sigma}{2} + 2\left(\frac{\Delta\sigma}{2K'}\right)^{\frac{1}{n'}} \tag{5.7}$$

where $\Delta\varepsilon$ is the strain range, $\Delta\sigma$ is the stress range amplitude, K' is the cyclic hardening coefficient, and n' is the cyclic hardening exponent. The cyclic Ramberg-Osgood parameters are obtained by using the $\sigma\ x\ \varepsilon$ cyclic curve. It is not unusual in fatigue analysis to assume K_m and n_m as equal to K' and n', respectively, when the formers' cyclic parameters are unknown. For a proper calculation, the hysteresis loop equation (5.7) must be used, as in **Figure 5.3**.

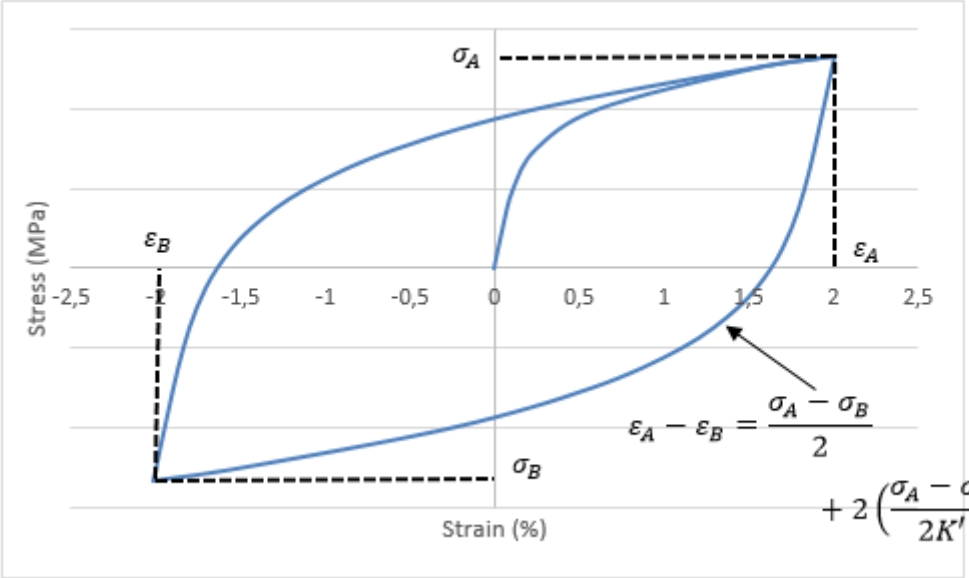

Figure 5.3: Example of the Ramberg-Osgood Curve.

5.3.3
Isotropic Hardening

Isotropic hardening is demonstrated by the isotropic change in the size of the yield surface. Hardening can be quantitatively represented by the increase in the stress limit required to cause a previously defined increase in plasticity. In other words, hardening means that an increase in the applied stress is required to cause an increase in the plastic strain.

This phenomenon is better explained by an example where a specimen is loaded and unloaded in a simple tensile test. **Figure 5.4** shows a specimen that is stressed until point 1 is reached, which is a point higher than a previously defined elasto-plastic limit (for example defined as the point where the plastic strain reaches, say, 0.001% or 0.2%). After unloading to zero and reloading the specimen, the new elasto-plastic limit becomes σ_1.

If the specimen continues to be loaded until it reaches point 2 and is then unloaded under compression, compressive plastic strain will start after point 3 ($\sigma_3 = -\sigma_2$) is reached. The generalization of a constant hardening, despite the previous proportionality of the pair of stresses (σ_x, τ_{xy}) that caused the increase in elasto-plastic stress limit, is described by the isotropic hardening phenomenon.

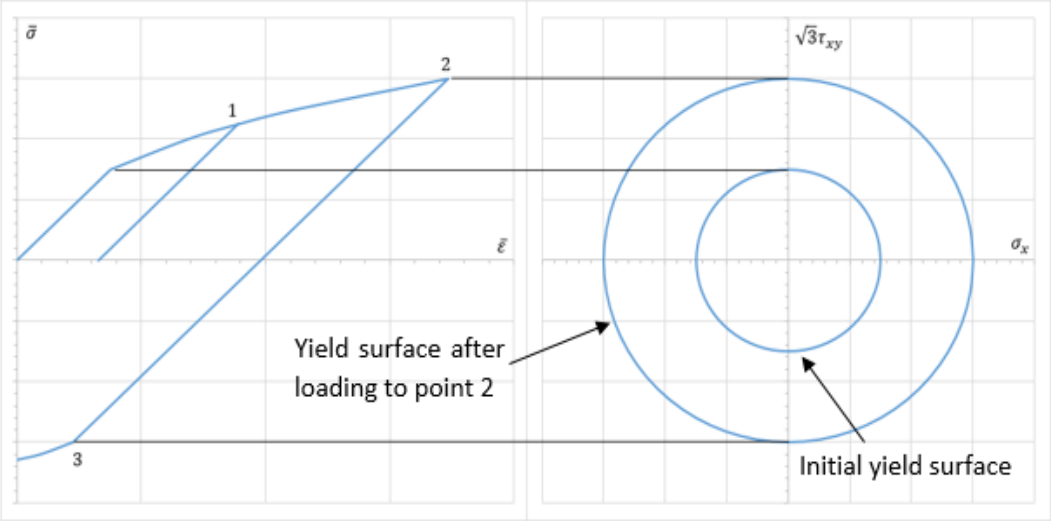

Figure 5.4: Illustration of the Isotropic Hardening phenomenon.

5.3.4

Kinematic Hardening

The kinematic hardening model is represented by the yield surface that translates but does not change the size or the shape. Using the previous example and observing **Figure 5.5**, one can see that the process of loading, unloading and reloading only produces the translation of the yield. The displacement of the yield surface is represented by vector α_B in **Figure 5.5**, but there is no growth of the yield surface, as occurred during isotropic hardening.

The difference between the two phenomena appears in the next part of the example. When the specimen continues to be loaded until it reaches point 2, and the yield surface is dislocated again farther from the origin, the unload to point 3' gives a yield stress in compression ($\sigma_3, = \sigma_2 - 2\sigma_y$) that is smaller than the same parameter for isotropic hardening (point 3 in **Figure 5.4**).

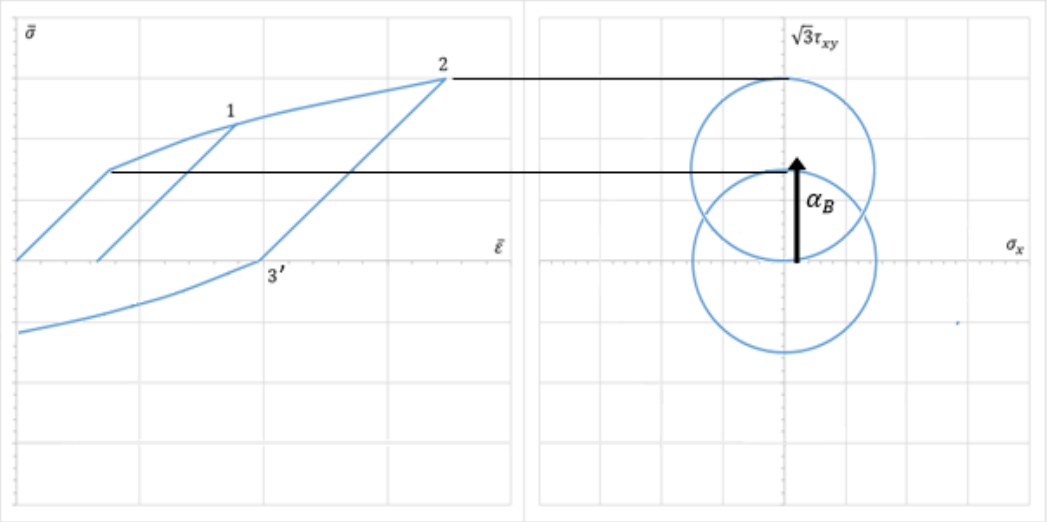

Figure 5.5: Illustration of the Kinematic Hardening phenomenon.

When a piece of material is subjected to cyclic deformation, the material will exhibit both isotropic and kinematic hardening behavior in the first cycles, and after a certain number of cycles, the material starts a phase described as cyclically stable. In that phase, the material displays only the kinematic hardening behavior. In general, when a fatigue assessment is being performed, the material is assumed to already be in a cyclically stable condition[9]; therefore, for cyclically-stabilized materials, only the kinematic has to be input to describe the material's behavior.

5.3.5

Non-proportional Cyclic Hardening

Figure 5.6 is the figure used most in the literature to exemplify this phenomenon. It shows results for tension and torsional strain controlled tests on a cylindrical bar. Both in-phase and 90 degrees out-of-phase data were obtained using sinusoidal waveforms to generate the normal and shear strains. When the cyclic deformation becomes stable, the amplitude of the equivalent stress is determined from the imposed strain amplitude.

[9] This assumption is due to the fact that only in the first cycles of deformation can the behavior of the material be described as non-stable [4, 27]. Since in fatigue analysis the material is subjected to a large number of cycles, the consideration of presenting an isotropic hardening behavior in the initial cycles has little impact on the final result.

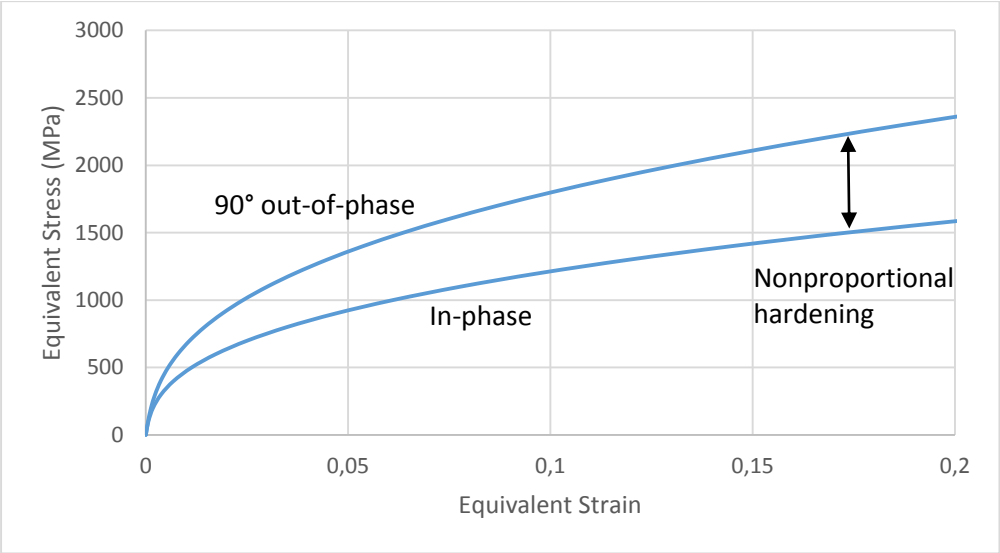

Figure 5.6: Illustration of the Non-proportional Cyclic Hardening phenomenon.

A phase difference between the strains is created in a non-proportional loading situation (when the direction of the principal strain changes during the strain history). One can see in the figure that there is a difference between the two curves, with the 90° out-of-phase curve presenting higher values of equivalent stress for the same values of equivalent strain. This characteristic is caused by the non-proportional cyclic hardening phenomenon.

Quantification of the non-proportional cyclic hardening phenomenon is made by changing the value of the cyclic hardening coefficient (K) in the Ramberg-Osgood model (exponent n is the same for proportional and non-proportional histories). The change in K is accomplished using the following equation:

$$K' = K(1 + \Phi \cdot F_{NP}) \tag{5.8}$$

where K' is the non-proportional cyclic hardening coefficient, Φ is a material property, and F_{NP} is the factor of non-proportionality for a given load. [4, 10]

The non-proportionality factor is measured by means of three steps: first, the entire load history is drawn in a $\varepsilon \; x \; \gamma/\sqrt{3}$ diagram; then, the complete load path in the diagram is circumscribed by an ellipse, with the minor axis of the ellipse denoted as b and the major axis as a; lastly, the value of the factor is equal to ratio b/a. An illustration of how to evaluate the factor is shown in **Figure 5.7**.

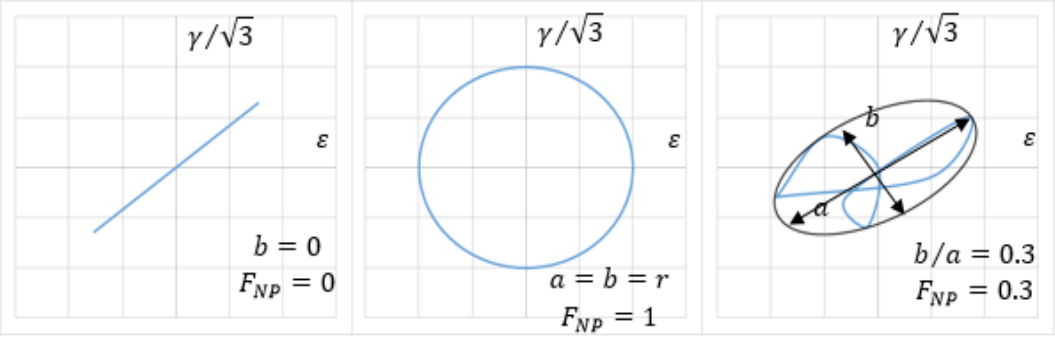

Figure 5.7: Illustration of the quantification of the non-proportional factor.

The material property Φ can be obtained using the results of the tests that generate the two curves plotted in **Figure 5.6.** The value of K is determined by fitting the in-phase curve in the chart using the Ramberg-Osgood equation, while the value of K' is obtained by fitting the 90° out-of-phase curve. Because the value of F_{NP} is 1.0 for the 90° out-of-phase loading, the value of Φ is calculated from equation (5.8).

Typical values for Φ are shown in [4] and can vary from 1.0 for materials that develop a large amount of non-proportional hardening, such as 316 and 304 stainless steel, to 0.0 for materials that do not develop any significant non-proportional hardening effects, such as Al 7075 and Al 1100.

5.3.6

Mean Stress Relaxation and Ratcheting or Cyclic Creep

The cyclic creep or ratcheting phenomenon can be explained using the following example. Consider a bar with one end fixed (without displacement or rotation) and with a weight connected to the other end, creating static axial stress. The end with the weight is then subjected to cyclic angular displacement, in such a way that a controlled cycle shear strain is produced.

If both loadings produce only an elastic scenario, or if the ratcheting phenomenon is not observed, the results of the loading conditions are easy to estimate. The static axial stress will impose a static axial strain, whereas the angular displacement cycles will result in a constant range of shear strain, since the shear strain is controlled.

This is not the case when loading results in plastic behavior and when ratcheting is observed. In such cases, the static axial stress will generate an initial axial strain. However, for each cycle of shear strain, not only a range of shear strain

is observed, but also an increase in the axial strain value. This increase is caused by the ratcheting phenomenon, and it is characterized by the growth of the plastic deformation in material subjected to cyclic strain loading associated with mean stress.

The same phenomenon is observed if the bar is subjected to both static shear stress and cyclic axial strain. It is important to point out the fact that the rate of the ratcheting effect can increase with the number of cyclic loadings, or it can decrease (eventually making the maximum strain stable) after a certain number of loading cycles. This rate depends on the material's properties and on the amount of plasticity observed in it.

Mean stress relaxation is similar to the ratcheting phenomenon. It can be observed during a cyclic strain controlled test where a mean stress is present. The $\sigma\ x\ \varepsilon$ curve in such cases will present the same strain ranges, but the mean stress value will tend towards zero for each strain cycle. That is what the mean stress relaxation means. The mean stress relaxation rate will depend on the initial mean stress value and the plastic strain range.

Because none of the models in the current literature [10] evaluate such phenomena accurately, the modeling of the plasticity characteristics described in this subchapter is still matter for research.

5.4
Models for the Plastic Stress-Strain Relationship

This subchapter describes some of the models that establish a relationship between stress and strain with the presence of cyclic plastic deformation. Although this description is made considering non-proportional histories, these methods can also be implemented for proportional load histories.

Before proceeding any further with presenting the models, it is important to point out a couple of points. The first one is that the methods presented here do not consider the change of material properties caused by variations in temperature. Models that evaluate these changes are more complicated and are beyond the scope of those presented here (see [32] for additional information).

The second point is that such models can only be used if the strain values are known. In cases where stresses are calculated, the plasticity model must be

included in the stress analysis, [33], or an elastic-plastic finite element solution must be implemented.

5.4.1

Kanazawa Method

Kanazawa proposed a method [34] that uses two concepts previously explained in this chapter. The model applies the non-proportional cyclic hardening coefficient (K') calculated in equation (5.8) in the Ramberg-Osgood equation. Consequently, the stress-strain relation is given by the following equation:

$$\frac{\Delta\sigma_{eq}}{2} = K' \left(\frac{\Delta\varepsilon_{eqpl}}{2}\right)^{n} \tag{5.9}$$

where $\Delta\sigma_{eq}$ and $\Delta\varepsilon_{eqpl}$ are the equivalent ranges of stress and plastic strain, respectively. If the strain value is not separated into plastic and elastic components, the stress value can be obtained by numerically solving the equation:

$$\Delta\varepsilon_{eq} = \frac{\Delta\sigma_{eq}}{2} + 2\left(\frac{\Delta\sigma_{eq}}{2K'}\right)^{\frac{1}{n}} \tag{5.10}$$

This is the Ramberg-Osgood equation, which uses the equivalent strain and stress and the value of the non-proportional cyclic hardening coefficient instead of the proportional cyclic hardening coefficient. The strain range can also be obtained by a given stress range value using equation (5.10) directly.

Reference [4] proposes using equation (5.10) in a critical plane approach. In doing so, the strain range that is normal to a plane ($\Delta\varepsilon_{\perp}$) can be related to the range of stress that is normal to a plane ($\Delta\sigma_{\perp}$), and vice versa, in the same way as explained previously. Hence, parameter $\sigma_{\perp max}$ required in the Fatemi-Socie and SWT models is obtained for a given strain history.

One can see that this model is very simple; however, reference [35] shows that it can lead to predictions of stress values 40% higher than the experimental values. A problem with this model arises, for example, if two different loading paths are considered, both having the same amplitudes in shear and axial strain, but with different formats in the $\varepsilon\ x\ \gamma/\sqrt{3}$ diagram. It is possible that, in using this model, the two different loading paths will result in the same non-proportional cyclic hardening coefficient, since this value is defined by the semi-axis of an ellipse that has circumscribed the load path, as shown in **Figure 5.8**.

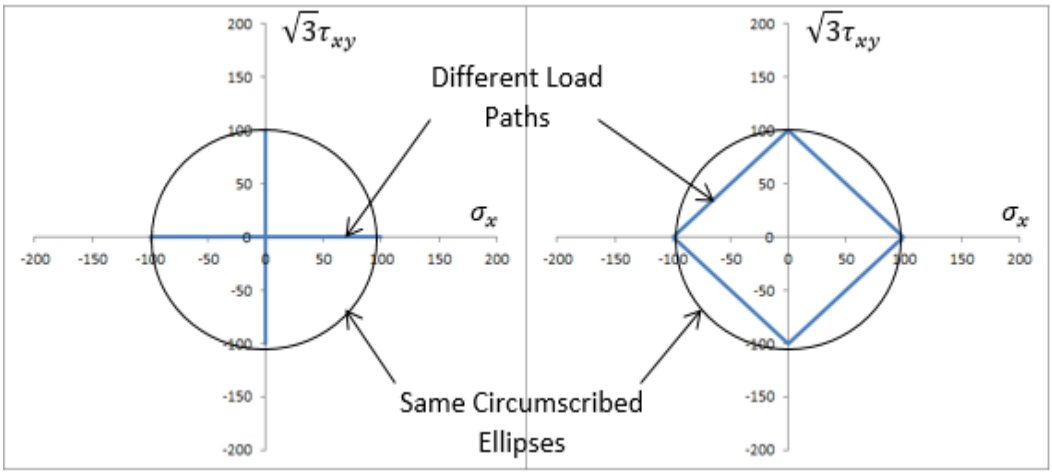

Figure 5.8: Example where the same ellipse can circumscribe two different load paths.

Another model (the Jiang and Sehitoglu using Tanaka's non-proportionality model) yields better predictions. In order to present this model, for a better understanding, the Flow Rule and the Mróz model will be presented first.

5.4.2
Flow Rule

A Flow Rule is a constitutive equation that describes the relationship between increments of stress and plastic strain. To apply this rule, the total strain must be separated into the plastic and elastic parts, with the calculation of the elastic part being performed by using Hooke's law.

Flow rules are usually supported by the concept proposed by Drucker [36], which states that the vector of incremental plasticity strain is normal to the yield surface during plastic deformation. This concept can be expressed by the following equation, the flow rule formula:

$$d\varepsilon_{ij}^{p} = \frac{1}{C}\frac{\partial F}{\partial \sigma_{ij}}\frac{\frac{\partial F}{\partial \sigma_{kl}}d\sigma_{kl}}{\frac{\partial F}{\partial \sigma_{mn}}\frac{\partial F}{\partial \sigma_{mn}}} \tag{5.11}$$

where $d\varepsilon_{ij}^{p}$ is the vector of incremental plasticity strain, F is the yield surface function, and the material property C is the strain hardening coefficient.

5.4.3
Mróz Model

Mróz proposed a model [37] that consists of a description of the stress-strain relationship using a series of yield surfaces. The first step of this model is to define the number of yield surfaces to be used. This number, included in the model, defines the accuracy of the resulting stress-strain relationship. A larger number of yield surfaces implies better accuracy, but more time is consumed in obtaining the final result.

The yield surfaces can be obtained using the $\sigma\ x\ \varepsilon$ curve (**Figure 5.9**), which is the result of an experimental test, or is defined based on the Ramberg-Osgood parameters.

Two parameters have to be selected before calculating the yield surfaces: S_y, which is the material's yield stress, and σ_{max}, which is the parameter defined by the user, and equal to the maximum equivalent stress that the model can evaluate. If, for example, this value is 500 MPa, any larger stress value cannot be evaluated unless σ_{max} is changed to a higher value.

The number of yield surfaces (M) defines the number of divisions between the values of σ_{max} and S_y. The range formed between those values is split into levels of stress σ_l (**Figure 5.9**), which can be defined using the following equation:

$$\sigma_l = S_y + (l-1)\left(\frac{\sigma_{max}-S_y}{M-1}\right),\ \ l = 1,2,3,\dots,M \tag{5.12}$$

The yield surfaces are obtained by replacing the value of S_y with σ_l, respective to each yield surface, using equation (5.4). For a better visualization of this calculation, see **Figure 5.8**. The yield surfaces assumed that only the stresses σ_x and τ_{xy} are present. Thus, one can see that the yield surfaces become circles centered on the origin of the $\sigma_x\ x\ \sqrt{3}\tau_{xy}$ diagram.

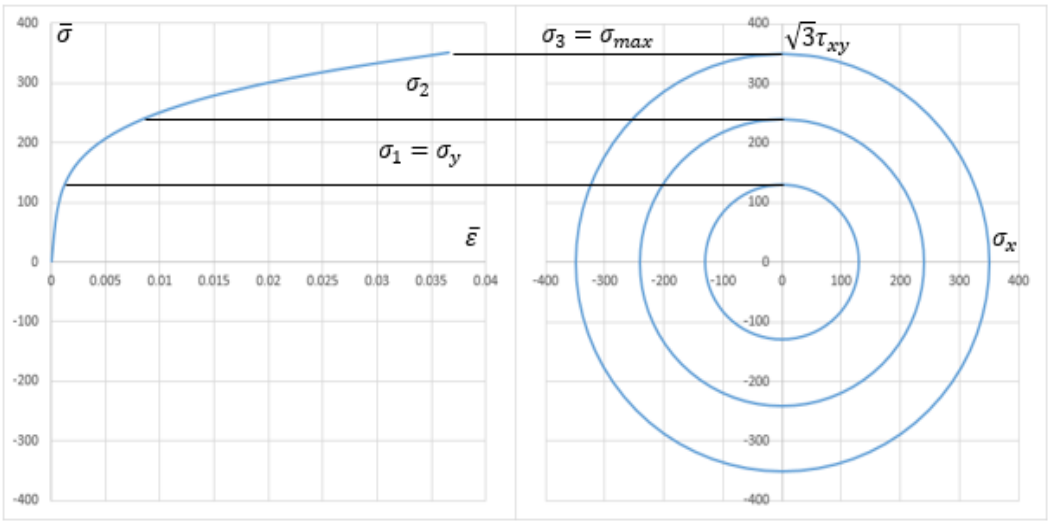

Figure 5.9: Illustration of the calculation of the yield surfaces with M = 3**.**

Evaluating the stess-strain relationship is made by translation (but not changing the format) of the yield surfaces and using the flow rule equation (5.11). The constant C required in equation (5.11) is defined for each region between two yield surfaces, and calculating these constants can be done using the following equation:

$$C_n = \left\{\frac{3}{2}\cdot\left[\left(\frac{\varepsilon_{n+1}-\varepsilon_n}{\sigma_{n+1}-\sigma_n}\right)-\frac{1}{E}\right]\right\}^{-1},\quad n = 1,2,3,\dots,M-1 \tag{5.13}$$

The translation of the yield surfaces its better explained by using **Figure 5.10**.

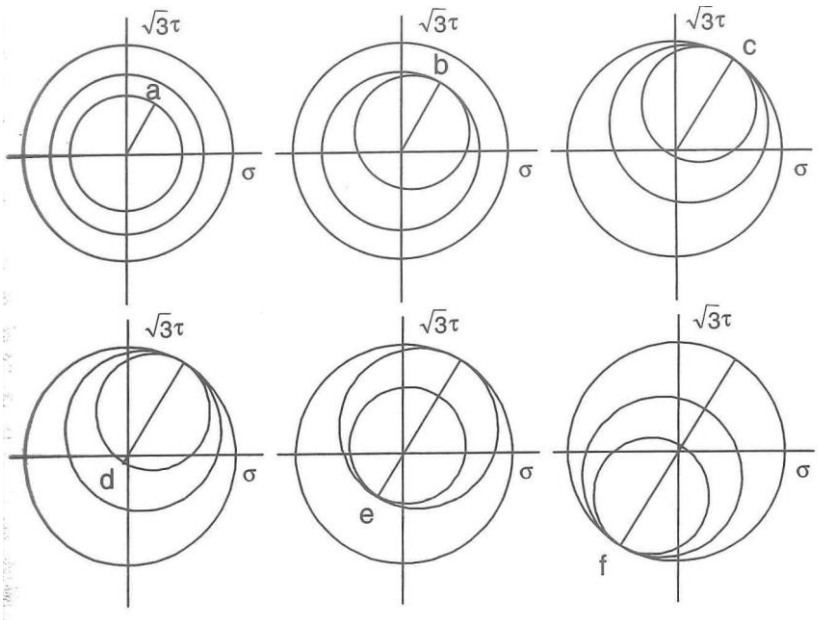

Figure 5.10: Translation of the yield surfaces [10].

Because the loads at point a are elastic, the stress-strain relationship can be evaluated using Hooke's law. Beyond point a, the smallest yield surface starts to be translated and the loading begins to cause a part of plasticity behavior. That part can be evaluated using the flow rule, with the coefficient related to the region between the smallest and the middle-sized yield surfaces.

The smallest yield surface continues to be translated until it touches point b. At that moment, both smallest and middle-sized surfaces are translated together, and the flow rule will now use the coefficient related to the region between the middle-sized and largest yield surfaces, until it touches point c. After reaching point c, unloading occurs to point d. At this moment, there is no plastic deformation because unloading occurs inside the smallest circle, and the stress-strain relationship is established by Hooke's law.

With the loading path history continuing to point e, the smallest yield surface is moved again, and the constant used in the flow rule is the one related to the region between the smallest and middle-sized yield surface. The compression loading continues making both smallest and middle-sized yield surfaces move together, and the constant for the region between the middle-sized and largest yield surfaces is adopted according to the flow rule.

Finally, the loading touches point f and the procedure is repeated cyclically from point c to point f. The resulting $\sigma_{eq}\, x\, \varepsilon_{eq}$ curve based on this model is presented in **Figure 5.11**.

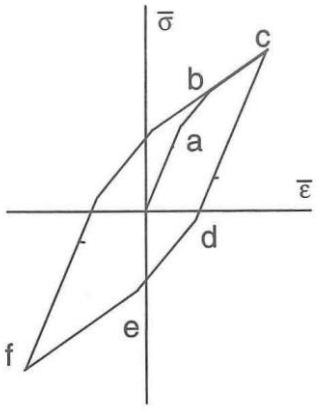

Figure 5.11: The stress-strain relationship when the load history is the one in **Figure 5.10** [10].

One can see that the resulting curve has a hysteresis loop format, which is to be expected under such loading conditions. This model can be better visualized using the application presented in [38], in which the creation of the yield surfaces using the Ramberg-Osgood parameters, the movement of the yield surface and

the resulting $\sigma_{eq}\ x\ \varepsilon_{eq}$ curve while loading is applied are all presented. The yield surface movement calculation used in this application is based on the Garud [40] model.

Even with the resulting $\sigma_{eq}\ x\ \varepsilon_{eq}$ curve being the one expected, this method has one disadvantage: it does not do a good job at predicting the ratcheting effect. That is why the Jiang and Sehitoglu model using Tanaka's non-proportionality model is presented below and employed herein.

5.4.4

Jiang and Sehitoglu using Tanaka's Non-proportionality Model

The method [41 to 48] requires calculating the deviatoric stresses using:

$$S_x = \sigma_x - \frac{1}{3}\sigma_h,\ S_y = \sigma_y - \frac{1}{3}\sigma_h,\ S_z = \sigma_z - \frac{1}{3}\sigma_h,\ S_{xy} = \sigma_{xy},\ S_{xz} = \sigma_{xz},\ S_{yz} = \sigma_{yz} \tag{5.14}$$

where:

$$\sigma_h = \frac{\sigma_x+\sigma_y+\sigma_z}{3} \tag{5.15}$$

The yield surface is defined as:

$$F = \left(\underline{S} - \underline{\alpha}\right):\left(\underline{S} - \underline{\alpha}\right) - 2k^2 = 0 \tag{5.16}$$

where $\underline{S}$ is the deviatoric stress tensor, $\underline{\alpha}$ is the total backstress tensor, which represents the location of the center point of the yield surface, k is the yield shear stress ($k = S_y/\sqrt{3}$) and the ":" operator represents the inner product. The flow rule proposed for this model is simplified with:

$$d\underline{\varepsilon}^p = \frac{1}{h}\langle d\underline{S}:\underline{n}\rangle\underline{n} \tag{5.17}$$

where $\langle\ \ \rangle$ is defined as the MacCauley bracket (if the value inside the bracket is negative, the result of the operation is zero, and if the value is positive the result is the value between the brackets), $d\underline{\varepsilon}^p$ is the incremental plastic strain tensor, $d\underline{S}$ is the incremental stress tensor in a deviatoric space, h is the plastic modulus, and $\underline{n}$ is the unit tensor that is normal to the exterior of the yield surface located at the loading point. This tensor can be calculated with:

$$\underline{n} = \frac{\underline{S}-\underline{\alpha}}{|\underline{S}-\underline{\alpha}|} \tag{5.18}$$

The concept used in this mode is the same as the one presented by Chaboche [42 to 44], who proposed that the total backstress tensor can be split into M parts, with the relationship between the total and the parts being described as:

$$\underline{\alpha} = \sum_{i=1}^{M} \underline{\alpha}^i \tag{5.19}$$

This representation is similar to the idea shown in the Mróz model, in that the splitting of the backstress tensor is close to the idea of several yield surfaces. The modeling of the split backstress tensors can be done with the definition of parameters c^i and r^i in equation (5.20), which can be calculated using the Ramberg-Osgood parameters, as shown in [46, 49], in a way similar to the Mróz model.

The translation due to the loading of the parts of the total backstress tensor is calculated using the following equation:

$$d\underline{\alpha}^i = c^i r^i \left[\underline{n} - \left(\frac{|\alpha^i|}{r^i} \right)^{\chi^i + 1} \underline{L}^i \right] dp \tag{5.20}$$

where c^i and r^i are material properties calculated using the Ramberg-Osgood equation (see [46, 49]), dp is the equivalent plastic strain, and χ^i is a material property responsible for controlling the ratcheting rate. In cases where steady state response is under analysis, the value of this constant is not important and, as shown in [35], if it is assumed to be 10, the model will predict adequate behavior of several materials and different loading conditions.

The following definitions are also required for the use of equation (5.20):

$$\underline{L}^i = \frac{\underline{\alpha}^i}{\left|\underline{\alpha}^i\right|}, \qquad i = 1,2,3,\dots,M$$

$$\left|\underline{\alpha}^i\right| = \sqrt{\underline{\alpha}^i : \underline{\alpha}^i}, \; i = 1,2,3,\dots,M \tag{5.21}$$

$$dp = \sqrt{d\underline{\varepsilon}^p : d\underline{\varepsilon}^p}$$

The translation of the parts of the total backstress ($d\underline{\alpha}_i$) is often called the evolution of the backstress, and was proposed by Jiang [45], who showed that the plastic modulus h can be calculated using equation (5.22), where this equation already considers the consistency condition. The consistency condition implies that the deviatoric stress tensor must be inside the yield surface during plastic deformation.

$$h = \sum_{i=1}^{M} c^i r^i \left[1 - \left(\frac{|\underline{\alpha}^i|}{r^i}\right)^{\chi^i+1} \underline{L}^i : \underline{n}\right] + \sqrt{2}\frac{dk}{dp} \tag{5.22}$$

The non-proportional effects are included in the model by changing the value of r^i and the evolution of dk. The evolution of these values is obtained using a non-proportional parameter that is defined as a fourth rank $\underline{C}$ as proposed by Tanaka [48]. The evolution of this tensor can be evaluated by:

$$d\underline{C}_{ijkl} = c\left(\underline{n}_{ij}\underline{n}_{kl} - \underline{C}_{ijkl}\right)dp \tag{5.23}$$

Initially, Tanaka's non-proportional tensor values ($\underline{C}$) are all equal to zero and as the loadings are applied, the values change using the above equation. Tensors $\underline{n}_{ij}$ and $\underline{n}_{kl}$ in equation (5.23) are the tensors defined in equation (5.18). The non-proportional parameter is obtained with the following equation:

$$A = \sqrt{1 - \frac{\underline{n}_{pq}\underline{C}_{ttpq}\underline{C}_{ttrs}\underline{n}_{rs}}{\underline{C}_{ijkl}\underline{C}_{ijkl}}} \tag{5.24}$$

The sub-index syntax operations used in equations (5.23) and (5.24) apply the tensor calculus concepts. The change in the value of r^i and the evolution of dk are evaluated with:

$$dk = \beta[k_o(1 + \Phi A) - k]dp \tag{5.25}$$

$$dr^i = \beta\left[r_o^i(1 + \Phi A) - r^i\right]dp \tag{5.26}$$

where k_o and r_o^i are the initial values of k and r^i, respectively, and β is the material parameter that controls the rate of non-proportional hardening. Reference [35] shows that if the value of β is set at 5, the model will predict an adequate relationship for several materials and different loading conditions if the steady state (cyclically stable) behavior is being modeled. The parameter Φ is the same one presented in subchapter 5.3.5 in the explanation of equation (5.8).

Reference [35] also shows that predictions using this model perform better than using the Kanazawa method. In the worst case, the Kanazawa method predicts values 40% higher than the measured values, and the Jiang and Sehitoglu model using Tanaka's non-proportionality model predicts values 12% higher than the measured values. For this reason, the latter method is the one applied in this thesis.

6

Case Studies

6.1

Introduction

Two fatigue analysis cases are presented in this chapter. The first uses the stress history calculated in Chapter 2; the second uses the experimental results of tests presented in [15]. During the presentation of both case studies, the methods described in the previous chapters are explained in such a way that the entire fatigue analysis methodology presented in this thesis may be well understood. In addition, some adaptations that were necessary are also presented and explained in more detail.

Figures 6.1 and **6.2** show the combination of the cycle counting methods and the damage models implemented in the software programs used for case studies one and two respectively.

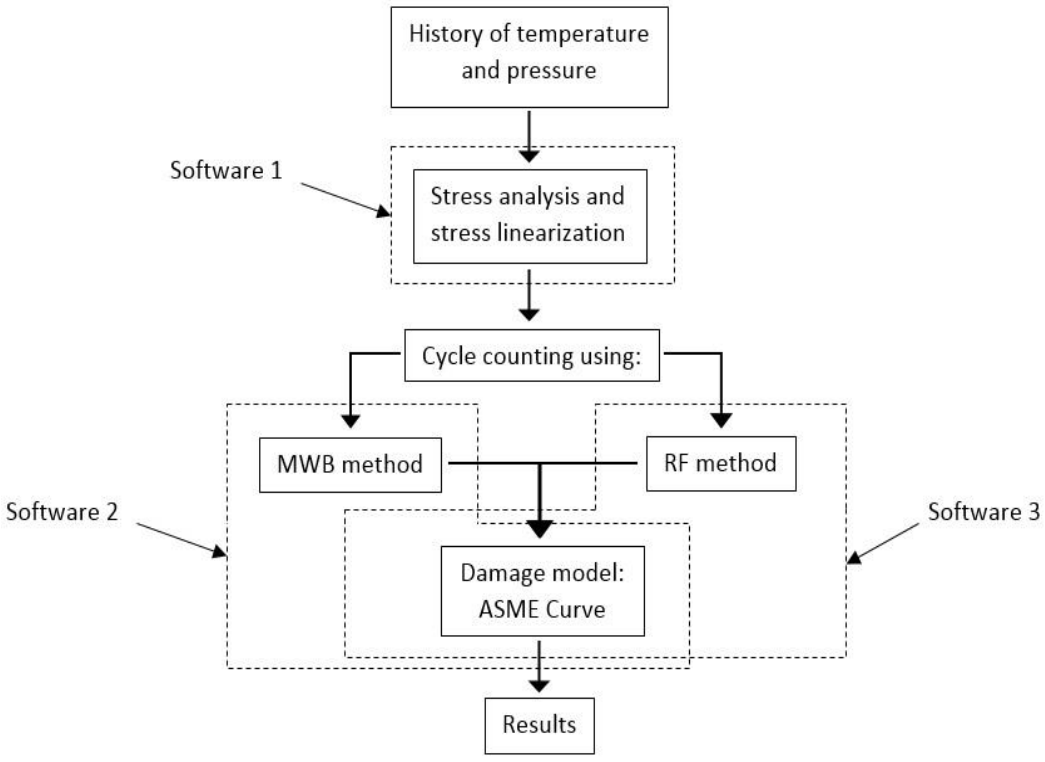

Figure 6.1: Use of the three software programs employed in the first case study.

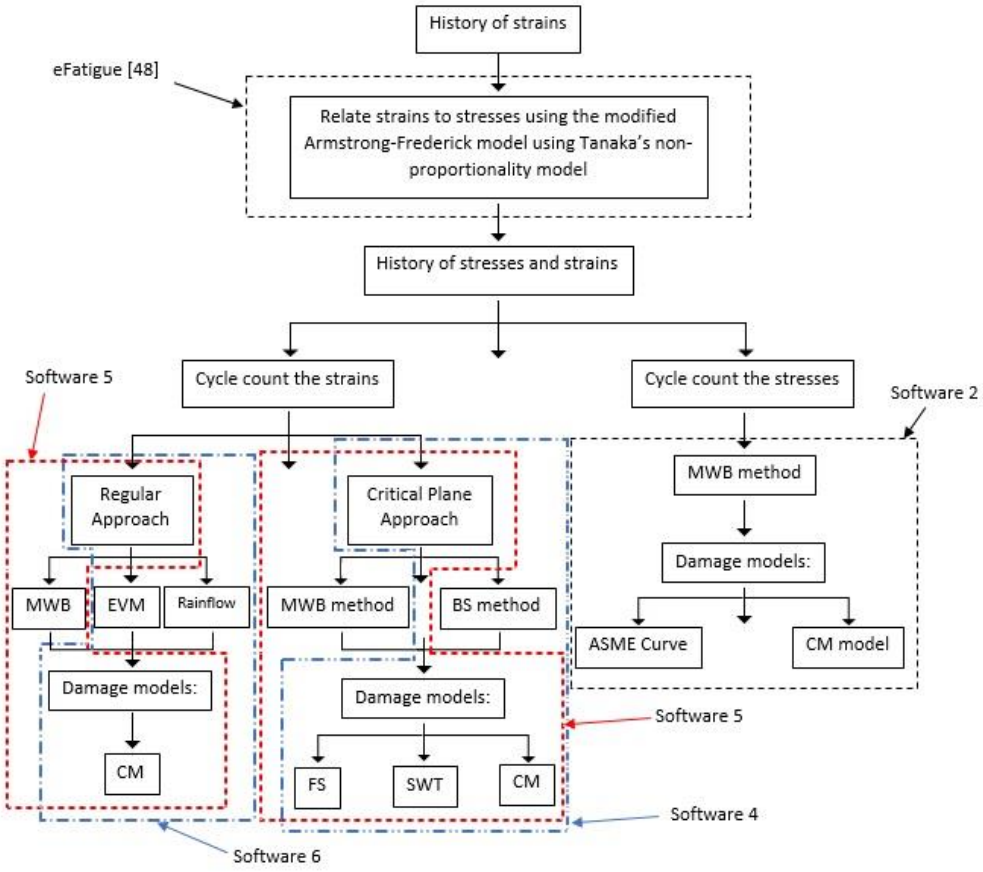

Figure 6.2: Use of the four software programs employed (without considering the eFatigue) in the second case study.

6.2

First Case Study

The first case study is performed using the time history of stresses calculated in Chapter 2. The primary objective of this case study is to compare the cycle counting method in **Figure 4.22** (Modified Wang-Brown) with the Rainflow method. Since the stress history is non-proportional, the modification of the Rainflow method explained in subchapter 4.3 is adopted.

The model used for evaluating the damage caused by this history is the one in the ASME Code for elastic stress analysis (explained in subchapter 3.3.1). Since this method does not use half cycles to evaluate damage, the Simplified Rainflow method was selected (subchapter 4.4).

Figures 6.3 to **6.5** show the linearized and peak stress components calculated in Chapter 2.

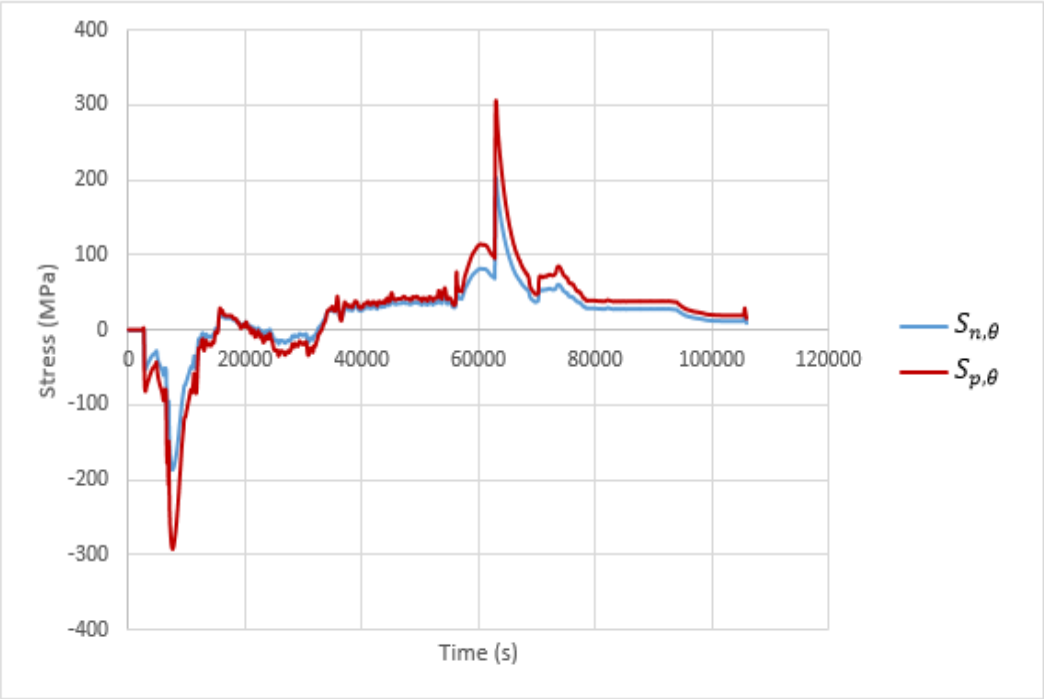

Figure 6.3: History of the circumferential stresses caused by the thermal plus mechanical loads.

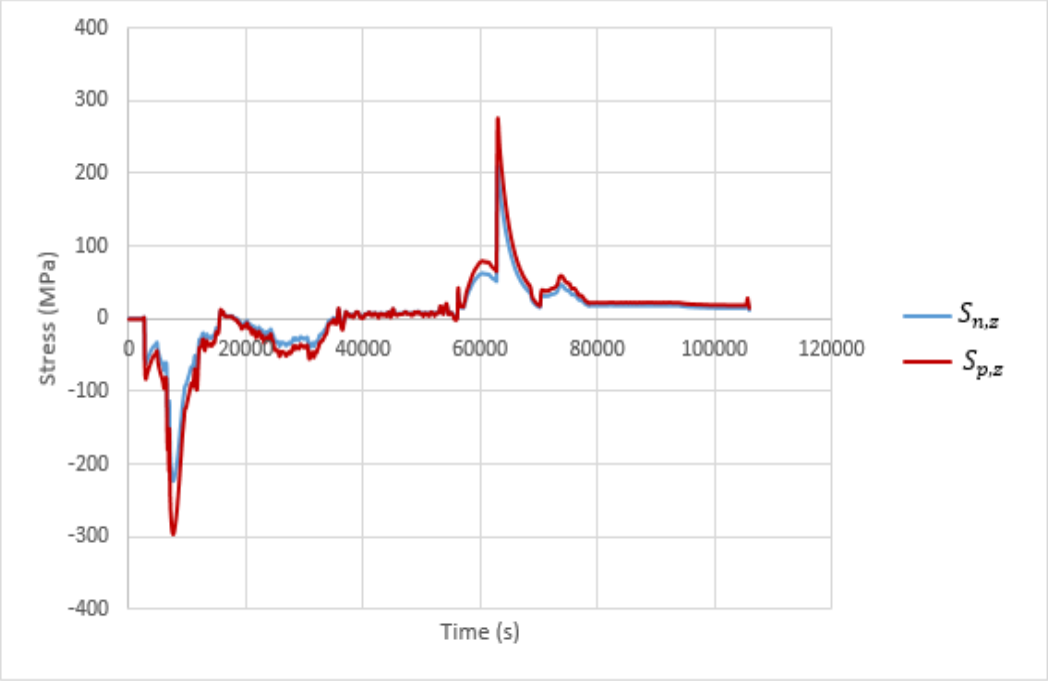

Figure 6.4: History of the longitudinal stresses caused by the thermal plus mechanical loads.

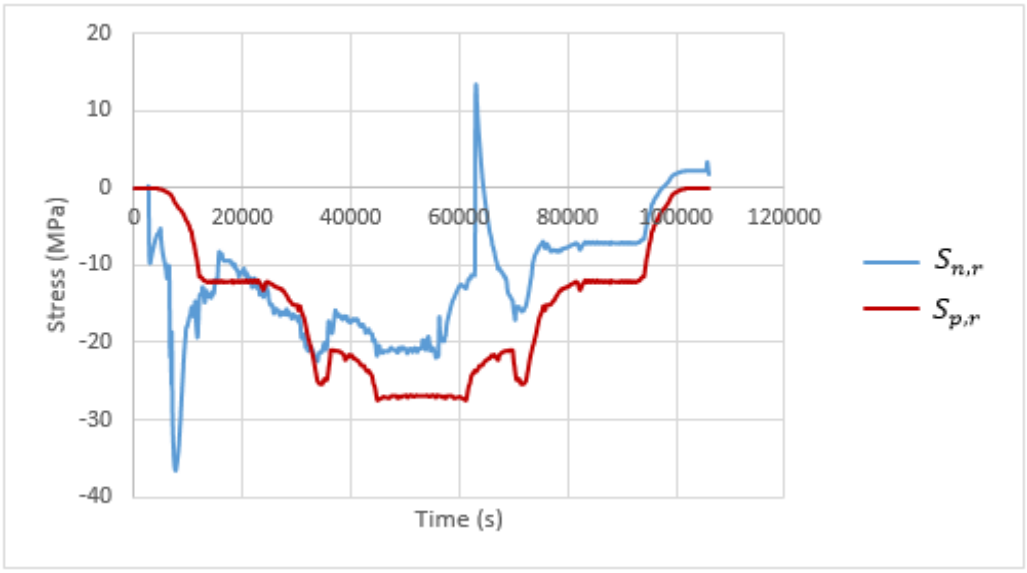

Figure 6.5: History of the radial stresses caused by the thermal plus mechanical loads.

A phenomenon that occurs when the linearized stresses are used in a fatigue analysis is that sometimes the peak (or valley) of the stress components of tensors S_p and S_n do not take place at the same time step. In the ASME Code the alternating stress (which is the parameter for entering the fatigue curve) is a function of the values of K_e and the range of S_p (formed using one cycle counting method) as shown in equation (3.13), where K_e is a function of the range of S_n and of the material properties, as shown in equation (3.14).

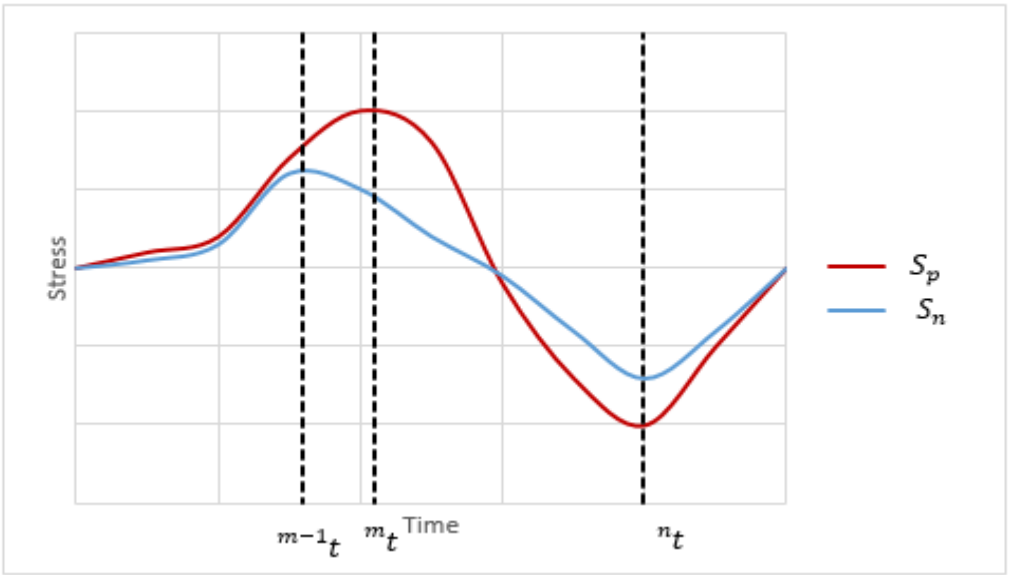

Figure 6.6: Schematic example of a time history of linearized stresses.

To form the stress ranges, the cycle counting is done using the S_p stresses, and the S_n ranges are formed using the same time steps that formed the S_p ranges.

In that way, if a cycle counting routine returns the S_p range using time steps ${}^{m}t$ and ${}^{n}t$, the S_n range is formed using time steps ${}^{m}t$ and ${}^{n}t$.

However, this leads to a problem, as can be observed in **Figure 6.6.** The cycle counting performed along the S_p history will return its range for time steps ${}^{m}t$ and ${}^{n}t$ while, on the other hand, the highest value of ΔS_n occurs for time steps ${}^{m-1}t$ and ${}^{n}t$.

If time step ${}^{m-1}t$ is selected instead of time step ${}^{m}t$ to calculate the ranges, it is possible that the alternating stress value (which is the final value of interest) will be higher, even if the ΔS_p is lower. The S_n range in this case will show a larger value, which will increase the value of the alternating stress (see equations (3.13) and (3.14)).

In conclusion, performing the cycle counting using the history of S_p stresses may result in a non-conservative fatigue analysis. In order to avoid that situation, the highest value of the alternating stress must be found in the cycle counting method. As explained in Chapter 2, this is one of the reasons that the entire history of the linearized stresses has to be calculated and not just its values at the time step where the maximum range of stress S_p range is formed.

To ensure that the highest value of alternating stress is found, a number of methods have been proposed. One is studied in [23], which assumes that the alternating stress value to be considered must be located between the time intervals where the S_n and S_p peaks occur. Even though this is a good assumption, another, simpler method was the one chosen for this thesis. This simple method is explained and developed in more detail in the following paragraphs.

This method was initially proposed for use with the Rainflow cycle counting method. It consists in, after the cycle counting is performed, combining the time steps - close to the time steps that have been counted – that will generate the largest alternating stress. Since the cycle counting procedure is implemented using a software program, the number of time steps in the search to be considered before and after the time step counted along the routine application (the so-called rubber band) is one of the input parameters that must be given by the user. **Figure 6.7** presents a better visualization of this search.

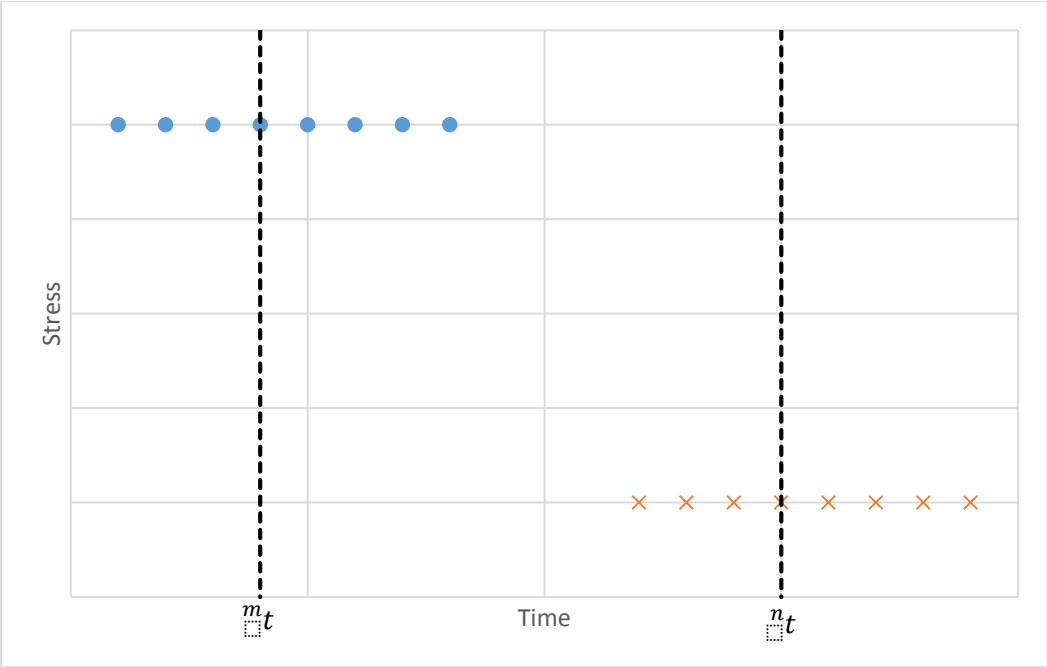

Figure 6.7: Example of the search for the highest alternating stress.

In **Figure 6.7** the dashed lines represent the time steps counted using the Rainflow routine, where ^{m}t represents the peak and ^{n}t the valley. The three points before the dashed lines represent the three time steps before the counted time step, and the four points after the dashed lines represent the four time steps after the counted time step. In that case, the user's input stated that the number of time steps to be analyzed before the counted time step is three, and the number of time steps to be analyzed after the counted time step is four.

Hence, the S_p and S_n stress ranges are calculated using the combinations between all the times steps marked with circles and all the time steps marked with 'x'. The combination that returns the largest alternating stress value is the final result for the considered time step. Consequently, the number of time steps defined by the user has an important influence on the result.

This number cannot be too low, because if it is, the maximum alternating stress will not be found. It cannot be too high, because, not only will the time to run the evaluation procedure increase drastically, but also because it may be possible to reach another peak or another valley, which will produce an erroneous cycle counting result.

As explained above, this procedure was developed for use in combination with the Rainflow cycle counting. Thus, for comparing the results obtained by applying the presented method with those obtained by applying the Modified Wang

Brown, a similar procedure was developed for use in combination with the latter method.

In order to explain this method, the histories of stresses S_p shown in **Figures 6.3** to **6.5** are converted to a five dimensional Euclidian space using equation (4.13). This conversion is shown in **Figure 6.8**.

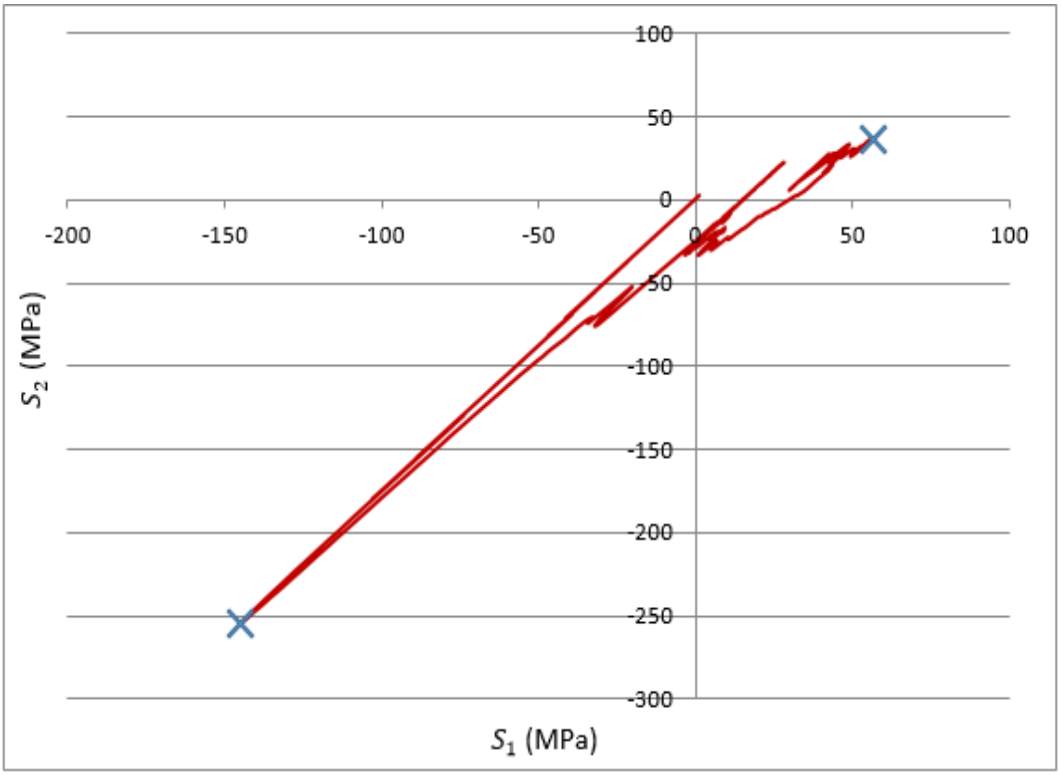

Figure 6.8: History of S_p stress presented in a $S_1 \, x \, S_2$ diagram.

Using the procedure developed for the Modified Wang Brown method (**Figure 4.22**) for the cycle counting of the history shown in **Figure 6.8**, the results of the first counting are several points that, when connected, generates a path, as explained in subchapter 4.8 (PMDR). The points farthest from each other - resulting from the first counting - are the ones marked in **Figure 6.8** with a blue 'x'.

To relate this path to the range of S_p, an enclosing surface solution is adopted. Enclosing surface solutions are methods used in non-proportional histories to relate paths of counted histories to ranges of stresses (for more information see [50]). Due to difficulties in implementing these approaches, only the Minimum Ball method is selected.

This method simply consists of evaluating the minimum-sized ball (on a 2D path) or sphere (on a higher dimensional path) that circumscribes the entire path. The diameter of this ball (or sphere) will be the range of S_p.

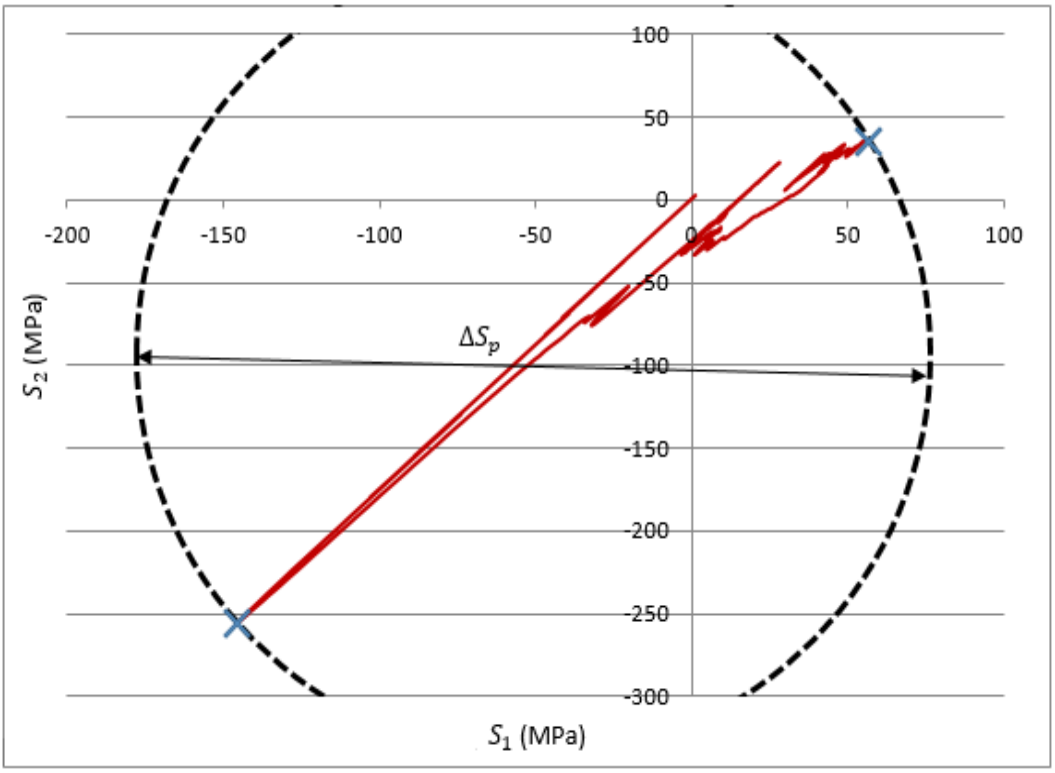

Figure 6.9: Example of the calculation of the S_p range using the minimum ball method.

The same procedure is used to calculate the S_n ranges. The computational routine implemented is summarized as:

1) Convert the entire histories of S_p and S_n to a five dimensional space.
2) Use the flowchart in Figure 4.22 to apply cycle counting on the history of S_p, where the result of this counting will not be the stresses, but the time steps;
3) With these time steps, calculate the ranges of S_n and S_p using the minimum ball method.

With this explanation, it is possible to calculate the alternating stresses, but it is not yet possible to be sure that these alternating stresses are the largest ones. In order to ensure that the maximum alternating stresses are found, a similar procedure of searching for the maximum alternating stress, as explained previously, is proposed in the next paragraph.

The time steps related to the S_p stresses that are touching the minimum ball are obtained. Going back to the example presented previously, the time steps (in the first counting) are the ones marked with a blue 'x' in **Figures 6.8** and **6.9**. If we call these time steps ${}^{m}t$ and ${}^{n}t$, it is possible to use a procedure similar to the

one in **Figure 6.7**, the difference being that now the combinations of time steps will pass through the minimum ball method to calculate the stress ranges.

The combination of ${}^{m-1}t$ (the time step immediately before the first one counted) with ${}^{n+1}t$ (the time step immediately after the second one counted) is obtained by transforming the stresses of these time steps into a five dimensional space, and then the minimum sphere circumscribing the stresses will represent the respective range.

This action is repeated for all possible combinations (inside the number of time steps given by the user) until the maximum alternating stress is found. The other difference between the search explained previously and this one is that the latter procedure gives the possibility of more than two points touching the minimum ball, and, consequently, the number of combinations will increase.

After having given this full explanation, it is now possible to show the results. The software with the Modified Wang Brown solution was implemented using the entire routine explained previously. The results of the cycle counting routines (Rainflow and Modified Wang Brown) returned that only the first counted cycle was significant, since it was the only one that gave any result for the CUF value; the other counted cycles result in insignificant or null CUF values.

The outputs generated from this counted cycle using both routines were identical: ΔS_p was equal to 607.53 MPa, ΔS_n was equal to 362.09 MPa, K_e was equal to 1.26, and, consequently the alternating stress (S_a) was equal to 433.82 MPa, resulting in a CUF value of 0.000176. Even with the results being equal, it is not possible to say that both routines will always generate similar results.

The fact that the loading history used in this example has characteristics of low non-proportionality between the values precludes such conclusion. In **Figure 6.9**, one can see how non-proportional the values are, by comparing them with a history with proportional values. In **Figure 6.9**, a history with proportional stress values would result in a straight line passing through the origin in the $S_1 \, x \, S_2$ diagram.

To illustrate the differences between these two methods, a highly non-proportional history is used.

6.3

Second Case Study

In this case study, histories of strain controlled fatigue tests [15] are used to compare the cycle counting methods and the damage models. The specimens used in [15] had solid circular sections with a diameter of 15.2 mm. The specimens were made of a 304L stainless steel material and were subjected to an axial-torsion strain controlled loading.

The strain history load is composed of combinations of different amplitude ratios of fully reversed axial-torsion cycles. The load amplitude ratios varied from cycle to cycle using one-degree increments, as shown in **Figure 6.10**. The first cycle starts at zero degrees with pure axial loading, and then it is followed by cycles where the torsion load is increased and the axial load is decreased. Therefore, the straight load lines plotted in **Figure 6.8** are rotated with the specified one degree increment until a circular boundary in the $\gamma/\sqrt{3}\ x\ \varepsilon$ diagram is formed. One block of this load is completed when it rotates 360 degrees.

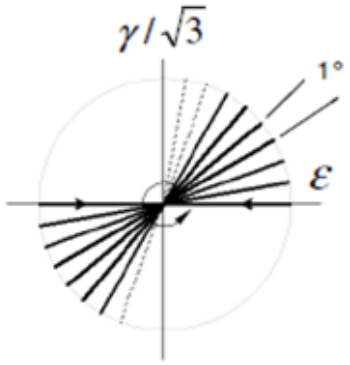

Figure 6.10: Strain axial-torsion load in the $\boldsymbol{\gamma/\sqrt{3}\ x\ \varepsilon}$ diagram.

It is interesting to note that each cycle is proportional. Therefore, each loading block is composed of 360 proportional load cycles. The cycle to cycle load-ratio variation turns the block into an example of a highly non-proportional load history.

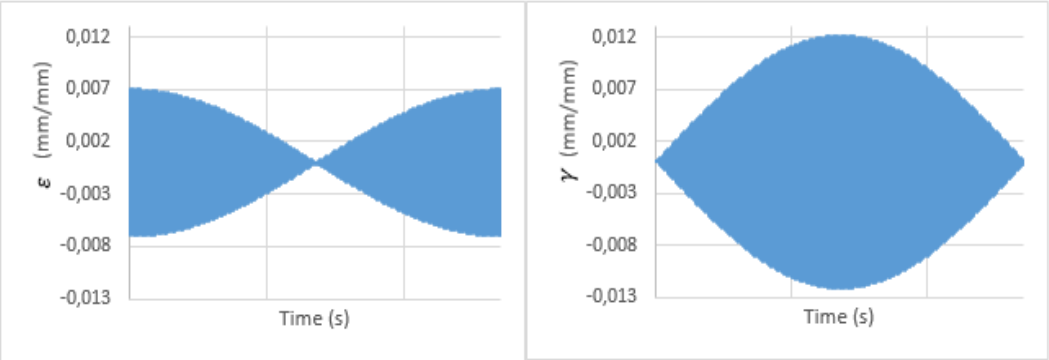

Figure 6.11: Strain load time history of one block.

The experiment performed in [15] consisted of repeating this block of strains until the specimen reached failure. The failure criteria considered a 5% drop in the axial load or torsion load when compared with their stabilized value. The tests used here were conducted with two specimens under a constant strain range value $\Delta\varepsilon$ of 0.014 mm/mm. In other words, the circumference diameter in **Figure 6.10** is 0.014 mm/mm. The first specimen failed after 5.5 blocks and the second after 5.8 blocks.

To compare these experimental values with those calculated using the methods in this thesis, the latter were separated into two different groups. One group adopted the critical plane approach. The other group was composed of the methods that do not adopt the critical plane approach. The methods belonging to this second group are called regular approach methods.

From the regular approach method group, only the Coffin-Manson (or Morrow) damage model was used. In this case, the strain ranges were obtained using the Extreme Value Method (EVM), the Modified Wang Brown (MWB) and the Rainflow method (see subchapter 4.3).

In the critical plane approach, the damage models to be compared were the Fatemie-Socie Model (FS), the Smith-Watson-Topper Model (SWT) and the Coffin-Mason (or Morrow) model (CM). Because the FS and the SWT models require determining the maximum stress perpendicular to the plane that is being evaluated, only the Bannantine and Socie (BS) and the Modified Wang Brown cycle counting methods were used.

As explained in subchapter 4.5, the Bannantine and Socie was developed as a change in the Rainflow method to find the maximum perpendicular stress (or strain, depending on the damage method) that occurs between the counted time steps. However, the MWB, as explained here-in, does not use that to count with,

and it is simple to search this parameter using the MWB method. After each counted cycle the value of maximum perpendicular stress is searched, belonging to the values of perpendicular stresses in the path returned by the counting.

However, because the test is strain controlled, the concepts explained in Chapter 5 have to be considered. The approach used to calculate the stresses is the Jiang and Sehitoglu method in conjunction with Tanaka's non-proportionality model (presented in subchapter 5.4.4). Due to the difficulty of implementing this model, the website eFatigue.com [51] was used as an auxiliary tool.

The strain load history is given as an input together with all the required material parameters, as explained in subchapter 5.4.4. After using the eFatigue auxiliary tool, the output is the complete stress-strain history (related using the previously cited method) and also a fatigue analysis. However, for the study of the fatigue methods implemented here, only the strains and stresses are collected and presented in **Figure 6.12** through **6.15**. Finally, the strains and stresses are used in the fatigue assessment in accordance with the methods explained above.

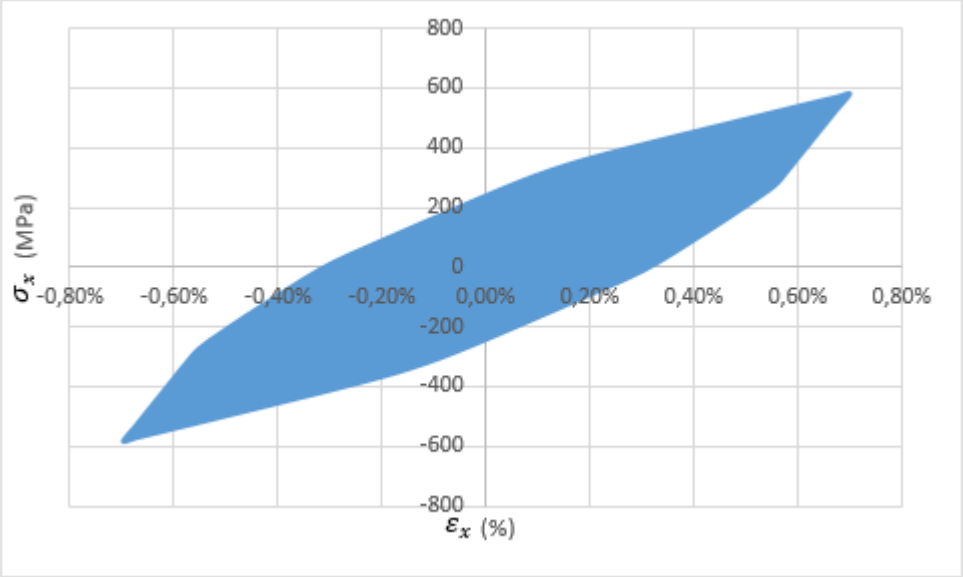

Figure 6.12: σ *x* ε diagram for the longitudinal direction.

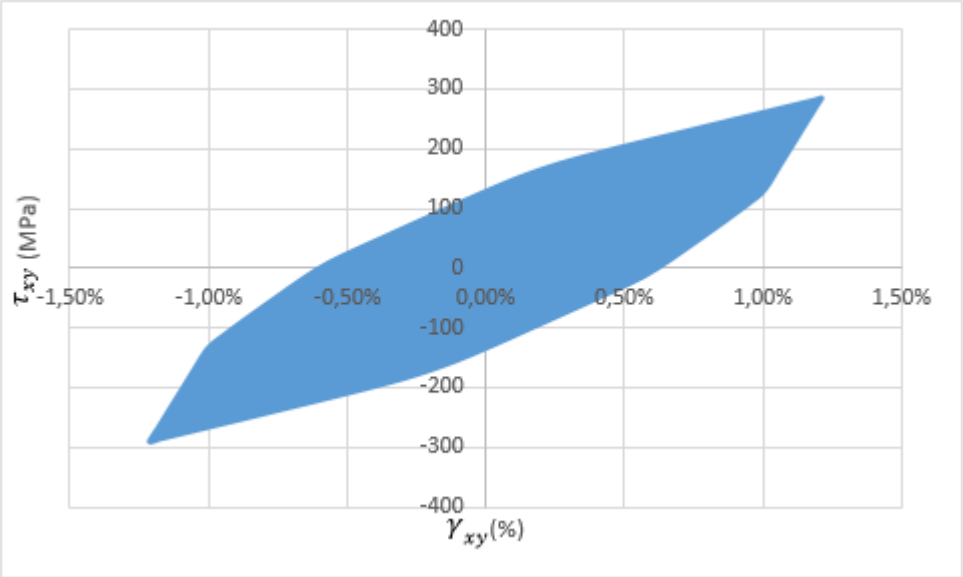

Figure 6.13: $\tau\ x\ \gamma$ diagram for the shear components.

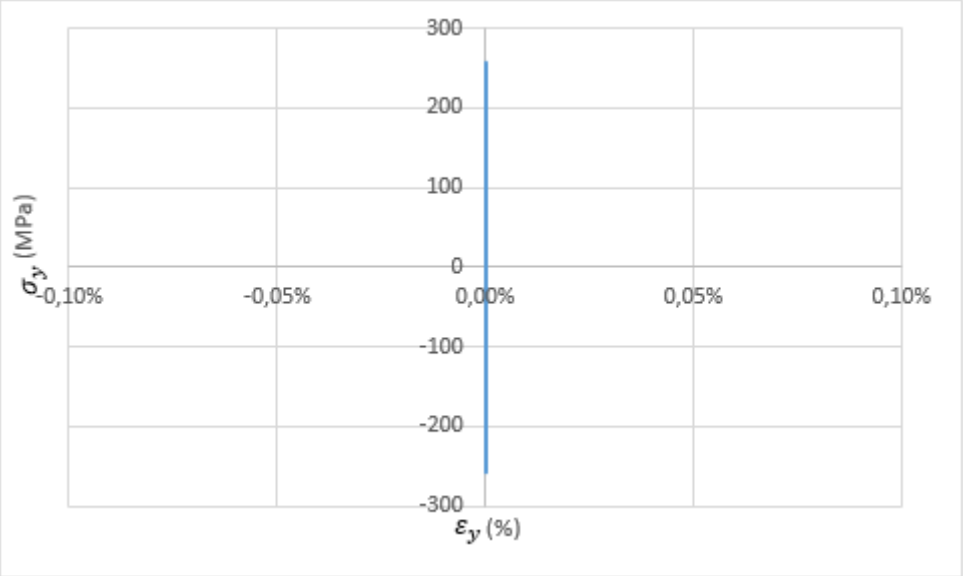

Figure 6.14: $\sigma\ x\ \varepsilon$ diagram for the circumferential direction.

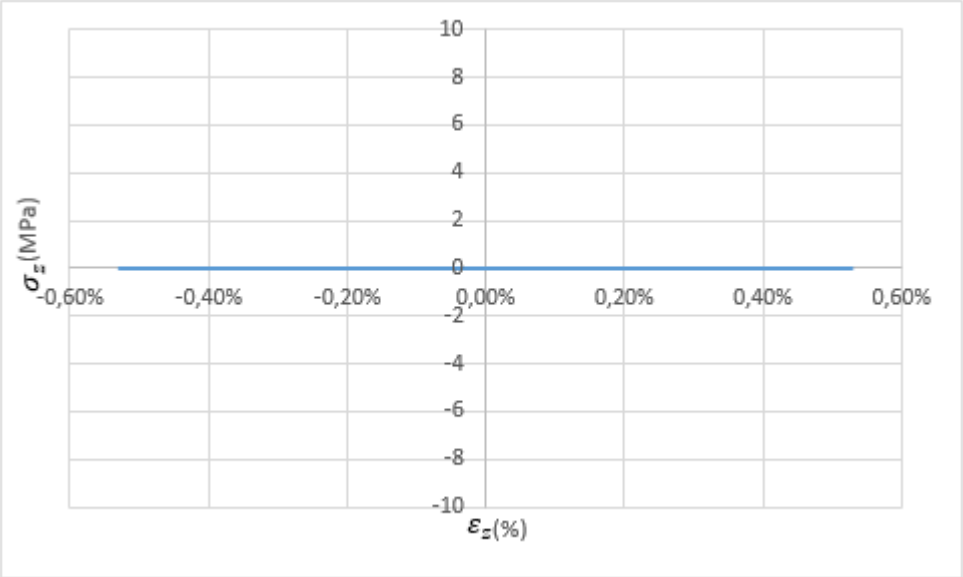

Figure 6.15: σ *x* ε diagram for the radial direction.

where the stress and strain in the ‘x’ direction is relative to the load acting in the axial directions, and the stress and strain in the ‘xy’ direction are caused by the torsion load. The stress in the ‘y’ direction (the circumferential direction of the cylinder) and the strain in the ‘z’ direction (the radial direction of the cylinder) are due to the Poisson effect.

The strain histories with time (**Figure 6.16**) are counted using the stress histories when necessary (**Figure 6.17**). In the regular approach, the histories are simply counted in the ‘x’, ‘xy’ and ‘z’ directions, the ranges are obtained and the damage is evaluated. In the critical plane approach, all the stresses and strains are calculated on a candidate critical plane, the cycle counting procedures are made on each plane, and the ranges of strains and the maximum perpendicular stresses are obtained to finally evaluate the damage.

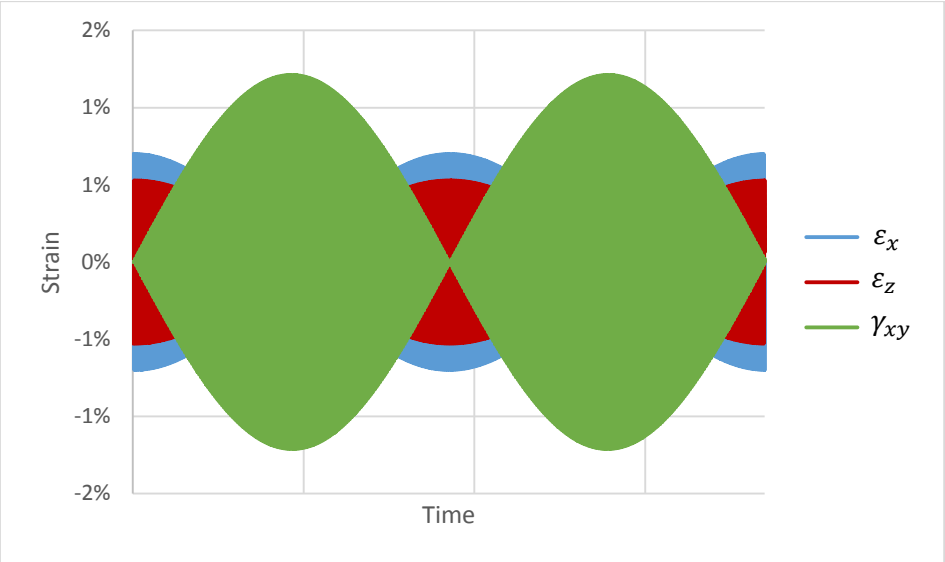

Figure 6.16: Time history of strains.

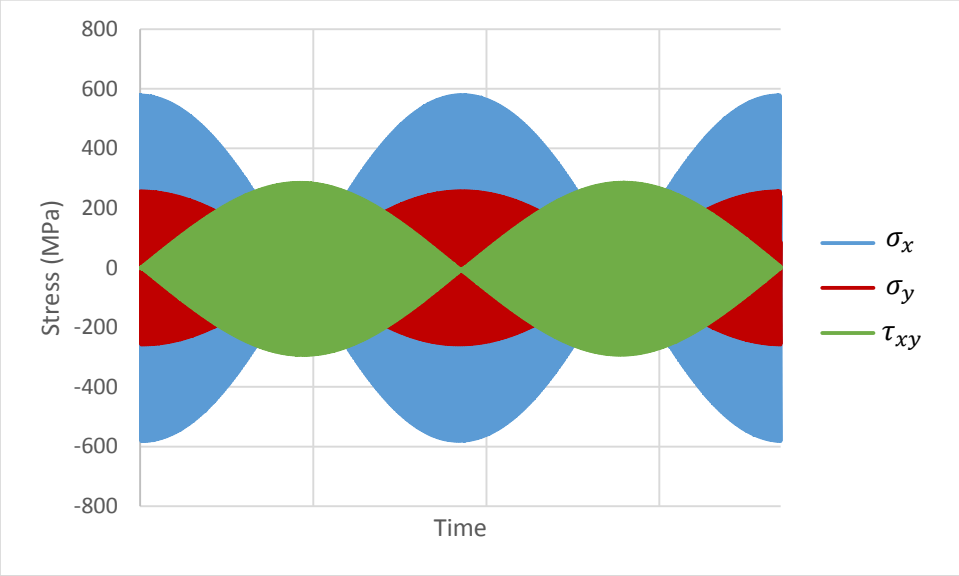

Figure 6.17: Time history of stresses.

The final result of each method can be compared based on the tables below, where the values represent the predicted number of blocks to failure for each combination of methods:

	Regular Approach				
	MWB	EVM	Rainflow (x)	Rainflow (z)	Rainflow (xy)
CM	1.31	0.49	42.05	17.15	8.67

Table 6.1: Final results using the regular approach methods.

	Critical Plane Approach	
	MWB	BS
FS	3.20	10.00
SWT	5.50	19.67
CM	4.77	7.05

Table 6.2: Final results using the critical plane approach methods.

The values in the tables represent the number of blocks allowed according to each method, which can be compared with the experimental results shown previously (5.5 and 5.8 blocks). With the stress values having been calculated, another result that is just as important to calculate is the result of a cycle counting performed on the stresses. The MWB method is used in such instances. For the damage models, the selected method is the one presented in the ASME Code.

It must be noted that, in the ASME Code, both S_n and S_p stresses have to be determined in order to do the fatigue analysis. However, because the stress distribution in the solid cylinder subjected to axial and torsion loads is smooth, equal values for S_n and S_p were assumed in the analysis.

Nevertheless, the design fatigue curve presented in the ASME Code includes a margin that would preclude a fair comparison with the other results. Thus, the ASME method was used once more, but this time, the CUF calculations were made using the alternating stress divided by the elastic modulus using the Coffin-Manson curve instead of the ASME Code curve. Table 6.3 presents the predicted number of blocks to failure for both methods:

	MWB
ASME Curve	0.13
CM Curve	3.94

Table 6.3: Final result of the MWB method using the stresses for counting.

7

Conclusions

This thesis has dealt with a number of topics that are relevant for the fatigue analysis of power plant components and piping subjected to mechanical and thermal loads.

The first topic dealt with the implementation and discussion of two analytical stress solutions applicable to thick walled pipes subjected to thermal and mechanical loads. As an example of this application, an actual measured pressure and temperature load history in a power plant was applied to a piping component and the transient analytical solutions were compared with results based on a commercial finite element software program.

The main goal of this study was to optimize the time consumed in determining the stresses that occur along the thickness of the pipe walls caused by transient thermal loading. The analytical solution implemented for this purpose consumed 1/3 of the time when compared with the solution time required for the finite element analysis. The implemented analytical solution allows the linearization of the stress components acting along the pipe wall thickness for all time steps used in the thermal transient solution. This is an important aspect for the accurate fatigue analysis of components under thermal loading transients.

Three other topics were addressed in the sequence: a study of the most frequently used fatigue damage models; the presentation and discussion of the most frequently used cycle counting methods applicable to components subjected to proportional and non-proportional load histories; and the presentation and discussion of stress-strain plasticity hardening models applicable to proportional and non-proportional load histories. Numerical algorithms of relevant models presented in the topics mentioned above were developed and implemented in C++ so that their combination could be applied to two case studies.

The last topic presented in the thesis was the application of the combinations of models to assess fatigue damage in two case studies.

The first case study entailed a thick pipe component subjected to transient thermal load and varying internal pressure. In this case, the most important aspect was the presentation of adjustments to the models so that a proper fatigue analysis for power plant components can be accurately performed.

One conclusion from the case was the confirmation that the Rainflow counting method could be adequately used because the principal stress directions do not change significantly as a function of time in this specific application, although there is non-proportionality in terms of the stress values generated by each loading type.

The second case study used loading, information and results acquired from multiaxial fatigue tests of 304L stainless steel specimens, and recently made available in the open literature. Applying the combination of model algorithms to the actual test data revealed that methods based on the regular approach did not produce good results, because the Extreme Value Method damage predictions were very conservative and the Rainflow predictions were non-conservative.

In the second case study, the critical plane approaches associated with the Modified Wang Brown method of cycle counting predicted damage very similar to the test results. The Smith-Watson-Topper damage model and Modified Wang Brown method of cycle counting damage results were the most accurate against the test damage results. Not coincidentally, this damage model, as explained in subchapter 3.7, is the best one for evaluating materials that fail in Mode I, such as 304L stainless steel.

As expected, **Table 6.3** shows very conservative results when the ASME Code procedure is used. The ASME Code fatigue analysis combines a conservative fatigue damage curve with the Extreme Value Method (EVM).

Conclusions of the second case study can be summarized as follows:

- The fatigue damage calculation procedure presented in the code for non-proportional histories is non-conservative [10].
- The best damage model to use depends on the material under evaluation.
- The MWB was the cycle counting method that showed the best results, especially when used with a critical plane approach.
- The damage model proposed in the code, using linearized stresses, combined with the MWB cycle counting method, might give good results, and this could be a good solution for a fatigue analysis of power plant components.

Three recommendations for future research topics are as follows:

- Search for more experimental results available in the literature for use in verifying the accuracy of the methods and models presented in this thesis, especially results from fatigue tests with temperature changes;
- Develop the analytical stress analysis considering two modification:
    - Add the modified Armstrong-Frederick using Tanaka's non-proportionality model to this analysis (to do so, [33] is recommended as a good reference for further reading). In this way, the strain history can be calculated and an elasto-plastic fatigue analysis can be performed. It is expected that this type of analysis will give more accurate results than the elastic analysis.
    - Expand the analytical solution to more components. The analytical solution was only validated for a thick walled pipe, which is a very simple geometry. A series of different components have to be evaluated in a power plant. Therefore, if analytical approaches could be generalized for other components, this would save even more time during a fatigue analysis.
- Improve the convex enclosure method. It was later observed that the method proposed here has its problems. These problems can be better observed in **Figure 7.1** and **7.2**. **Figure 7.1** contains an illustration of a micro crack under different loading conditions. Whereas at (a) the crack is subjected to normal stress that tends to open the crack, at (b) another normal stress is added that does not affect the crack; and at (c) a shear stress is added to (a) that affects the behavior of the crack.

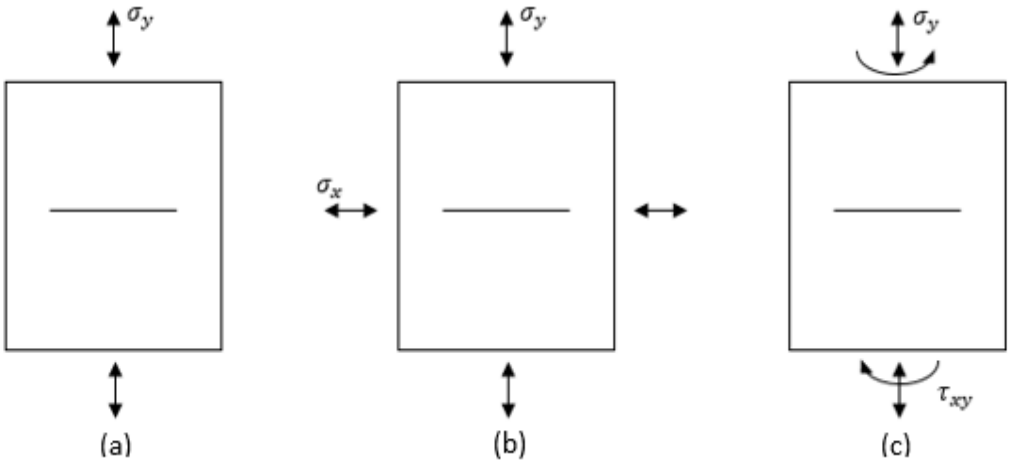

Figure 7.1: Illustration of a micro crack under different loading conditions.

Figure 7.2 shows examples of paths that the loading conditions in **Figure 7.1** can create if the stresses change through time. (I) and (II) are loading paths generated by loading condition (a), (III) is the path created by (b) and (IV) is the path of (c).

One can see that, when using the minimum ball method to calculate an equivalent stress for loading paths (II) and (IV), the equivalent stress will be equal. However, this should not be the correct result, since the loading condition at (c) is more damaging than at (a), such that a proper convex enclosure method has to be implemented to consider the difference. The minimum ellipse and MOI [50] are examples of good convex enclosure methods.

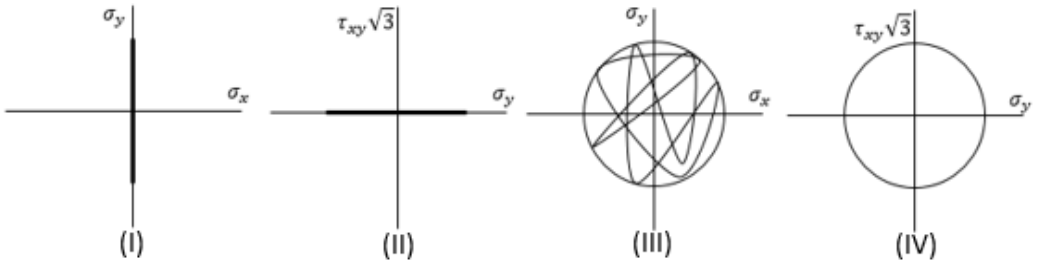

Figure 7.2: Illustration of the loading paths created by the loading conditions given in **Figure 7.1**.

On loading paths (I) and (III), the minimum ball method calculates the same equivalent stress, which is the correct result, since the addition of the other normal stress at (b) does not result in a more damaging loading condition. However, if the proposed convex enclosure methods (minimum ellipse or MOI) are applied to these loading paths, (III) will be more damaging than (I), and this is not the correct result. To remedy this problem, only the damaging stress components are to be considered when using the convex enclosure methods. For example, if a critical plane approach is being used, only the normal stress (or strain) on the plane and its shear stresses (or strains) should be considered.

Some concluding remarks can be added:

- The simplified elasto-plastic fatigue analysis based on elastic stress analysis and plasticity correction will remain the most common method for an engineering calculation method. Against this background, examined fields of improvement should be summed up. Particularly, the advantages of more complex cycle counting methods should be pointed out and the applicability of the Modified Wang-Brown Solution as a standard fatigue post processing method should be substantiated.

- Assessments of the non-proportionality of typical power plant load or stress-time histories should be made.
- A systematic examination of non-proportionality may be recommended as a possible topic for further studies.

Bibliography

[1] SINES, G.; WAISMAN, J. L.; DOLAN, T. J.: “Metal Fatigue.” McGraw-Hill, 1959.

[2] BANNANTINE, J.: “Fundamentals of Metal Fatigue Analysis.” Prentice Hall, 1990.

[3] SHIGLEY, J. E.: “Shigley’s Mechanical Engineering Design.”McGraw-Hill, 2011.

[4] CASTRO, J. T. P. D.; MEGGIOLARO, M. A.: “Fadiga – Técnicas e Práticas de Dimensionamento Estrutural sob Cargas Reais de Serviço. Volume I – Propagação de Trincas, Efeitos Térmicos e Estocásticos.” CreateSpace, p. 494, 2009.

[5] ALBRECHT, W.: “Instationäre Wärmespannungen in Hohlzylindern.“, Konstruktion 18, pp. 224-231, 1966.

[6] SINES, G.: “Behavior of Metals under Complex Static and Alternating Stresses.” Metal Fatigue, p.145-169, McGraw-Hill, 1959.

[7] FINDLEY, W. N.: “A Theory for the Effect of Mean Stress on Fatigue of Metals under Combined Torsion and Axial Load or Bending.” Journal of Engineering for Industry, p.301-306, 1959.

[8] MCDIARMID, D. L.: “A General Criterion for High Cycle Multiaxial Fatigue Failure.” Fatigue & Fracture of Engineering Material & Structures, v. 14, n. 4, p.429-453, 1991.

[9] DANG VAN, K.; PAPADOPOULOS, I. V.: “High-Cycle Metal Fatigue”, Springer 1999.

[10] SOCIE, D. F.; MARQUIS, G. B.: “Multiaxial Fatigue.” Warrendale, PA: Society of Automotive Engineers, p. 502, 1999.

[11] ASME Boiler and Pressure Vessel Code, Section III, The American Society of Mechanical Engineers, Edition 2010.

[12] ASME Boiler and Pressure Vessel Code, Section VIII, The American Society of Mechanical Engineers, Edition 2010.

[13] RETTENMEIER, P.; HERTER, K.-H.; SCHULER, X. and FESICH, T. M.: “Application of Advanced Fatigue Damage Parameters in Comparison With Fatigue Analysis Included in Codes and Standards.” ASME 2014 Pressure Vessels and Piping Conference. American Society of Mechanical Engineers, 2014.

[14] O'DONNEL, W. J.: "Code Design and Evaluation for Cyclic Loading – Sections III and VIII." Companion Guide to the ASME Boiler and Pressure Vessel Code, Third Edition, KR Rao Editor, 2009.

[15] SHAMSAEI, N.: "Multiaxial Fatigue and Deformation Including Non-Proportional Hardening and Variable Amplitude Loading Effects." Doctoral Dissertation, University of Illinois at Urbana-Champaign, 2010.

[16] MEGGIOLARO, M. A.; CASTRO, J. T. P.: "Statistical Evaluation of Strain-Life Fatigue Crack Initiation Predictions." International Journal of Fatigue, v. 26, n. 5, p. 463-476, 2004.

[17] BROWN, M. W.; MILLER, K. J.: "A Theory for Fatigue Failure under Multiaxial Stress-Strain Conditions." Proceedings of the Institution of Mechanical Engineers, v. 187, n. 1, p. 745-755, 1973.

[18] SOCIE, D. F.; SHIELD, T. W.: "Mean Stress Effects in Biaxial Fatigue of Inconel 718", ASME Journal of Engineering Materials and Technology, Vol. 106, pp. 227-283, 983.

[19] FATEMI, A.; SOCIE, D. F.: "A Critical Plane Approach to Multiaxial Fatigue Damage Including Out-of-Phase Loading." Fatigue and Fracture of Engineering Materials and Structures, Vol. 11, No. 3m pp. 149-166, 1988.

[20] SMITH, R. N.; WATSON, P.; TOPPER, T. H.: "A Stress-Strain Parameter for the Fatigue of Metal." Journal of Material, Vol. 5, No. 4, pp. 767-778, 1970.

[21] GUPTA, S. K.; FESICH, T. M.; SCHULER, X.; BHASIN, K. K. and ROOS, E.: "A Critical Plane Based Model for Fatigue Assessment Under Fixed and Rotating Principal Direction Loading." Transactions SMiRT 21, New Delhi, 2011.

[22] SIEBEL, E. and STIELER, M.: "Ungleichförmige Spannungsverteilung bei schwingender Beanspruchung." Zeitschrift des VDI, 97(5), pp. 121-126, 1955.

[23] ROUSSEV, A.: "Cycle Counting Methods for Load-Time-Histories Typical for Power Plant Application." Master's Thesis, Technical University of Sofia, 2012.

[24] MATSUISH, M.; ENDO, T.: "Fatigue of metals subjected to varying stress." Japan Soc. Mech. Engineering., 1968.

[25] BANNANTINE, J. A. and SOCIE, D. F.: "A Variable Amplitude Multiaxial Fatigue Life Prediction Model." Fatigue under Biaxial and Multiaxial Loading, European Structural Integrity Society, ESIS Publication 10, Mechanical Engineering Publications, London, pp. 35-51, 1991.

[26] BANNANTINE, J. A. and SOCIE, D. F.: “Multiaxial Fatigue Life Estimation Technique.” M, Mitchel and R. Landgraf (Eds), ASTM Symposium on Advances in Fatigue Lifetime Predictive Techniques, ASTM STP 1122, pp. 249-275, 1991.

[27] WANG, C. H.; BROWN, M. W.: “Life Prediction Techniques for Variable Amplitude Multiaxial Fatigue – Part I: Theories.” Journal of Engineering Materials and Technology 118.3, pp. 367-370, 1996.

[28] MEGGIOLARO, M. A.; DE CASTRO, J. T. P.: “An Improved Multiaxial Rainflow Algorithm for Non-Proportional Stress or Strain Histories – Part II: The Modified Wang-Brown Method.” International Journal of Fatigue, v. 42, pp. 194-206, 2012.

[29] COXERER, H. S. M.; GREITZER, S. L.: Geometry revisited. Washington (DC): Math. Assoc. Amer; 1967.

[30] DONG, P.; WEI, Z. and JEONG, K. H.: “A Path-Dependent Cycle Counting Method for Variable-Amplitude Multi-Axial Loading.” International Journal of Fatigue 32.4, pp. 720-734, 2010.

[31] DOWLING, N. E.: “Mechanical Behavior of Materials”, 3rd ed., Prentice Hall 2007.

[32] SLAVIK, D. and HUSEYIN, S.: “Constitutive Models Suitable for Thermal Loading.” Journal of Engineering Materials and Technology 108.4, pp. 303-312, 1986.

[33] MAHBADI, H. and ESLAMI, M. R.: “Cyclic Loading of Thick Vessels Based on the Prager and Armstrong-Frederick Kinematic Hardening Models.” International Journal of Pressure Vessels and Piping 83.6, pp. 409-419, 2006.

[34] KANAZAWA, K.; MILLER, K. J.; BROWN, M. W.: “Cyclic Deformation of 1% Cr-Mo-V Steel under out-of-phase loads.” Fatigue of Engineering Materials and Structures 2, pp. 217-228, 1979.

[35] SHAMSAEI, N.; FATEMI, A. and SOCIE, D. F.: “Multiaxial Cyclic Deformation and Non-Proportional Hardening Employing Discriminating Load Paths.” International Journal of Plasticity 26, pp. 1680-1701, 2010.

[36] DRUCKER, D. C.: “A More Fundamental Approach to Plastic Stress-Strain Relations.” Proceedings of the First U.S. Congress of Applied Mechanics, American Society of Mechanical Engineers, pp. 487-491, 1952.

[37] MRÓZ, Z.: “On the Description of Anisotropic Work Hardening.” Journal of the Mechanics and Physics of Solids 15.3, pp. 163-175, 1967.

[38] Karolczuk, A., Stress2Strain. Available in:

<http://www.mathworks.com/matlabcentral/fileexchange/24711-stress2strain>
Accessed in: 18/12/2014.

[39] KAROLCZUK, A.: “Non-local Area Approach to Fatigue Life Evaluation under Combined Reversed Bending and Torsion.” International Journal of Fatigue 30, pp. 1985-1996, 2008

[40] GARUD, Y. S.: “Prediction of Stress-Strain Response under General Multiaxial Loading.” Mechanical Testing for Deformation Model Development, ASTM STP 765, pp. 223-238, 1982.

[41] ARMSTRONG, P. J.; FREDERICK, C. O.: “A Mathematical Representation of the Multiaxial Bauschinger Effect.” Central Electricity Generating Board, Report RD/B/N 731, 1966.

[42] CHABOCHE, J. L.: “Cyclic Plasticity Modeling and Ratcheting Effects.” In: Proc. Of the 2nd International Conference on Constitutive Laws for Engineering Materials: Theory and Application, Tucson, AZ. Elsevier, New York, 1987.

[43] CHABOCHE, J. L.: “On Some Modifications of Kinematic Hardening to Improve the Description of Ratcheting Effects.” International Journal of Plasticity 7, pp 661-678, 1991.

[44] CHABOCHE, J. L., DANG VAN, K. CORDIER, G.: “Modelization of the Strain Memory Effect on the Cyclic Hardening of 316 Stainless Steel.” In: Proc. of the Transactions of the 5th International Conference on Structural Mechanics in Reactor Technology, Berlin, No. Div L in 11/3, 2008.

[45] JIANG, Y. and SEHITOGLU, H.: “Modeling of Cyclic Ratcheting Plasticity, Part I: Development of Constitutive Relations.” Journal of Applied Mechanics 63.3, pp. 720-725, 1996.

[46] JIANG, Y. and SEHITOGLU, H.: “Modeling of Cyclic Ratcheting Plasticity, Part II: Comparison of Model Simulations with Experiments.” Journal of Applied Mechanics 63.3, pp. 726-733, 1996.

[47] JIANG, Y. and KURATH, P.: “A Theoretical Evaluation of Plasticity Hardening Algorithms for Non-proportional Loadings.” Acta Mechanica 118. 1-4, pp. 213-234, 1996.

[48] TANAKA E.: “A nonproportionality parameter and a cyclic viscoplastic constitutive model taking into account amplitude dependences and memory effects of isotropic hardening.” European Journal of Mechanics, A. Solids 13.2, pp. 155-173, 1994.

[49] JIANG, Y. and KURATH, P.: “Characteristics of the Armstrong-Frederick Type Plasticity Models.” International Journal of Plasticity 12.3, pp. 387-415, 1996.

[50] MEGGIOLARO, M. A.; DE CASTRO, J. T. P.: “An Improved Multiaxial Rainflow Algorithm for Non-Proportional Stress or Strain Histories – Part I: Enclosing Surface Methods.” International Journal of Fatigue, v. 42, pp. 217-226, 2012.

[51] eFatigue, Multiaxial Strain-Life Analysis, Available in:

<https://www.efatigue.com/multiaxial/strainlife/#a>, Accessed in: 05/04/2015.